In vivo determination of a 2D strain field in a skeletal muscle using MR tagging

Kerckhoffs, R.C.P.

Award date:
1998

Eindhoven University of Technology Experimental and computational mechanics

In vivo determination of a 2D strain field in skeletal muscle using MR tagging

R.C.P. Kerckhoffs
WFW-report 98.023

Master's thesis

Eindhoven, June 1998

Experimental and computational mechanics (WFW)

Faculty of Mechanical Engineering

Eindhoven University of Technology

Professor: prof. dr. ir. T. Arts

Coach: dr. ir. P. Bovendeerd

Acknowledgements

I have not been alone in this project. The following people were of great assistance:
Peter Bovendeerd who supported me and provided a lot of tips and ideas during the project.
Theo Arts for his ideas on data processing and who thoroughly reviewed this report together with Peter.
Maarten Drost who performed the preparation of the animals and together with Rene van Donkelaar was a great help in defining an anatomical coordinate system.
Marijn Kruiskamp and Klaas Nicolay of the Bijvoet Centrum in Utrecht who helped me on MRI theory and the MRI experiments.
Liesbeth Ossevoort, my predecessor, for joining us in MRI experiments.
Carlijn Bouten and Cees Oomens, who let me join the meetings on muscle mechanics. They and other participants of these meetings gave useful comments.

The numerous suggestions, comments and criticisms of all these people improved the outcome of the project. To all of them goes a sincere expression of gratitude.

Abstract

To test numerical models of skeletal muscle mechanics, experimental data on regional muscle deformation are needed. Aim of our study is to investigate if it is possible to determine a 2d strain field in a reproducible slice in the tibialis anterior muscle of a Wistar rat.

A sequence called SPAtial Modulation of Magnetization (SPAMM) was used to apply line-shaped tags in the tibialis anterior muscle of a Wistar rat. When the muscle tissue deforms, due to physiological contraction, the lines deform accordingly. The deformed line-pattern is imaged with the FLASH (Fast Low Angle SHot) sequence. The data acquisition time of the FLASH sequence lies within 2 seconds.

The slice of observation should be related objectively to the animal's anatomy. To select such a slice, an anatomical coordinate system has been defined, using anatomical landmarks (e.g. the tibia-fibula fusion). After selection of an anatomically interesting slice, tags were applied and the muscle was stimulated. From the measured deformations, displacement fields were calculated. From this information strain fields were determined.

The determination of displacements is done by a phase analysis of a complex transformed image. A square hanning window was used for filtering. Every pixel within an image line receives a unique phase. The matching of these phases between the undeformed and deformed muscle yields the displacement of a pixel at subpixel accuracy.

Finally, Green Lagrange strains in a straingroup of 8 pixels are estimated in 2 ways. One according to a 1st order estimation and the other according to a 2nd order estimation. The magnitude of noise determines whether the first or second order strain estimation has to be applied. In general, the MR images made contain a lot of noise. Most of the noise is filtered out by the special filtering technique used in the phase analysis. The deformation field in the muscle turned out to be not very complex: large strain gradients existed only where different tissues slide along each other (e.g. at skin-muscle and muscle-muscle transitions). In our case (with a bandwidth frequency ratio of 1), the 1st order estimation satisfies.

Uncertainties in the estimated strains are in the order of 0.01 on a median strain value of 0.15 for the first principal strain ε_{11} and -0.07 for the second principal strain ε_{22}.
Because tissue inside a region of interest is assumed as a continuum, sliding between different tissues is characterized by large strains and shear ($\varepsilon_{11}>0.4$, $\varepsilon_{12}>0.5$). The 2nd principal strain – defined as the most negative strain – tends to align with the muscle fiber direction.

Table of contents

Vocabulary

anterior	Toward the front.
B_0	Static magnetic field in the scanner, generally ranging from 0.5 T to 1.5 T in the medical diagnostic environment. We used a magnetic field strength of 4.7 T. Spins are slightly more aligned parallel than anti-parallel with the applied field B_0 at T=300 K.
B_1	Rotating magnetic field (the RF pulse) at the Larmor frequency. The B_1 field flips the longitudinal magnetization into the transverse plane.
distal	Farther away from the trunk.
echo	The excited spins dephase very quickly. An echo is evoked by rephasing the spins with help of a 180° RF pulse or a reversed magnetic gradient.
echo time	TE. The time in a MRI sequence between the RF pulse and the maximum signal in the echo. At ½TE a 180° RF pulse is given (in a spin echo sequence) or a reversed gradient (in a gradient echo sequence), causing the echo.
excitation	Spins are flipped into the transverse plane by irradiating an RF pulse if the pulse frequency matches the Larmor frequency of the spins (the resonance effect).
fibular	Toward the fibula. See figure 2.1.
FID	Free Induction Decay. The signal emanating from the tissue right after excitation. Generally it fades away within 20 ms, due to T_2^* relaxation.
FLASH	Fast Low Angle SHot. A gradient echo sequence, using a small flip angle (7°-45°). Images can be acquired within 2 seconds. See also §2.2.2
flip angle	Angle between the magnetization vector and the static magnetic field. RF pulses are named after the flip angle they cause (e.g. a 90° RF pulse)
G	Magnetic gradient. On the static field B_0, a gradient can be superimposed. The result is that in a certain direction (x, y, z or arbitrary) the magnetic field is linearly increasing. The spins precess along the chosen direction with increasing frequency. The gradients in the x-, y- and z-directions are also denoted by G_{read}, G_{phase} and G_{slice} respectively.
gradient echo	see appendix A.
gyromagnetic ratio	γ. A constant related to a specific nucleus. (E.g. for ^1H: $\gamma = 2.6394 \cdot 10^8$ rad/Ts).
k-space	The raw MRI data, stored in a 2 or 3 dimensional matrix ($k_x \cdot k_y \cdot k_z$), which contains echoes stored parallel with each other. Fourier transformation of the k-space yields the MR image.

Larmor frequency	The frequency of the precessing spins. It depends on the gyromagnetic ratio γ and magnetic field strength, according to $\omega=\gamma B$.
longitudinal magnetization	Magnetization magnitude along the static magnetic field B_0.
medial	Toward the middle.
MRI	Magnetic Resonance Imaging. Technique that enables to image soft tissue non-invasively in vivo. It is based on the property that nuclei with an odd atomical mass, act like tiny magnets. By detecting this magnetization, after excitation, an image is made. Contrast depends on nuclei's density, relaxation times T_1 and T_2.
pixel	Picture element. Smallest 2d element in an image. In MRI, a pixel has a certain gray value, dependent on signal strength. A voxel of a slice is displayed in an image as a 2d pixel.
plane	is defined by 3 points, a line and a point, 2 crossing lines or 2 parallel different lines. A plane has no thickness.
posterior	Toward the back.
precession	Here, the cone-shaped rotation of a spin vector about the axis of the static magnetic field.
proximal	Toward the point of attachment of the limbs at the trunk.
repetition time	The time between two RF pulses, in which 1 echo per slice is read out in a spin echo sequence or gradient echo sequence.
RF pulse	Radio Frequency pulse. Varying magnetic field B_1 with radio frequency. It flips the longitudinal magnetization into the transverse plane, creating transverse magnetization.
sagittal plane	Any plane which is parallel to the median plane. The median plane divides a body through the middle in a left and right part.
slice	A plane with a thickness. A slice is generally imaged in MRI. The thickness is needed for adequate signal acquisition per slice voxel.
SPAMM	SPAtial Modulation of Magnetization. A sequence to apply tags or lines in soft tissue. See §2.2.1.
spin	Angular momentum of nuclei, theorized by Pauli. All nuclei with an odd atomical mass, possess a characteristic spin quantum number I.
spin echo	See appendix A.
TE	See echo time.
TR	See repetition time.
T_1	Spin-lattice relaxation time. After excitation, the nuclei return to their

	equilibrium, losing their energy by emitting electromagnetic radiation and by transferring energy to the lattice (the surroundings). This time is quantified by the T_1 time constant. It is the time for the longitudinal magnetization to return to 63% of its original value in an exponential function. T_1 varies in biological tissue from approx. 50 ms to a few seconds. T_1 depends on magnetic field strength.
T_2	Spin-spin relaxation time. Energy is transferred between nuclei in different energy states. Immediately after excitation, spins precess in phase. However, interactions between spins create random local magnetic field variations which cause fluctuations in the frequency of the spins. This causes a dephasing of the spins and a decay in the magnitude of the transverse magnetization. $T_2<T_1$. T_2 is independent on magnetic field strength. T_2 ranges in biological tissue from a few ms in solids to a few seconds in fluids.
T_2^*	Relaxation time due to magnetic field inhomogeneities. $T_2^*<T_2$.
tag	A local different magnetic situation in tissue. It is attached to the tissue and deforms if the tissue deforms.
tibia	Shinbone. See figure 2.1.
transverse magnetization	Magnetization magnitude perpendicular to the magnetic field B_0. This magnetization rotates with the Larmor frequency of the spins and is detected by an RF receiving coil.
voxel	Volume element. Smallest element in MRI from which a signal with certain strength is read. It has length, height and depth.

1. Introduction

To study damage and adaptation mechanisms in skeletal muscle due to mechanical load, mathematical models have been developed (Gielen, 1998). To test these models experimentally, information on the deformation inside skeletal muscle is required.
This can be accomplished using Magnetic Resonance tagging techniques, which have been applied extensively lately to measure deformation in heart muscle. MR imaging is based on the principle of nuclear magnetic resonance. The most commonly used nucleus is that of hydrogen because of its abundance in biological tissue and its high sensitivity to magnetic resonance.

In a study performed recently by Ossevoort (1997), a tagging technique called SPAMM (SPAtial Modulation of Magnetization (Axel et al., 1989) and the FLASH (Fast Low Angle SHot) imaging technique have been demonstrated to be most promising for utilization in skeletal muscle.

To obtain reproducible results a slice was selected. A coordinate system was defined in the muscle using anatomical landmarks. Next, MR line shaped tags were introduced by spatial modulation of magnetic saturation of the tissue. The lines were attached to the tissue. When the tissue deformed, the line pattern deformed accordingly. By comparing the tag positions in images of a deformed and undeformed muscle a displacement field was determined. From this information the strain distribution field was calculated.

Aim of this study was to investigate whether the strain field induced by an isometric tetanic contraction in skeletal muscle could be determined in a reproducible longitudinal cross-section. The thus determined strain field will be used for testing a numerical model describing muscle mechanics. The tibialis anterior muscle in the hind leg of the rat has been chosen to investigate for the following reasons:
On the one hand the muscle's geometry and boundary conditions can be modeled relatively easily, while on the other hand, its behaviour is too complex to be resolved with simple planimetric models. The muscle is partly fixed to the bone and it contains an internal and an external tendon sheet. These characteristics can cause an interesting complex displacement field.

Chapter 2, material & methods, describes the techniques being used in the experiments and in data processing. Paragraph 2.1 describes the implementation of the anatomical coordinate system, from which a slice of observation is selected. The coordinate system is defined by anatomical landmarks.
In paragraph 2.2 the applied MR techniques are discussed. The most important ones are the SPAMM technique for applying tags in the tissue and the FLASH technique for acquiring the image, containing the undeformed and deformed tag pattern.
Paragraph 2.3 presents an overview of the performed experiments. It describes the fixation of the rat, the stimulation of the m. tibialis anterior and the data acquisition.
The processing of the acquired images with undeformed and deformed line patterns in the muscle is described in paragraph 2.4. The displacement field is calculated per pixel. The first positive harmonic in the frequency domain is bandpassed and transformed back to the spatial domain. Thus, an image is created with complex amplitude. The phases of the pixels in the deformed and undeformed muscle are determined. By comparison of the phases, the displacements are determined. After determination of the displacement field, Green Lagrange strains were estimated, using both a 1^{st} and 2^{nd} order estimation of the deformation gradient tensor. The principal strains are used for visualization.
An error analysis will be presented in paragraph 2.5, where 2 kinds of strain fields are estimated: 1) between 2 undeformed muscles in the same rat and hind-leg and 2) in a known displacement field of an artificial muscle.

Chapter 3 presents the results of the tagging, the determination of the displacements and the strains.

In chapter 4 the used methods and results will be discussed.

Finally, conclusions and recommendations are presented in chapter 5 and 6 respectively.

2. Material and methods

2.1 Selection of slice of observation

In selecting the location of a slice of observation, 3d reconstructions of the tibia bone, the fibula bone and the tibialis anterior muscle were made using a high resolution MRI dataset of the lower hind leg of a rat (Kretzers, 1996), containing 15 transverse spin echo images (slice thickness 0.5 mm, slice distance 1.5 mm). For a more detailed description of the MR imaging techniques see appendix A. In the reconstruction an anatomical coordinate system (the coordinate system is explained in §2.1.4) was displayed together with the cross-section of the slice of observation with the tibialis anterior muscle. Thus the slice of observation and its orientation can be previewed. The 3d reconstructions together with the anatomical coordinate system are also useful for testing reproducibility of the anatomical coordinate system in different rats.

The *magnet* coordinate system (X, Y, Z) is connected to the MRI scanner. The origin is located in the middle of the magnet, the Z-axis is aligned with the core, the Y-axis is the vertical and the X-axis is positioned orthogonally to the Z- and Y-axis, according to a right-hand coordinate system. Generally, the positive Z-axis points to the animal's head. In this magnet coordinate system, the anatomical coordinate system is defined.

First, anatomical characteristics of the m. tibialis anterior will be discussed. Then, a method will be shown to reconstruct the 3d geometry of the tibia, fibula and m. tibialis anterior. Finally, a description of the anatomical coordinate system will be given, from which the slice of observation is selected.

2.1.1 Anatomy of the rat's hind-leg

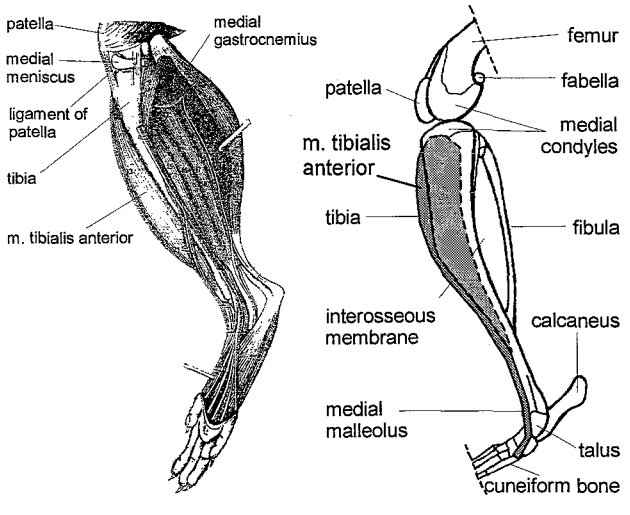

Figure 2.1: Left: medial view of the hind-leg's muscles, right: medial view of the bones (Popesco et al, 1992)

The discussion of the anatomy as follows is based on human anatomy, but is also valid for the rat's anatomy (Drost, 1998). As can be seen in figure 2.1, the tibialis anterior muscle is a superficial muscle: it is a

dorsiflexor of the ankle and invertor of the foot. Proximally, it originates from several regions: from the tibia's lateral condyle, from half to two-thirds of the lateral surface of the tibia shaft and from the anterior side of the interosseous membrane between the tibia and fibula bone. Distally, the muscle ends in a tendon, which starts as an internal tendon sheet at approximately 1/3 from the lower part of the leg, runs to the medial side of the leg and inserts in the medial and inferior regions of the medial cuneiform and the adjoining base of the first metatarsal bone. The deep peroneal nerve stimulates the muscle (Williams, 1995).

2.1.2 Tibia and fibula 3d reconstruction

For a representation of the anatomical coordinate system and the slice of observation, a 3d reconstruction is made using a MRI dataset. This paragraph describes the 3d reconstruction of the bones in the hind-leg.

Because we only need information on the bones, first the transverse images of the dataset are manually cleared from anatomical features in the soft tissue, especially tendons and tendon sheets that appear black in the image, just like bone. Next, the images are made binary by applying a threshold half way between the average gray values of the pixels in the soft tissue and those in the bones. After thresholding, the tibia and the fibula appear black, the rest of the image is white. The magnet X-, Y- and Z-coordinates of the tibia contour pixels – pixels at the tibia edge – in image *i* are stored into columns $\tilde{t}_{xi}$, $\tilde{t}_{yi}$ and $\tilde{t}_{zi}$ respectively. The coordinates in the tibia columns are sampled such that the columns become of equal length and are respectively stored in the tibia contour matrices $\underline{T}_x$, $\underline{T}_y$, $\underline{T}_z$,. For example the structure of the tibia contour matrix of the X coordinates is as follows:

$$\underline{T}_x = \left[\tilde{t}_{x1} \quad \tilde{t}_{x2} \cdots \quad \tilde{t}_{xi} \cdots \quad \tilde{t}_{xn}\right]$$

The X-, Y- and Z-coordinates of the fibula contour pixels undergo a similar operation.

From these matrices a 3d mesh image is constructed by connecting all neighbour points by line elements. Further, by applying ray-tracing algorithms the bones are represented as solid objects.

2.1.3 M. tibialis anterior 3d reconstruction

The muscle's reconstruction is performed differently, because muscles are difficult to differentiate.

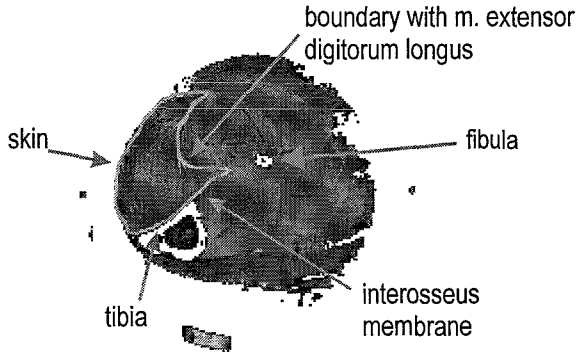

Figure 2.2: The contour of the m. tibialis anterior in a transverse cross-section

A threshold procedure is not appropriate to extract the muscle contour from an image. Therefore points on the muscle contour are indicated manually. Through these points higher order polynomials are fitted (Bogaerds, 1997).
The accuracy of the sampling depends on the sampling location on the contour (see figure 2.2). Along the skin and the tibia the contour can be distinguished clearly, because of the high contrast. However, along the interosseous membrane between the tibia and fibula and along the extensor digitorum longus muscle the sampling accuracy is lower due to low contrast between muscles which results in a wider inter-observer variability.
From the polynomial representation, coordinate columns $\tilde{m}_{xi}$, $\tilde{m}_{yi}$ and $\tilde{m}_{zi}$ of equal length are calculated.
Like the tibia and fibula 3D reconstruction, the columns are put into matrices $\underline{M}_x$, $\underline{M}_y$ and $\underline{M}_z$. The matrices are used for the construction of the 3D-mesh of the muscle surface.

2.1.4 The anatomical coordinate system

To acquire a reproducible slice of observation, an anatomical coordinate system (x, y, z) is implemented, based on anatomical landmarks of the hind-leg.

First, a high-resolution multislice spin echo dataset of the leg is produced, consisting of contiguous transverse slices. See table 2.1 for the dataset parameters.

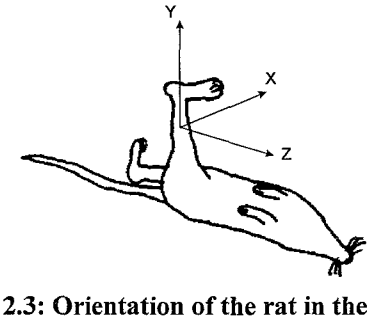

Figure 2.3: Orientation of the rat in the magnet

The rat's leg lies approximately parallel with the magnet Y-axis (figure 2.3) in our setup with the foot pointing to the positive direction. All transverse images are perpendicular to the Y-axis.

In the anatomical coordinate system (see figure 2.4), the origin $\vec{p}_0$ and the z-direction $\vec{e}_z$ are defined as:

$$\vec{p}_0 = \tfrac{1}{2}(\vec{p}_1 + \vec{p}_2) \tag{2.1}$$

$$\vec{e}_z = \frac{\vec{p}_2 - \vec{p}_1}{\|\vec{p}_2 - \vec{p}_1\|} \tag{2.2}$$

where $\vec{p}_1$ and $\vec{p}_2$ are the positions of the center of gravity of the tibia at two specific levels along the tibia

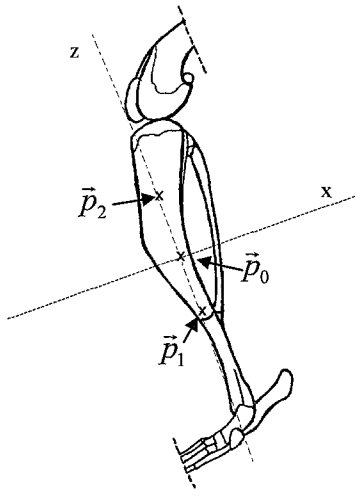

Figure 2.4: The anatomical coordinate system, displaying the origin x- and z-axis, the origin $\vec{p}_0$ and two point defining the z-axis ($\vec{p}_1$, $\vec{p}_2$), which are explained in the text.

TR	= 11 s
TE	= 16 ms
Slice thickness	= 0.4 mm
Field of view	= 30 × 30 mm
Number of pixels	= 256 × 256 pixels

Table 2.1: Parameters of the high-resolution MRI dataset

bone, which will be defined later.
The x-direction $\vec{e}_x$ and y-direction $\vec{e}_y$ are defined as:

$$\vec{e}_x = \frac{\vec{t} - \vec{f}}{\|\vec{t} - \vec{f}\|} \tag{2.3}$$

$$\vec{e}_y = \vec{e}_z \times \vec{e}_x \tag{2.4}$$

where $\vec{t}$ and $\vec{f}$ are the centers of gravity of respectively the tibia and fibula in the anatomical xy-plane.

Bones serve as landmarks for the definition of the anatomical coordinate system, because bones are rigid structures. Nevertheless, the coordinate system is also partly based on the tibialis anterior muscle, for the simple fact that a slice through this muscle is the main goal of the coordinate system.

The implementation of the anatomical coordinate system will be discussed step by step below:

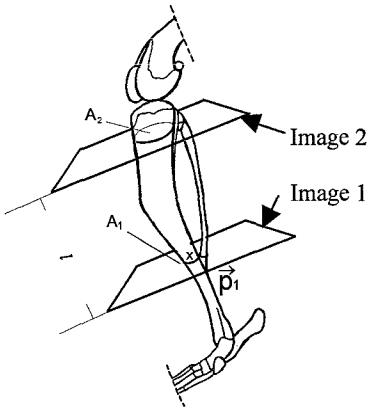

Figure 2.5: Image 1 and 2, the tibia-fibula fusion and the factor 2.8 tibia area increase respectively.

Determination of the anatomical z-axis

- *Image 1*: See figure 2.5. From the MRI dataset, the most proximal image is selected where the tibia and the distal end of the fibula meet. In this image, the center of gravity $\vec{p}_1$ and the area A_1 of the tibia cross-section are determined.

- *Image 2*: See figure 2.5. Next, in proximal direction, the image is searched where for the tibia area A_2 it holds that $A_2 = 2.8 \cdot A_1$. The distance between the images containing A_1 and A_2 is length

$$l = \mathrm{Y(image\ 2)} - \mathrm{Y(image\ 1)} \tag{2.5}$$

At the proximal side of the tibia, the transverse tibia area increases quickly, seen from distal to proximal position. The presence of a large gradient is a good criterium for accurate slice selection along the main tibia axis. In that region however, the position of the center of gravity of the cross-section varies also strongly, because of the asymmetry of the tibia. In this section a second point for the definition of the z-axis cannot be found with sufficient accuracy. Therefore a 3rd image is chosen, which is situated distal to

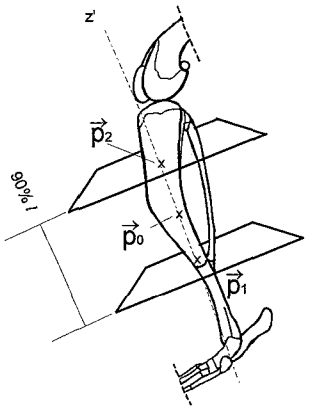

Figure 2.6: Image 3

the region of the large gradient. Here, the position of the center of gravity varies minimally.

- *Image 3*: The tibia center of gravity $\vec{p}_2$ in the image at

$$Y(\text{image } 3) = Y(\text{image } 1) + 0.9 \cdot l \tag{2.6}$$

is determined next (see figure 2.6). In this region, the tibia cross-section changes less quickly along the bone, enabling a relatively accurate determination of the in-plane position of the tibia center of gravity. The anatomical origin is now defined according to equation (2.1), the z-axis according to equation (2.2).

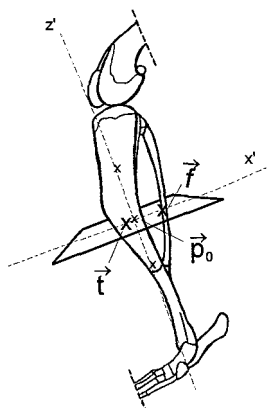

Figure 2.7: Image 4

The anatomical x- and y-axes

- *Image 4*: The slice through $\vec{p}_0$ (eq. 2.1, figure 2.7) perpendicular to the z-axis is imaged. See also appendix B. This image of the anatomical xy-plane is generally not part of the transverse dataset, because the z-axis is tilted with respect to the magnet coordinate system. In this image, centers of gravity of both the tibia $\vec{t}$ and the fibula $\vec{f}$ are determined. The vector between $\vec{t}$ and $\vec{f}$ defines the direction of the anatomical x-axis, according to eq.(2.3). The y-axis is found perpendicular to the x- and z-axis, corresponding to a right-handed coordinate system (see eq. 2.4).

2.1.5 The slice of observation

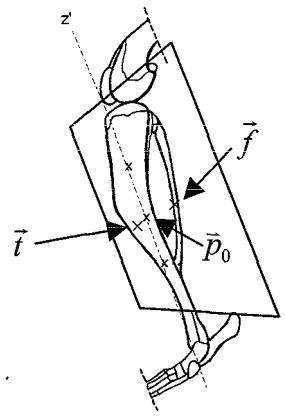

Figure 2.8: The selection of the slice of observation

The slice of observation (figure 2.8) is determined by two points ($\vec{p}_4$ and $\vec{p}_5$) and is situated parallel with the z-axis:

$$\vec{p}_4 = \vec{t} + \alpha(\vec{f} - \vec{t}) \tag{2.7}$$

$$\vec{p}_5 = \vec{t} + \beta(\vec{m} - \vec{t}) \tag{2.8}$$

Where α and β are respectively the fibula and muscle coefficients and $\vec{m}$ is the center of gravity of the m. tibialis anterior in the anatomical xy-plane. To select a well defined slice through the m. tibialis anterior (e.g. a slice through the middle of the muscle), α and β are both set equal to 0.6.
The thus selected slice of observation is the slice in which tags will be applied for measuring deformation.

2.2 The use of Magnetic Resonance techniques

2.2.1 Application of tags by spatial modulation of magnetization

The SPAMM (SPAtial Modulation of Magnetization) sequence - developed by Axel and Doughtery (1989) is used for applying saturated tag lines in tissue. In SPAMM this means that tissue water is saturated by sinusoidal varying magnetization.
See figure 2.9a, which depicts the starting situation. The coordinate system (x', y', z') in figure 2.9 is a frame that rotates about the z'-axis at the Larmor frequency, resulting from the static magnetic field B_0. First, a non-selective 90° RF-pulse produces transverse magnetization (figure 2.9b). To this transverse magnetization a dephasing gradient along the x-axis G is introduced (figure 2.9c). This magnetic gradient G causes nuclei to precess at different frequencies, dependent on their position. After a time interval t [s], the phase φ [rad] along the gradient G in the y-direction is determined by:

$$\varphi(y) = y\gamma \int_0^t G(\tau)d\tau \qquad (2.9)$$

where γ is the gyromagnetic ratio.
Next, a non-selective 180° RF-pulse refocuses the spins that were dephased by B_0 field inhomogeneities (figure 2.9d). The 180° RF-pulse causes the spin vectors to rotate 180° about the x'-axis.

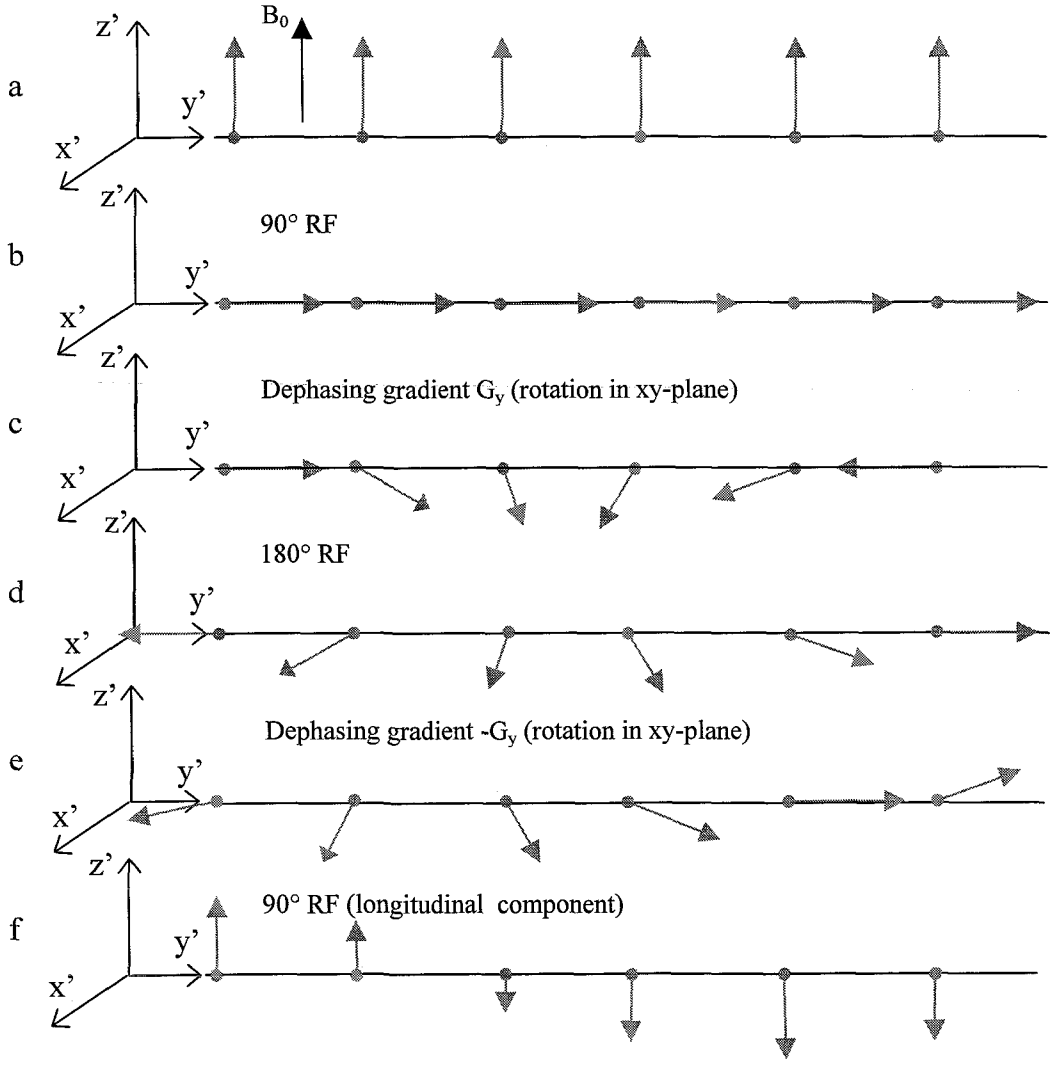

Figure 2.9: The influence of SPAMM on tissue water magnetization (the gray vectors). The situations from a through f are explained in the text.

After the 180° pulse, the sign of the dephasing gradient is changed in order to let the dephasing progress (figure 2.9e).

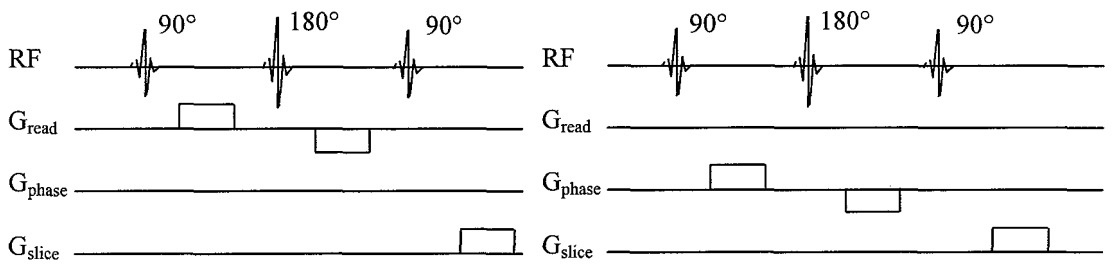

Figure 2.10: The SPAMM sequence schematically depicted. Left: application of tag lines perpendicular to the read-out direction. Right: application of tag lines perpendicular to the phase-encode direction

Finally, a second non-selective 90° RF pulse is applied (figure 2.9f) in order to turn the modulated transverse magnetization along the longitudinal axis. This results in spatially modulated longitudinal magnetization with a sinusoidal intensity profile. Figure 2.10 shows the sequence schematically.
The phase modulation between two peaks in the intensity profile is $\varphi = 2\pi$ rad. The length of a period l [m] of the tagging lines can thus be calculated from:

$$l = \frac{2\pi}{\gamma \int_0^t G(\tau) d\tau} \tag{2.10}$$

The composite flip angle of the RF pulses is called the tagging angle. It determines the depth of the

RF pulse:	B1-insensitive adiabatic segmented BIR4 pulse (Hendrich et al, 1994)
G strength:	2.164 mT/m.
Effective G time:	11 ms (2 times 5.5 ms)
Peak to peak distance:	1 mm.
Tagging angle:	0° (90°+180°+90°)
Time between tagging and image acquisition:	100 ms

Table 2.2: SPAMM parameters

modulation along the z'-axis.
See table 2.2 for the used parameters of the SPAMM sequence.

2.2.2 *Imaging by FLASH*

It is important to acquire an image in a short time for the following two reasons:
- to avoid muscle fatigue during stimulation,
- to avoid the disappearance of tagging lines due to T_1 relaxation.

Very fast imaging sequences exist, for example gradient echo sequences (see also appendix A). For this experiment, the FLASH (Fast Low Angle SHot, see figure 2.11) sequence is used. A repetition time of 10 ms can be reached without much loss of signal to noise ratio (S/N).
In the FLASH sequence, the maximal S/N occurs for a well-defined optimum flip angle, the so-called

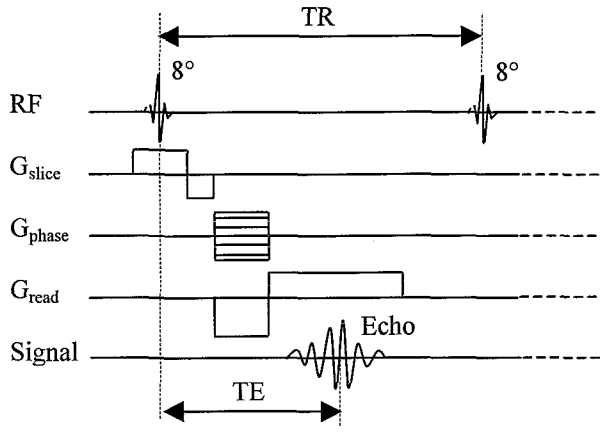

Figure 2.11: The FLASH sequence schematically depicted. See also appendix A.

Ernst flip-angle:

$$\alpha_e = \arccos\left(e^{\frac{-TR}{T_1}}\right) \tag{2.11}$$

TR	= 15.6 ms
TE	= 7 ms
Flip angle α_e	= 8°
Slice thickness	= 1 mm
Field of view	= 60 × 30 mm
Number of pixels	= 256 × 128
Total imaging time	= 2.00 s
Peak to peak distance	= 4.27 pixels

Table 2.3: FLASH parameters

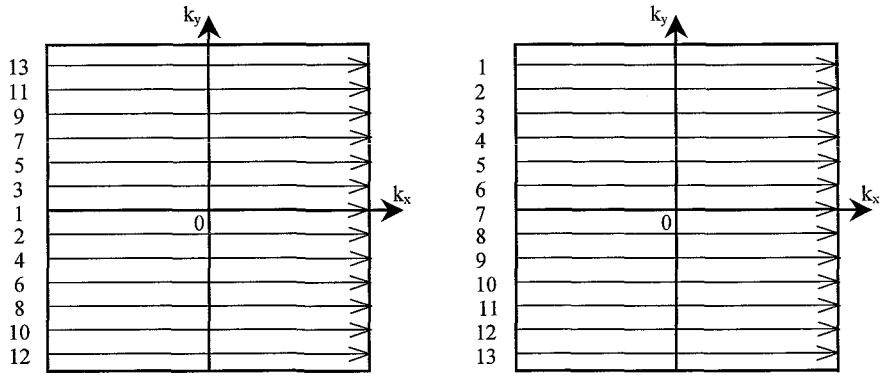

Figure 2.12: Acquiring the k-space in centric order (left) and in monotonic order (right). The numbers indicate the order of read-out acquisition. See also appendix A

The T_1 relaxation time of the tibialis anterior muscle is $T_1 = 1.5$ s. Table 2.3 presents the used FLASH parameters.

The k-space (see appendix A) is sampled in a centric order in the phase-encoding direction (G_{phase} in figure 2.11) instead of a monotonic order.

Monotonic sampling (figure 2.12) means that sampling of the k-space starts with the most positive phase-encoding gradient. In discrete steps the phase-encoding gradient follows a path linearly to the most negative phase-encoding gradient.

Centric sampling (figure 2.12) means that the sampling of the k-space starts with a zero phase-encoding gradient and increases alternatingly to the maximal positive and minimal negative phase-encoding. The center of the k-space contains most information of an image. In centric sampling, the center is sampled in the beginning of the sequence, so before the longitudinal magnetization starts to decrease due to the effects of T_1 relaxation.

2.3 Experimental setup

An 8 weeks old male Wistar rat (m = 248 g) was anaesthetized with a mixture of hypnorm, dormicum and atropine. Next, the rat was intubated and ventilated. From this moment on, halotane gas was administered by inhalation. A platinum stimulation electrode was sutured to the peroneus communis nerve. The stimulation was tested visually.

The foot was plastered with paladur, a dentist's cement, in order to suppress its internal degrees of freedom and to be able to attach the foot to the footstool of the fixation device. A pair of arnite tweezers was attached to the femur in order to suppress the femur's degrees of freedom at a knee angle of 90°. In this manner, conditions for an isometric contraction are satisfied.
The rat was placed in the MR compatible fixation device, consisting of a cylindrical pipe, in which the other end of the pair of tweezers was clamped. An RF coil was placed around the lower left hind-leg. Finally, the plastered foot is glued to the footstool. The foot was fixated in plantar flexion (110°) to cause a pre-tension in the tibialis anterior muscle. Thus, the initial position of the muscle was well defined and fixed.

The rat was kept warm with a heated water mattress. The CO_2 content of the expired gas was monitored with a capnograph during the experiment. The rectal temperature was also monitored.

Once the rat was positioned in the fixation device, the device was placed in the center of the magnet (B_0 = 4.7 T). The resonance frequency of the MR coil was tuned. The impedance of the coil was matched to the impedance of the transmission line in order to avoid signal loss and distortion due to reflection. To create an

Stimulation frequency	= 100 Hz
Stimulation amplitude	= 3 V
Pulse length	= 0.5 ms
Maximal stimulation time	= 2 s

Table 2.4: Stimulation parameters

optimal setting of the homogeneity of the magnetic field a dynamic shimming procedure was followed.
The rat was stimulated according to a load application protocol, designed in an experiment by Ossevoort (1997). The parameters presented in table 2.4 normally yield a supra-maximal tetanic contraction.

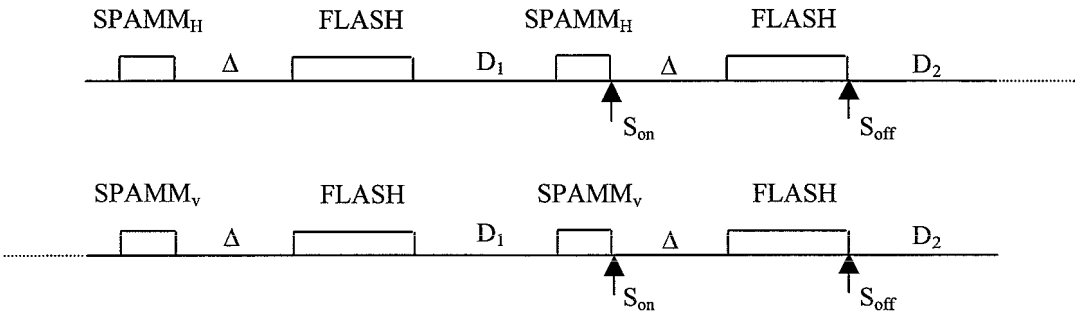

Figure 2.13: Timing of the experiment

The timing of the experiment has been schematically depicted in figure 2.13.

1. During the period SPAMM$_H$, a tagging grid of horizontal lines was applied to the tissue. After a delay time Δ=100 ms, image acquisition of the undeformed muscle started using the FLASH sequence. After image acquisition of the undeformed muscle, a delay time D_1=10 s was necessary in order to let the magnetization return to its equilibrium state.
2. Then a similar tagging grid of horizontal lines was applied to the tissue during the second SPAMM$_H$ period. The muscle was stimulated after 10 ms. The second FLASH sequence started after a delay time Δ=100 ms in order to let the muscle reach full contraction. After image acquisition the stimulus was turned off. A delay time D_2=60 s was needed, not only to allow the magnetization to return to the equilibrium state, but also to permit muscle recovery.

The protocol steps 1 and 2 were repeated for the steps 3 and 4 with the modification that the 2 periods SPAMM$_V$ were used for application of vertical lines. Thus, four images were acquired during one experiment:

- an image containing the unstimulated muscle with a horizontal tagging grid;
- an image containing the stimulated muscle with the deformed horizontal tagging grid;
- an image containing the unstimulated muscle with a vertical tagging grid;
- an image containing the stimulated muscle with the deformed vertical grid.

The following experiments have been performed:

- Acquisition of deformation data in a selected slice according to the anatomical coordinate system with the fibula and muscle coefficients at $\alpha = \beta = 0.6$. Two measurements have been made in this slice.
- Acquisition of deformation data in a slice parallel to the first slice (α=β=0.6), one millimeter towards the fibula. Here, also two measurements have been made in this slice.
- Acquisition of deformation data in a slice parallel to the first slice, 2 millimeter towards the fibula. Here, 6 measurements have been made: 5 containing tags and 1 without tags. This image contains also the m. extensor digitorum longus.
- Acquisition of deformation data in a slice perpendicular to the selected slice, in a transverse cross-section of the muscle (this is the same slice as the xy-plane in the anatomic coordinate system).
- Furthermore, there exist 2 high-resolution images of the unstimulated muscle (made in the procedure of the anatomic coordinate system): one of the xy-plane and one of the first selected slice (α=β=0.6).

2.4 Data processing

From the acquired images, displacement fields were determined by comparison of the undeformed tag lines with the deformed tag lines. From the displacement field, a strain field was computed.

2.4.1 Displacement field

The description of the displacement of material points is the main goal. Material points ξ in the undeformed state $x_0=\chi(\xi,t_0)$ and in the deformed state $x_1=\chi(\xi,t)$ were matched. The muscle slice was discretized in volume elements or voxels, the smallest detectable material points, appearing as pixels in a 2d image.

The images are measurements of signal intensities I_0 and I_1 in the undeformed and deformed state respectively. From these measurements phases φ_0 and φ_1 were determined. The phases are attached to material points. This means that pixels in the undeformed and deformed state with equal phase are the same material points. For a 1d situation it holds that

$$\varphi_0(x_0) = \varphi_1(x_1) \tag{2.12}$$

The coordinates of the phases are denoted by the material coordinates x_0 and x_1. Equation 2.12 gives a relationship between x_0 and x_1:

$$x_1 = f(x_0) \tag{2.13}$$

Finally, from x_0 and x_1, the displacement u is calculated:

$$u = x_1 - x_0 \tag{2.14}$$

For a 2d situation, phases were determined separately in the vertical and horizontal direction.

2.4.1.1 Example of resolving the displacements in a 1D linear deformation field

A sinusoidal tagging grid is applied to a 1d bar with length L_0. A material point ξ is identified by its position

$$x_0 = \chi(\xi,t_0) \tag{2.15}$$

The material points receive intensity

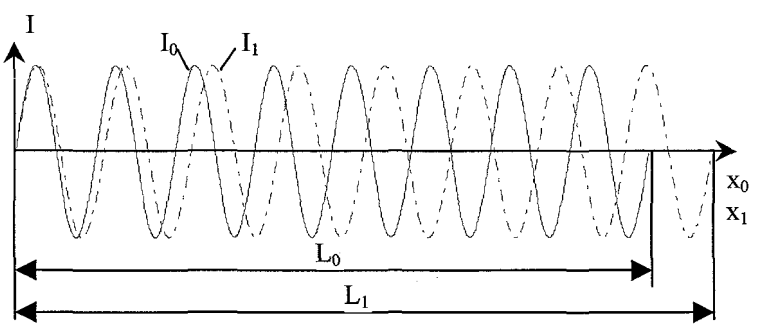

Figure 2.14: Intensity along the bar in undeformed state I_0 and deformed state I_1

$$I_0(x_0) = A\cos(k_0 x_0 + \psi_0) \tag{2.16}$$

(see figure 2.14) with A the amplitude, ψ_0 the phase-offset and k_0 the wave-number

$$k_0 = \frac{2\pi}{l_0} = \frac{2\pi n}{L_0} \tag{2.17}$$

where l_0 is the length of a period, n the number of periods applied to the bar and L_0 the length of the bar. Next, the bar is stretched elastically with a stretch ratio λ, such that $L_1=\lambda L_0$. Thus the number of periods applied to the bar remain equal, but the period-length stretches to $l_1=\lambda l_0$. The new intensity profile is now:

$$I_1(x_1) = A\cos(k_1 x_1 + \psi_0) \tag{2.18}$$

with

$$k_1 = \frac{2\pi}{l_1} = \frac{2\pi n}{L_1} = \frac{2\pi n}{\lambda L_0} \tag{2.19}$$

Writing equation 2.16 in complex form yields:

$$I_0 = \frac{A}{2} e^{i(k_0 x_0 + \psi_0)} + \frac{A}{2} e^{-i(k_0 x_0 + \psi_0)} \tag{2.20}$$

Now, if the negative frequencies (the right-hand term on the right-hand side of equation 2.20) are filtered out in the frequency domain, the result is

$$I_0 = \frac{A}{2} e^{i(k_0 x_0 + \psi_0)} \tag{2.21}$$

A similar operation is carried out for the deformed situation I_1. The phases φ_0 and φ_1 are extracted by taking the argument of I_0 and I_1 respectively. Next, the phases are expressed as a function of x_0 and x_1 by

$$\varphi_0 = k_0 x_0 + \psi_0 = \frac{2\pi n}{L_0} x_0 + \psi_0 \tag{2.22}$$

$$\varphi_1 = k_1 x_1 + \psi_0 = \frac{2\pi n}{\lambda L_0} x_1 + \psi_0 \tag{2.23}$$

The matching of the phases is done by setting eq.(2.22) equal to eq.(2.23):

$$x_1 = \frac{2\pi n}{L_0} \cdot \frac{\lambda L_0}{2\pi n} x_0 = \lambda x_0 \tag{2.24}$$

which is the relationship between the undeformed state x_0 and deformed state x_1 with a stretch ratio λ. Finally, the displacement u(x) is determined by equation 2.14.

In the example the displacement field was linear but that condition is not strict. As long as physical laws are satisfied, φ_1 can be any function of x_1: $\varphi_1=f(x_1)$. For a measured complex displacement field, as in our experiments, the equation

$$k_0 x_0 + \psi_0 = f(x_1) \tag{2.25}$$

has to be resolved numerically.

2.4.1.2 Resolving displacements in a 2d deformation field

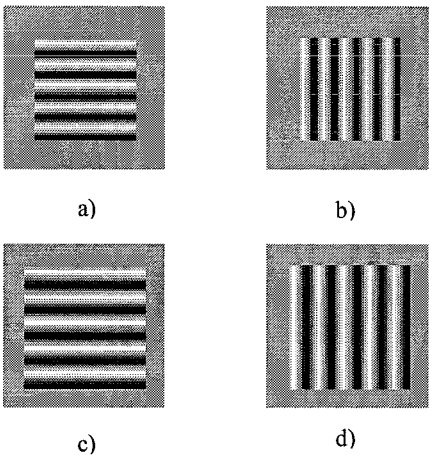

Figure 2.15: Undeformed 2D grid (top) and deformed grid (bottom)

To extract phase-information from an image, first the image containing the undeformed field with a sinusoidal intensity (see figure 2.16a) will be transformed by a 2D Fast Fourier Transform (FFT) into the frequency domain. Because a complex deformation field will yield a frequency spectrum, only the first positive harmonic was band-passed by applying a 2d square hanning window (figure 2.16b). 2 bandwidths were used: a bandwidth frequency ratio (BFR=$\frac{bandwidth}{frequency} = \frac{b}{f_1}$) of 1 and a BFR of 1.2.

The value of the first harmonic f_1 is calculated by:

$$f_1 = \frac{L}{l} = \frac{\gamma L \int_0^t G(\tau)d\tau}{2\pi} \tag{2.26}$$

In case of horizontal tag lines, L is the height of the image. When vertical tag lines exist in the image, L is the image width. The first harmonic is equal to the number of tag lines the image contains. In this experiment, $f_1 = 30$.

Secondly, the frequency domain will be transformed back to the spatial domain after filtering and thus an image with complex amplitude is acquired (figure 2.16c and 2.16d). Because of the complex nature of the filtered image, each tag line contains pixels with equal phase. Perpendicular to a tag line, a linear increase of phases exists after unwrapping the phases.

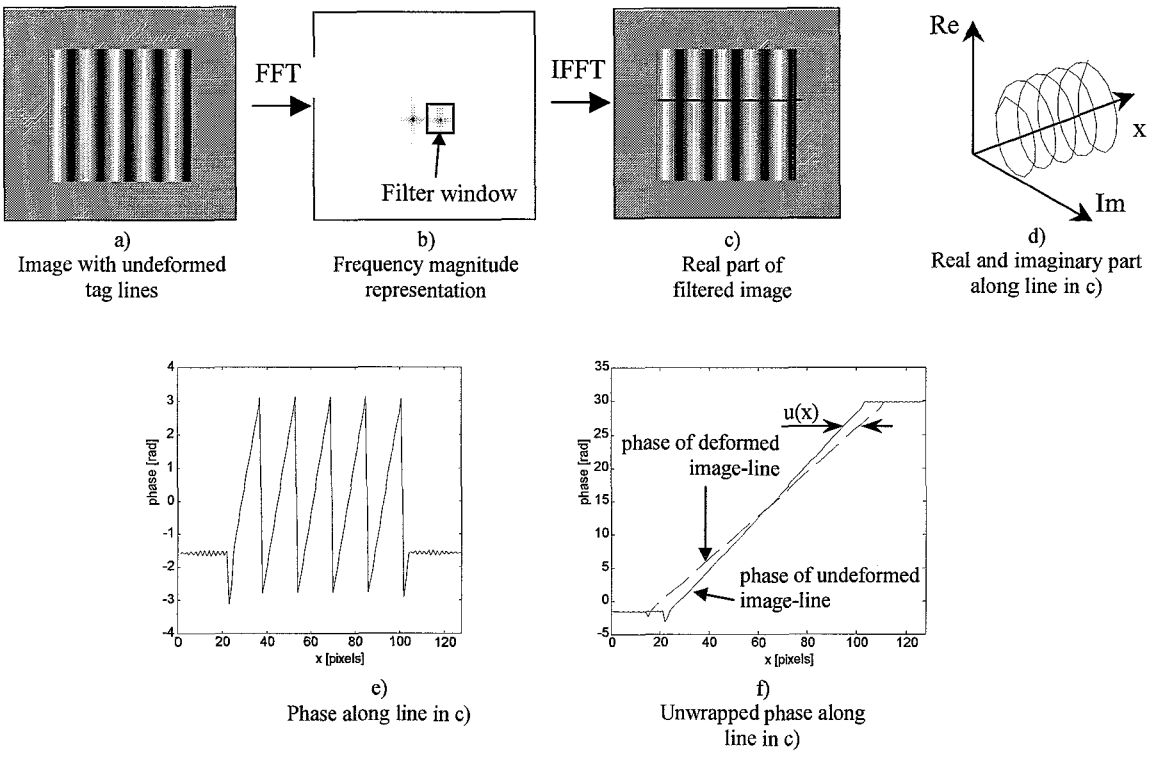

Figure 2.16: The procedure for extracting phase information from an image. See text for explanation.

Unwrapping phases means changing absolute jumps greater than π to their 2π complement, as can be seen in figure 2.16e) and f). The same procedure is applied to the image containing the deformed tag lines (see figure 2.16f).

Finally, pixels in the deformed filtered image with a certain phase have to be matched with pixels in the undeformed filtered image with equal phase.
When deformation has occurred, pixels in the different images with equal phase have different position vectors and one element of the displacement vector $\vec{u}$ is determined. This procedure is separately carried out for the images containing the horizontal and vertical tag lines. When combining the horizontal and vertical displacements, the complete 2d displacement vector for a material point is acquired – assuming there is no displacement perpendicular to the imaged slice.

It is important to match phases from the deformed to the undeformed state and not in the reverse order. There are 2 reasons for doing this:

- Because of the discrete nature of the images a certain discrete phase in the undeformed state will never exactly match a phase in the deformed state. So an interpolation between 2 phases has to be carried out (enabling subpixel accuracy). The intensity along a line perpendicular to the tagging lines in the undeformed muscle is of a sinusoidal form. The relation between the position and the unwrapped phase is therefore linear, as can be seen in fig 2.16f). A linear interpolation in the linear relationship between position and phase results in the exact position of the phase to be matched in the undeformed muscle.
- Determination of horizontal and vertical displacements $\vec{u}_h$ and $\vec{u}_v$ are carried out separately. As can be seen in figure 2.17, matching phases from the undeformed to the deformed state, results in an error $\vec{u}_e$ in the displacement $\vec{u}$ when shear is present in the deformation field. However, when matching a phase from the deformed in the undeformed state, the exact displacement is found. This is possible because undeformed horizontal and vertical tag lines are orthogonal and have a constant phase.

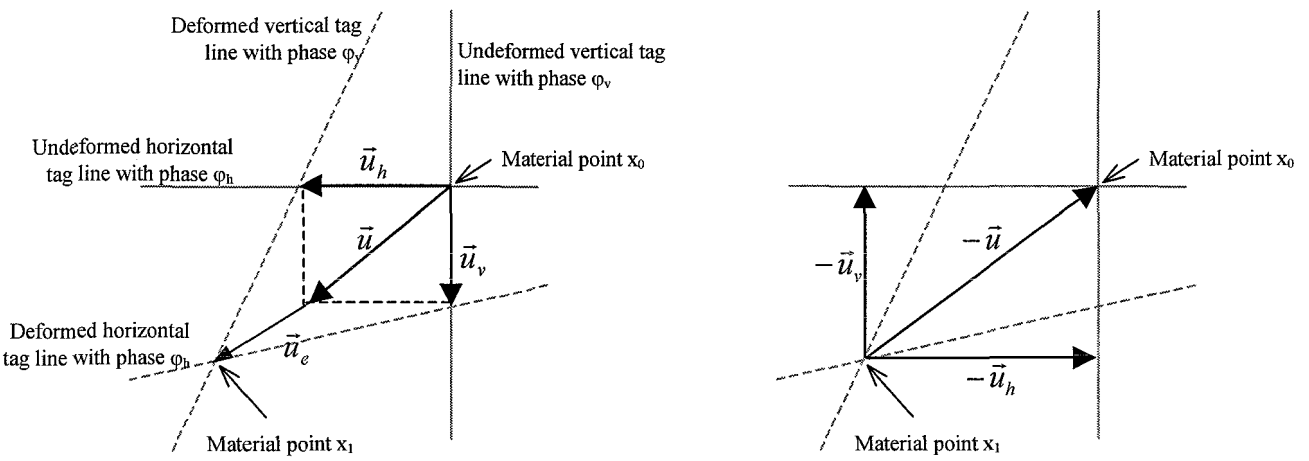

Figure 2.17: Matching phases from undeformed to a deformed state (left) and matching phases from deformed to undeformed state (right)

2.4.2 Strain field

From the determined displacement field, a strain field was calculated. Therefore, in every data point the deformation gradient tensor **F** had to be calculated. Theoretically, the deformation gradient tensor **F** relates to the undeformed state x_0 and deformed state x_1 through:

$$d\vec{x}_1 = \mathbf{F} \cdot d\vec{x}_0 \tag{2.27}$$

$$\mathbf{F} = \left(\vec{\nabla}_0 \vec{x}_1\right)^c \tag{2.28}$$

where $d\vec{x}_0$ and $d\vec{x}_1$ are infinitesimal difference vectors between two points P and Q (figure 2.18) in respectively the undeformed and deformed state.

From the experiment, position vectors were obtained for material points, also called markers, located at finite distances from each other.

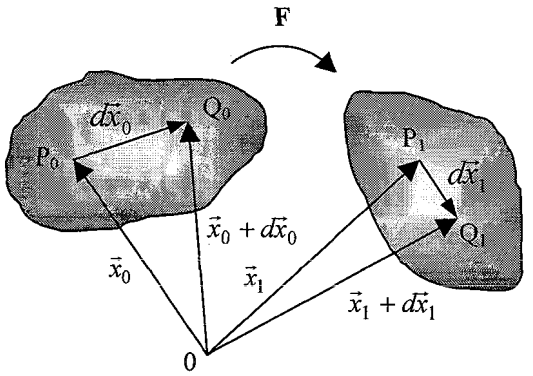

Figure 2.18: Undeformed and deformed infinitesimal difference vector $d\vec{x}_0$ and $d\vec{x}_1$ respectively.

The distribution of markers around a central marker is called a straingroup (figure 2.19). According to Peters (1987) **F** can be linearly estimated from a straingroup by

$$\hat{\mathbf{F}}_1 = \mathbf{X}_{01}^c \cdot \mathbf{X}_{00}^{-1} \tag{2.29}$$

with $\mathbf{X}_{00}$ and $\mathbf{X}_{01}$ the distribution tensors of the difference vectors $\Delta\vec{x}_{0i}$ and $\Delta\vec{x}_{1i}$:

$$\mathbf{X}_{00} = \frac{1}{k}\sum_{i=1}^{k} \Delta\vec{x}_{0i}\Delta\vec{x}_{0i} - \Delta\underline{\vec{x}}_0\Delta\underline{\vec{x}}_0 \tag{2.30}$$

$$\mathbf{X}_{01} = \frac{1}{k}\sum_{i=1}^{k} \Delta\vec{x}_{0i}\Delta\vec{x}_{1i} - \Delta\underline{\vec{x}}_0\Delta\underline{\vec{x}}_1 \tag{2.31}$$

with $\Delta\underline{\vec{x}}_0$ and $\Delta\underline{\vec{x}}_1$ being the mean difference vectors.

However, it can be shown that in complex deformation fields - especially at the borders - $\hat{\mathbf{F}}_1$ isn't very accurate. Geers (1996) developed a method for a 2nd order estimation $\hat{\mathbf{F}}_2$ of **F** by

$$\hat{\mathbf{F}}_2 = \mathbf{N}^c \cdot \mathbf{M}^{-c} \tag{2.32}$$

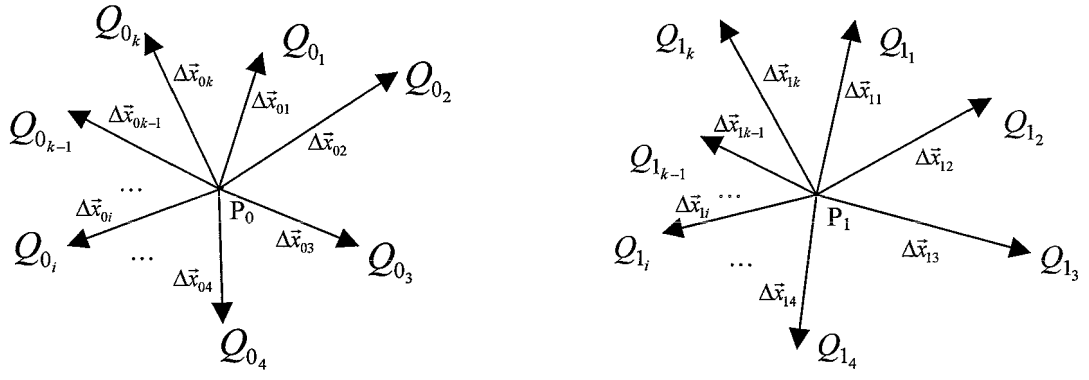

a) Undeformed straingroup b) Deformed straingroup

Figure 2.19: Undeformed and deformed strain group. P is the central marker, the Q's are the markers in the straingroup.

For the meaning of the tensors **N** and **M** and their laborious elaboration is referred to Geers (1996).

At least 3 markers are necessary in a straingroup for the solution of eq.(2.29) and 6 markers for the solution of eq.(2.32). The use of more markers implies a statistical correction, but also an averaging over a larger area. In our experiments, 8 markers (pixels) were used in a straingroup, because of the symmetrical distribution. Another reason is the abundance of markers, so averaging remains in a small area.

Whether $\hat{\mathbf{F}}_1$ or $\hat{\mathbf{F}}_2$ is used, depends on the quantity of noise in the deformation field. Roughly said, in a deformation field, which contains a lot of noise, $\hat{\mathbf{F}}_1$ is preferred. Otherwise, when the data contains less noise, it is better to use $\hat{\mathbf{F}}_2$. The exact influence of noise on the estimation - and as a consequence whether the 1st order or 2nd order estimation will be chosen - has to be determined by experiments.

The deformation gradient tensor is the basic tensor for strain computations. The Green-Lagrange strain tensor is defined as

$$\mathbf{E} = \tfrac{1}{2}(\mathbf{F}^c\mathbf{F} - \mathbf{I}) \tag{2.33}$$

$$\hat{\mathbf{E}}_i = \tfrac{1}{2}(\hat{\mathbf{F}}_i^c\hat{\mathbf{F}}_i - \mathbf{I}) \qquad i \in \{1,2\} \tag{2.34}$$

The (biased) estimated strain tensors $\hat{\mathbf{E}}_1$ and $\hat{\mathbf{E}}_2$ were both used for the strain computations of the muscle displacement fields.

The proposed phase analysis limits the detectable strains. An analysis on the detectable strains in done in the following paragraph.

2.4.3 Data analysis

The absolute minimum detectable Green Lagrange strain is determined by the maximum tag line frequency possible (the Nyquist frequency, with 2 pixels per period) by

$$\varepsilon_{N\min} = \tfrac{1}{2}\left(\left(\frac{2}{n_p}\right)^2 - 1\right) \tag{2.35}$$

where n_p is the number of pixels in one period (peak to peak distance) in the undeformed grid.
From eq.(2.35) it is seen that it is important not to choose the tag line frequency too close to the Nyquist frequency, otherwise one restricts himself detecting contraction: when $n_p = 2$ then $\varepsilon_{N\min} = 0$, so no contraction can be detected at all.

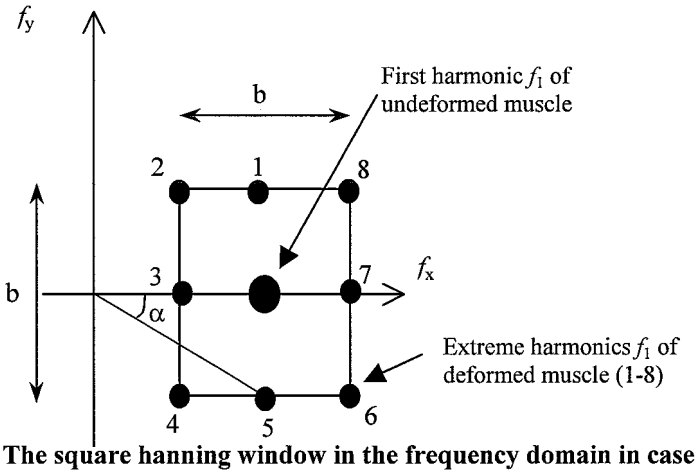

Figure 2.20: The square hanning window in the frequency domain in case of vertical tag lines. The numbers 1-8 are possible extremes that are detectable. 1 and 5 are pure shear. 3 and 7 indicate pure stretching and contraction respectively. The even numbers are combined strain/shear situations. α is the angle that relates to shear τ according to τ=tan(α).
In case of horizontal tag lines, the hanning window is placed on the f_y-axis.

The practical minimum and maximum detectable strain and shear are determined by the applied bandwidth (see figure 2.20). The minimum and maximum detectable deformed tag line frequencies $f_{\min}$ and $f_{\max}$ are

$$f_{\min} = f - \tfrac{1}{2}b \tag{2.36}$$
$$f_{\max} = f + \tfrac{1}{2}b \tag{2.37}$$

where f is the applied tag line frequency in the undeformed muscle and b the bandwidth.
The respectively minimum and maximum detectable stretch ratios $\lambda_{\min}$ and $\lambda_{\max}$ are

$$\lambda_{\min} = \frac{f}{f_{\max}} = \frac{f}{f + \tfrac{1}{2}b} = \frac{1}{1 + \tfrac{1}{2}BFR} \tag{2.38}$$
$$\lambda_{\max} = \frac{1}{1 - \tfrac{1}{2}BFR} \tag{2.39}$$

where BFR is the bandwidth frequency ratio. Finally, the minimum and maximum detectable Green Lagrange strains (if no shear is present) $\varepsilon_{\min}$ and $\varepsilon_{\max}$ are given by

$$\varepsilon_{\min} = \tfrac{1}{2}\left(\left(\frac{1}{1 + \tfrac{1}{2}BFR}\right)^2 - 1\right) \tag{2.40}$$

$$\varepsilon_{\max} = \tfrac{1}{2}\left(\left(\frac{1}{1-\tfrac{1}{2}BFR}\right)^2 - 1\right) \tag{2.41}$$

Eq.(2.41) shows that the bandwidth frequency ratio must not be chosen larger than 2, BFR<2.
In our case, the detectable strain extremes are:

BFR=1: $\varepsilon_{min} = -0.28$
$\varepsilon_{max} = 1.5$
BFR=1.2: $\varepsilon_{min} = -0.305$
$\varepsilon_{max} = 2.625$

The maximum detectable shear is derived as follows. The hanning window is chosen square, so the bandwidth is in 2 directions the same. See figure 2.20.

The maximum frequency detectable in the y-direction of a vertical line pattern is

$$f_{y\max} = \tfrac{1}{2}b = \tfrac{1}{2}BFR \cdot f_1 \tag{2.42}$$

So the maximum detectable pure shear is:

$$\tau_{\max} = \tan\alpha = \frac{\tfrac{1}{2}BFR \cdot f_1}{f_1} = \tfrac{1}{2}BFR \tag{2.43}$$

It can be seen from figure 2.20, that also shears of τ=1 can be detected if shear is combined with stretch (points 2 and 4).

2.5 Error analysis

Two kinds of tests were done to determine uncertainties in strain estimation:

- To test the accuracy of all steps taken in the whole procedure from the start (e.g. MRI signal to noise ratio) till the end (the estimation of the strains) a special strain field was determined. It is a strain field, estimated between images only containing undeformed tibialis anterior muscles (of the same rat and leg). Noise in pixel positions causes noise in strain estimation.
- Another accuracy test was done solely on the phase analysis and subsequently the strain determination. In this test, a simple artificial m. tibialis anterior contracted homogeneously in the y-direction with a stretch ratio λ_y=0.75 and lengthened in the x-direction with a stretch ratio λ_x=1.3125. See figure 2.21. The accompanying Green Lagrange strains are ε_y=-0.2188 and ε_x=0.3613. The bi-linear displacement field adjoined a region with no displacements. Horizontal and vertical tagging lines were applied with a sinusoidal intensity with the same frequency as in the in vivo experiments (a peak to peak distance of 4.27 pixels).

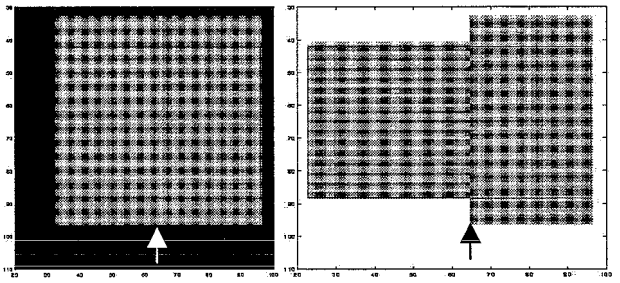

Figure 2.21: Artificial hind-leg, with m. tibialis anterior at rest (left) and stimulated (right), producing a bi-linear displacement field. The arrows mark the transition of the deforming and non-deforming regions. The horizontal & vertical tag lines are superimposed

3. Results

3.1 Selection of slice of observation

3.1.1 The anatomical coordinate system & the slice of observation

Figure 3.1 shows the 4 main images, used for the definition of the anatomical coordinate system and the slice of observation. The first 3 are part of the high resolution dataset. The 4th image is the xy-plane and the 5th image is the slice of observation, perpendicular to the xy-plane, with $\alpha = \beta = 0.6$. Next to the slice of

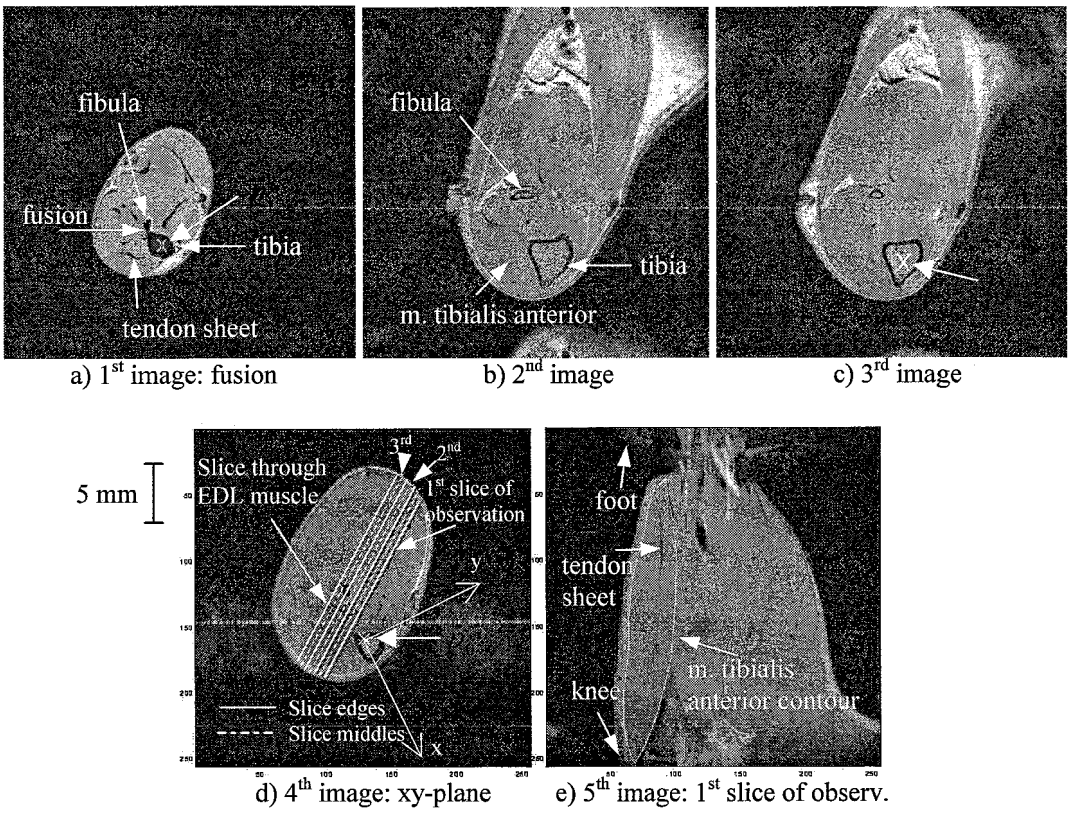

a) 1st image: fusion b) 2nd image c) 3rd image

d) 4th image: xy-plane e) 5th image: 1st slice of observ.

Figure 3.1: The 4 important images of the anatomical coordinate system and the slice of observation. a) is the image with the tibia-fibula fusion. In this image the center of gravity p_1 of the tibia was determined. b) is the image with the factor 2.8 tibia are increase in relation to the tibia area in image 1. c) is the image at 90% between image 1 and 2. Here, the tibia center of gravity p_2 is determined. d) is the image of the xy-plane with p_0 as the origin. The slices of observation are also depicted. e) is the 1st slice of observation.

observation a 2nd and a 3rd slice (respectively 1 and 2 mm in the direction of the fibula) has been used for tagging. From now on, whenever spoken of the slice of observation, the 1st is meant.
The tibialis anterior muscle is highlighted by the contour in figure 3.1e. At the knee side, at the right-hand side of the contour, the tibia is observed. At the left-hand side of the contour, the skin is clearly discernable.

3.1.2 3d reconstruction

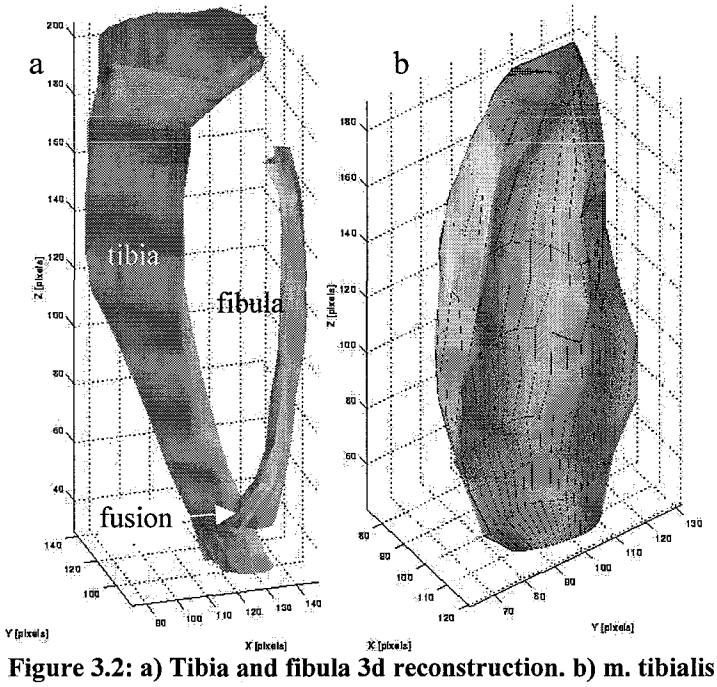

Figure 3.2: a) Tibia and fibula 3d reconstruction. b) m. tibialis anterior 3d reconstruction. These reconstructions are made with the dataset of Kretzers (1996).

Figure 3.2 shows the 3d reconstructions of the tibia and fibula (figure 3.2a) and the m. tibialis anterior (figure 3.2b). Figure 3.3 shows the 2 bones and the muscle together with the anatomical coordinate axes. The cross-section of a slice of observation (with α=0.5 and β=1) and the m. tibialis anterior is displayed also.

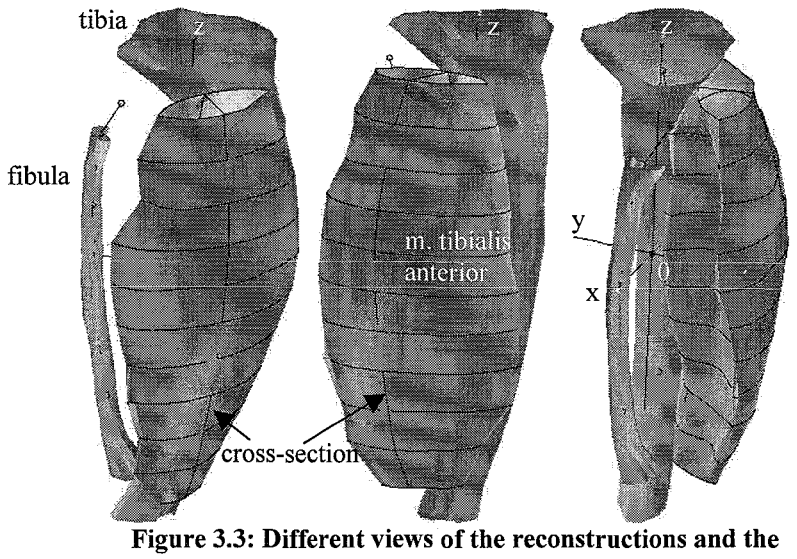

Figure 3.3: Different views of the reconstructions and the anatomical axes, together with the cross-section of a slice of observation and the m. tibialis anterior.

3.2 Displacement field

Figure 3.4 shows the unfiltered (top) and the real part of the filtered (bottom) tag-images of the slice of observation, in which also the region of interest (ROI) and the contour of the tibialis anterior muscle are displayed. The ROI is based on a high-resolution spin echo image and the images containing the deformed horizontal and vertical tag lines.
In figure 3.5 the displacement field (BFR=1) within the ROI is presented for the slice of observation.

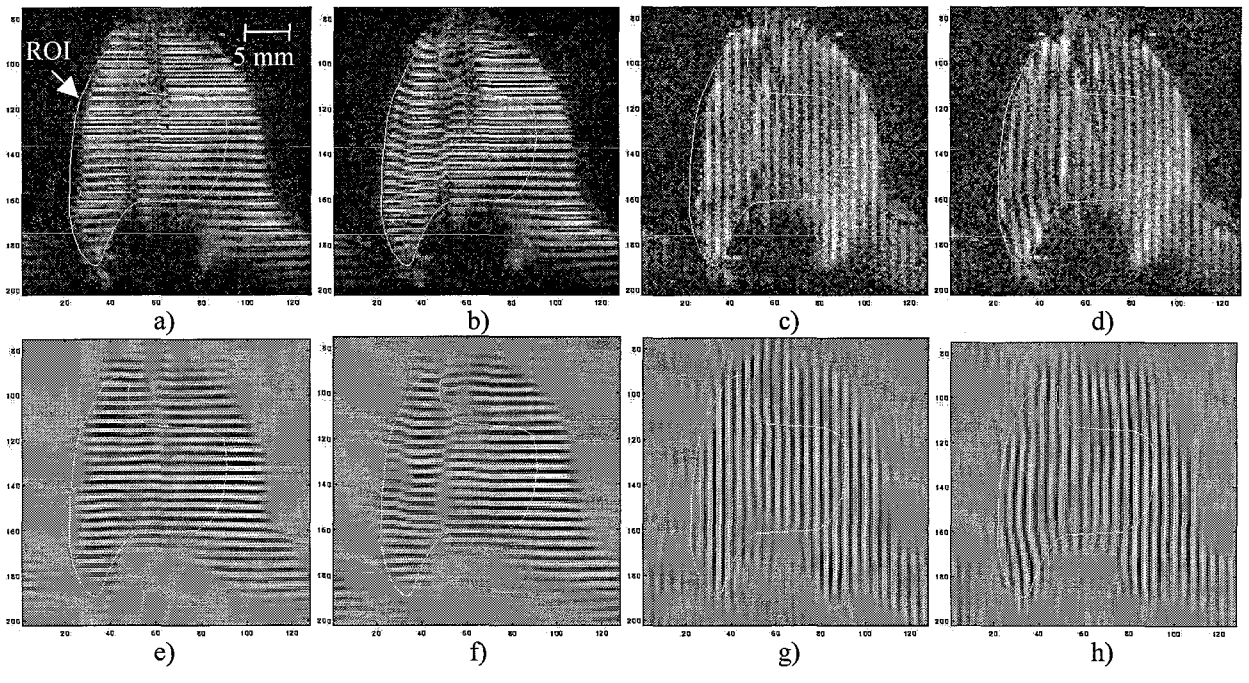

Figure 3.4: Unfiltered (top) and real part of filtered (bottom) tagged MR images. The contour presented is the region of interest. a, c, e and g are unstimulated, while b, d, f and h are images with stimulated m. tibialis anterior.

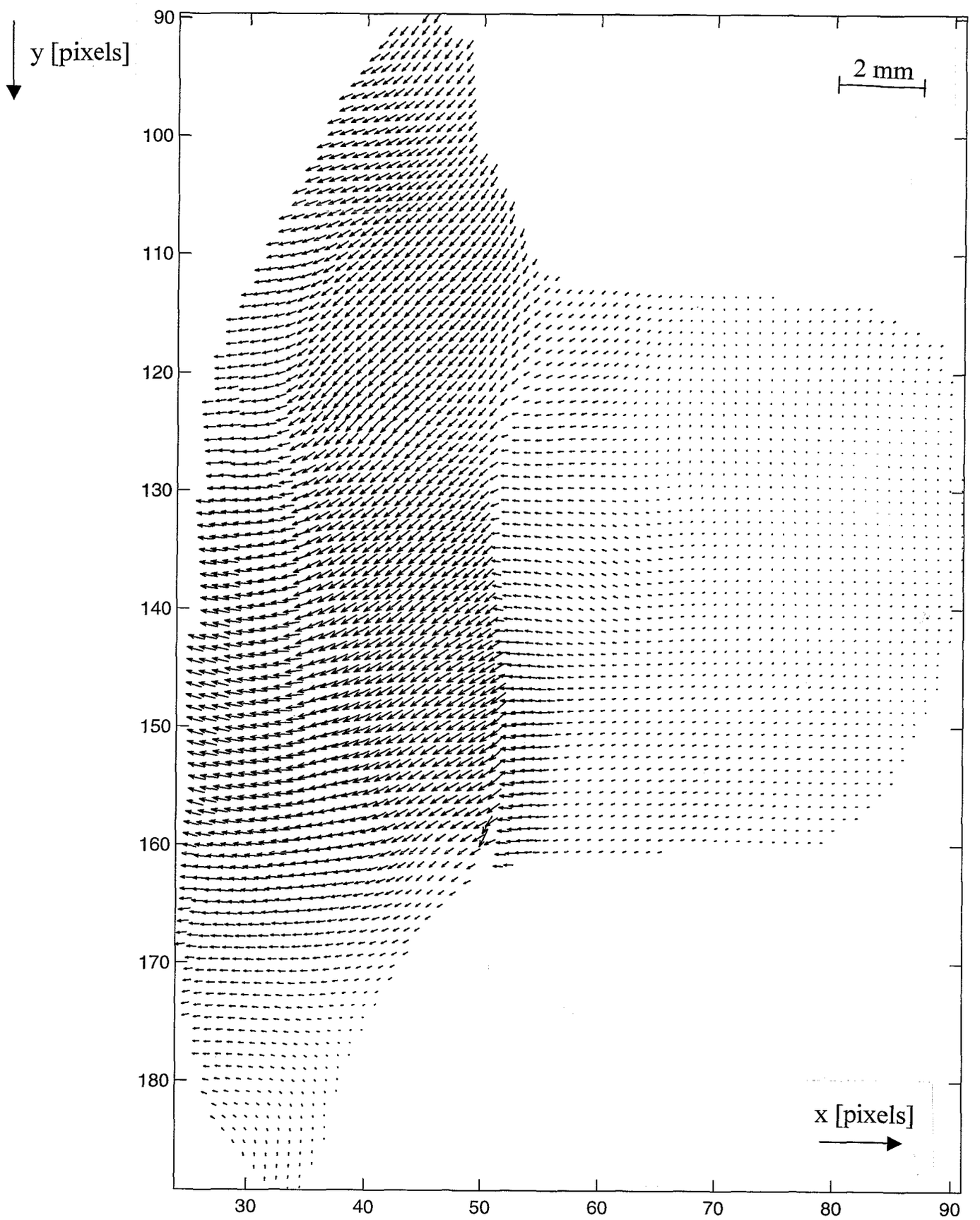

Figure 3.5: Displacement field of the slice of observation (BFR=1)

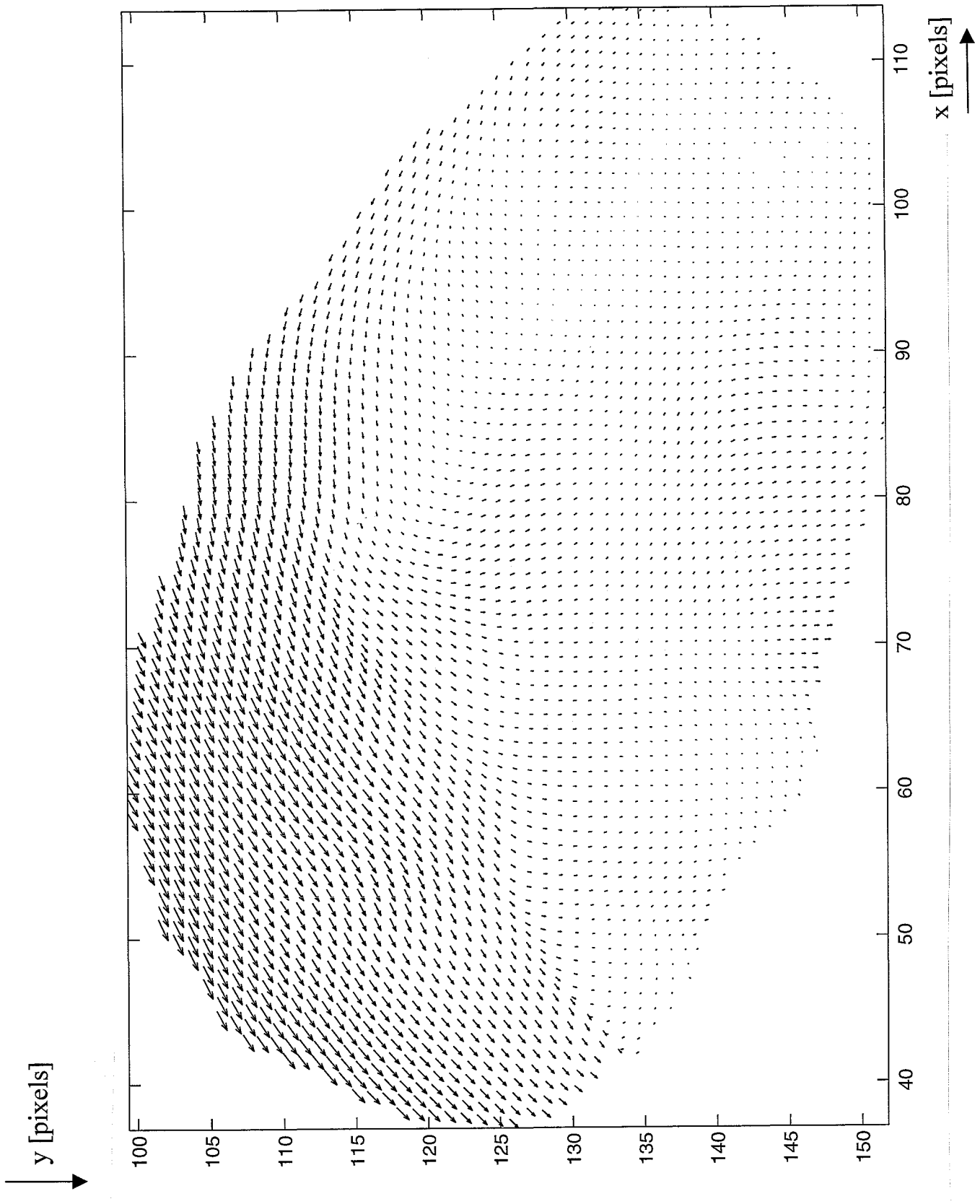

Figure 3.6: Displacement field for the xy-plane (BFR=1)

See figure 3.5. The displacements around (80,130), were set to zero. The reason for this will be explained in the discussion. It can be observed that the direction of the muscle tissue displacement was mainly downwards – towards the knee – and to the left. It pressed against the skin and the skin moved to the left along with the muscle. A sudden increase can be seen in the left displacements along the line x = 50. The displacements in the large area right of x = 50 were mainly zero. Along the contour of the m. tibialis anterior, at the region where it lies against the tibia (40,175) the displacements were also mainly zero. The two displacement vectors near (50, 160) were artifacts and will also be explained in the discussion.
Figure 3.6 shows the displacement field in the anatomical xy-plane. The displacing m. tibialis anterior is clearly seen. Because the tibialis muscle surrounds the m. extensor digitorum longus partly (figure 2.2), the latter was also displaced. It is seen at the top that the deformed muscle pulled the skin.

3.3 Strain field

Figure 3.7 through 3.9 show the principal strains of the first order estimated Green Lagrange strain tensor and the maximal shear of the first slice of observation. The displacement field from which the strain field was calculated, was determined with a BFR of 1 (figure 3.5). The following strain fields were also calculated and can be reviewed in appendix C:

- 1st order estimation, BFR=1.2 in the first slice of observation
- 2nd order estimation, BFR=1 in the first slice of observation
- 2nd order estimation, BFR=1.2 in the first slice of observation

Furthermore, the following strain fields were estimated for accuracy determination:

- 1st and 2nd order estimation, with BFR=1 and BFR=1.2 between 2 images, both containing the undeformed muscle of the slice of observation.
- As above, for the 2nd slice of observation.
- 1st and 2nd order estimation, BFR=1.2 in a simple simulated muscle with a known constant strain field.

3.3.1 First principal strain

See figure 3.7. In this strain field the first principal strain ε_{11} is displayed - defined as the most positive strain - in the deformed state.
The direction of the strain is given by the short lines, the strain magnitude by colour (from yellow to dark red is lengthening or stretching, from yellow to dark blue is shortening or contraction). The colour-range is scaled between $\varepsilon_{11} = -0.1$ and $\varepsilon_{11} = 0.5$. Thus, the first principal strain shows mainly lengthening.
When negative strains occur in the first principal strain at a certain region, it means that in that region the second principal strain is also negative.

At the right-hand side of the line x = 70, ε_{11} varied from 0 to 0.05. Locally at (90,125) the strain was $\varepsilon_{11} \approx -0.06$.

Between x=55 and x=70 the strain varied around 0.1. At (61,124) and (62,155) there were local strains of $\varepsilon_{11} \approx 0.27$ and $\varepsilon_{11} \approx -0.02$ respectively.

In the region $48<x<55$ large strains over 0.5 were observed.

Inside the blue m. tibialis anterior contour, the strains varied over a wide range from $\varepsilon_{11} = -0.03$ to 0.3. Locally at (42,163) a large strain over 0.5 existed. Contraction was seen at (43,152), mainly in the y-direction. Furthermore, there was a large area of lengthening ($\varepsilon_{11} \approx 0.2$) in the region $y > 155$. In the region $y<155$ areas of $\varepsilon_{11} = 0$ were observed and a long strain-band ($0.3<\varepsilon_{11}<0.45$) along the left-hand contour line.

This band followed at y = 110 a path to the mid-axis of the muscle. Lengthening was mainly seen in the x-direction, apart from some regions with zero strain and a region at (38,123).

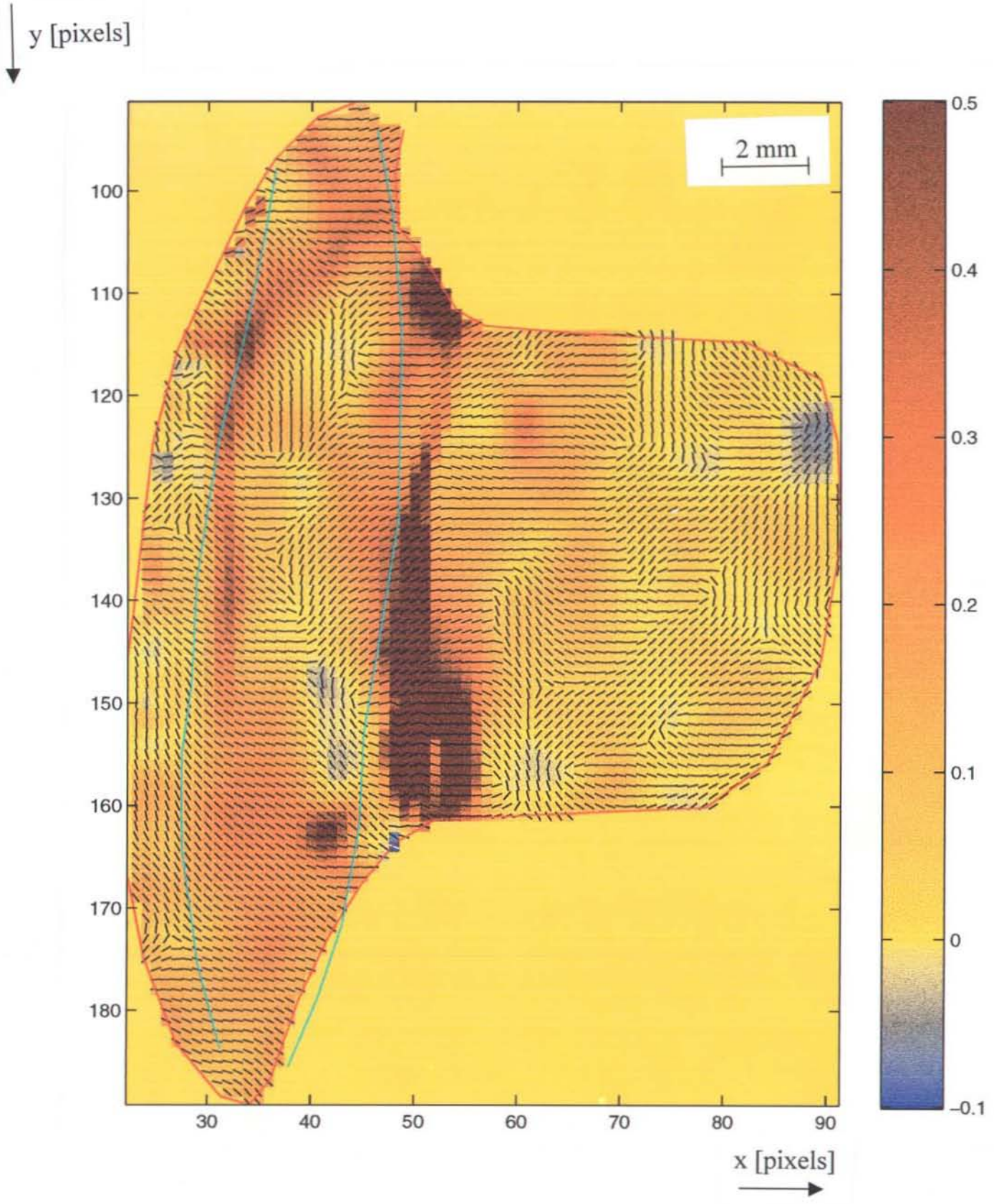

Figure 3.7: 1st order estimated strain field (1st principal strain ε_{11}) of the slice of observation (BFR=1). The magnitude of the strain is presented by the colours – zero strain by yellow, lengthening by orange and red and shortening by blue colours. The direction of the strains is presented by the line pieces. The blue continuous line is the deformed m. tibialis anterior contour.

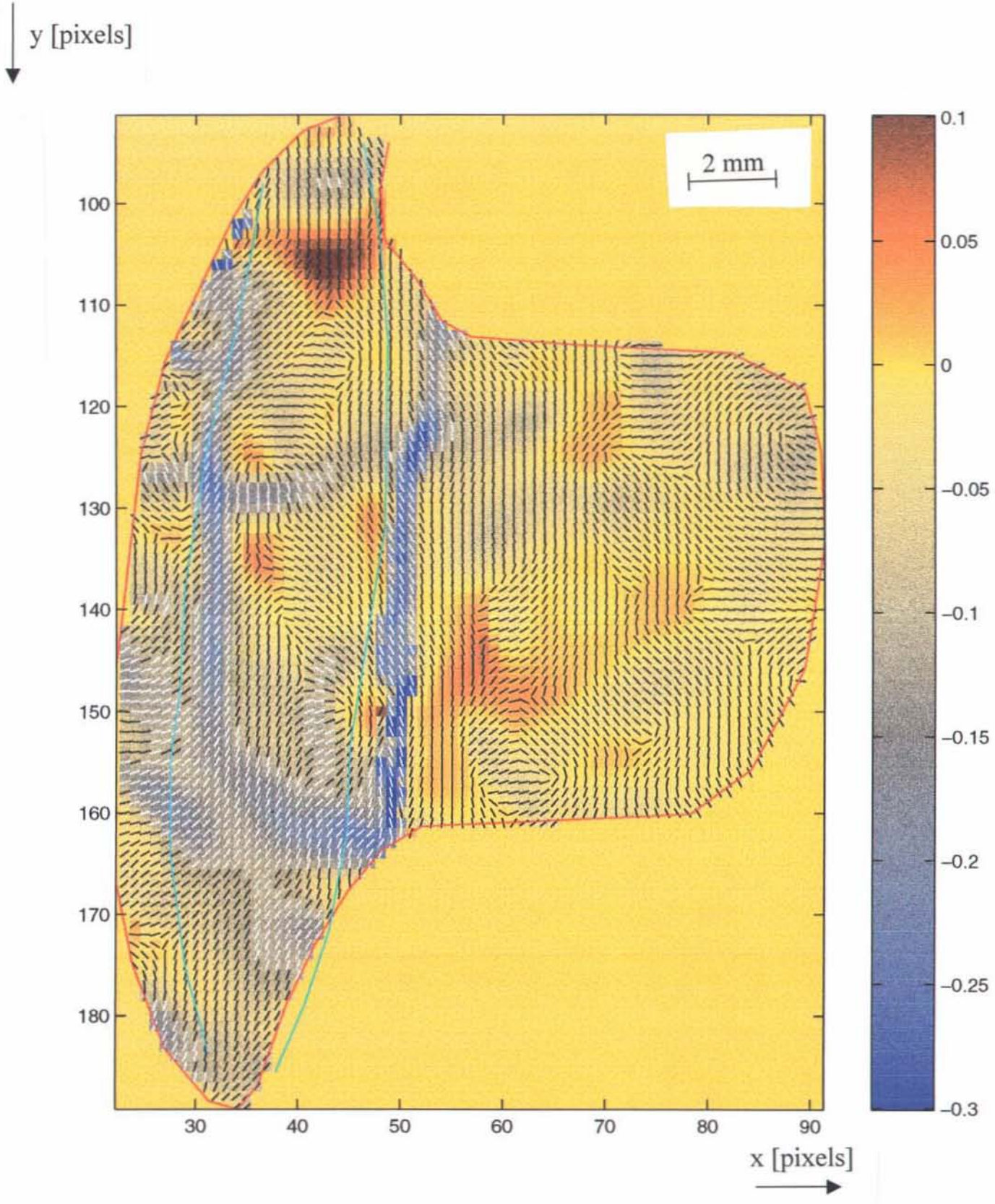

Figure 3.8: 1st order estimated strain field (2nd principal strain ε_{22}) of the slice of observation (BFR=1). The colours present the magnitude of the strain – zero strain by yellow, lengthening by orange and red and shortening by blue colours. The direction of the strains is presented by the line pieces. The blue continuous line is the deformed m. tibialis anterior contour.

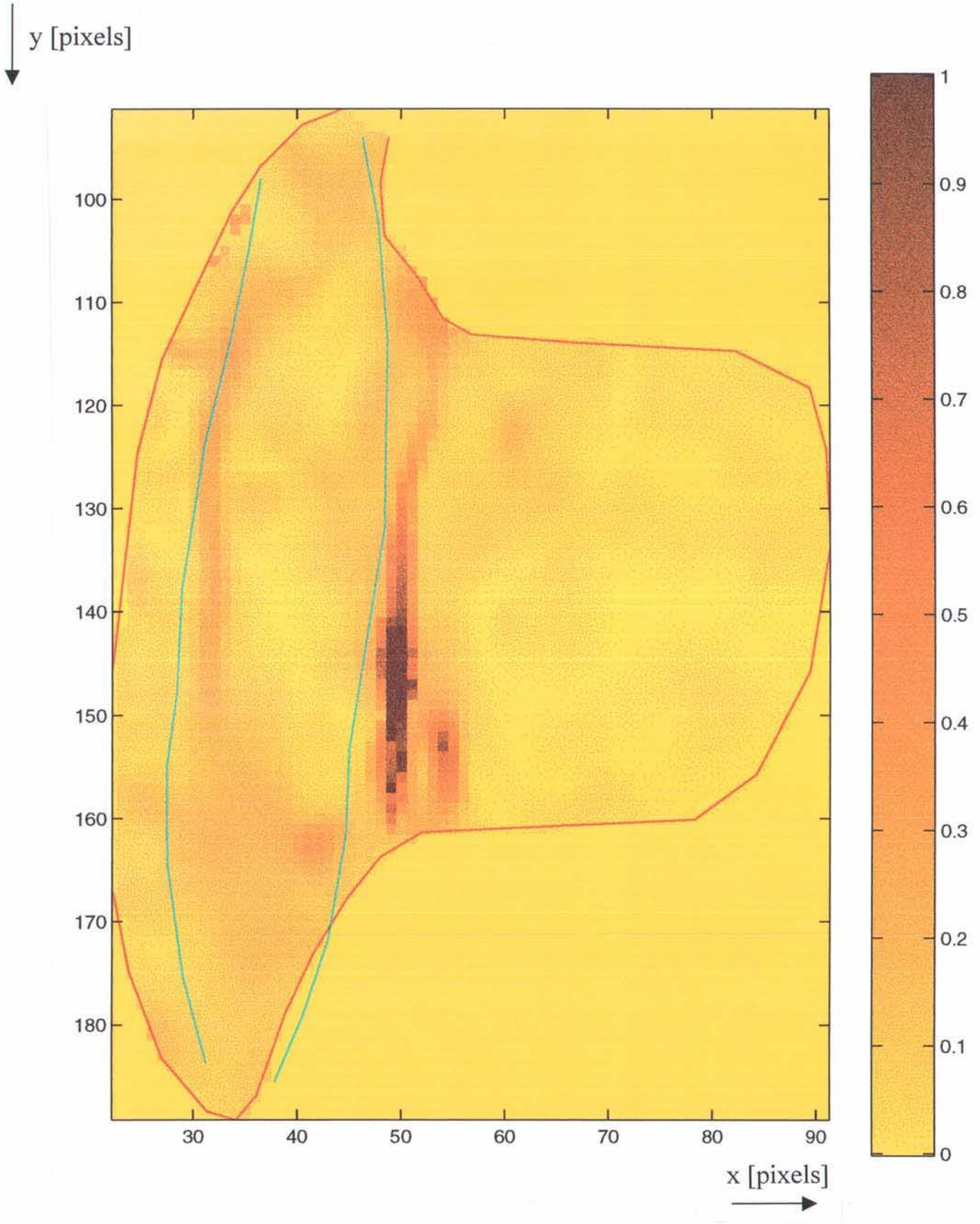

Figure 3.9: 1st order estimated largest shear ε_{12} of the slice of observation (BFR=1). The magnitude of the shear is presented by orange and red. The blue continuous line is the deformed m. tibialis anterior contour.

The contour of the deformed tibialis muscle - shown by the blue lines in figure 3.7 through 3.9 - were reconstructed from the high resolution image of the undeformed muscle (figure 3.1e) and the displacement field in figure 3.5. The line of the muscle contour at the left-hand side in figure 3.1e was clearly discernible along the skin. However, the contour line at the right-hand side was difficult to differentiate from the rest of the hind-leg and was subjected to inter-observer accuracy.

3.3.2 Second principal strain

See figure 3.8 for the second principal strain - the most negative strain. The second principal strain ε_{22} shows mainly contraction. A positive ε_{22} implies also a positive 1st principal strain.

Positive 2nd principal strains were seen at several regions, inside and outside the m. tibialis anterior. Especially in the muscle around (106,43) strains of $\varepsilon_{22} \approx 0.12$ occurred.

Two large bands of contraction ($\varepsilon_{22} = -0.15$) were observed along the left-hand and right-hand tibialis contours. In the region at $y > 150$, the strain-bands joined over the full width of the muscle, showing contraction parallel with the main muscle-axis (in the y-direction).

Above the region with the lengthening – in the region at $y < 100$ – a contraction of $\varepsilon_{22} \approx -0.10$ was observed. Around (38,120) a contraction of $\varepsilon_{22} \approx -0.06$ is seen in the x-direction. Around (42,150), also in the x-direction, a contraction of $\varepsilon_{22} \approx -0.10$ was observed.

3.3.3 Maximal shear

In figure 3.9 the maximal shear ε_{12} is presented. It is calculated from the principal strains ε_{11} and ε_{22} by

$$\varepsilon_{12} = \tfrac{1}{2}(\varepsilon_{11} - \varepsilon_{22}) \qquad (3.1)$$

At the right-hand side of the line $x = 55$ the shear varied approximately from 0 to 0.05. Large shear ($\varepsilon_{12}>1$) was observed at $x = 50$ and at (54,155).
Along the left-hand muscle contour a band of shear ($\varepsilon_{12}\approx 0.25$) was seen.
Within the muscle the shear varied from 0 to 0.35. The latter value was seen locally at (42,162).

3.3.4 Data of varied parameters

The data described in the paragraphs 3.3.1, 3.3.2 and 3.3.3 and data with regard to varied parameters in the slice of observation are summarized in the following tables:

	minimum	**maximum**	**median**
ε_{11}	-0.109	3.64	0.0860
ε_{22}	-0.386	0.114	-0.0391
ε_{12}	0.0017	1.99	0.0678

Table 3.1: slice of observation. BFR=1. First order estimation $\hat{\mathbf{E}}_1$

	minimum	**maximum**	**median**
ε_{11}	-0.164	5.47	0.0824
ε_{22}	-0.4125	0.115	-0.0392
ε_{12}	0.0012	2.73	0.0623

Table 3.2: slice of observation. BFR=1.2. First order estimation $\hat{\mathbf{E}}_1$

	minimum	maximum	median
ε_{11}	-0.0704	14.7	0.0781
ε_{22}	-0.498	0.0941	-0.0332
ε_{12}	0	7.34	0.0571

Table 3.3: slice of observation. BFR=1. Second order estimation $\hat{\mathbf{E}}_2$

	minimum	maximum	median
ε_{11}	-0.172	12.97	0.0838
ε_{22}	-0.499	0.164	-0.0386
ε_{12}	0	6.63	0.0625

Table 3.4: slice of observation. BFR=1.2. Second order estimation $\hat{\mathbf{E}}_2$

It can be seen that all the median values of the calculated strains were about the same. The maximal difference for ε_{11} was 0.006, for ε_{22} it was 0.008 and for ε_{12} the maximal difference between the calculations was 0.01. The largest differences existed among the maximal and among the minimal strains. Especially the 2nd order estimations showed large maximums.
All values in tables 3.1 through 3.4 were based on the whole ROI, as presented in figures 3.7 through 3.9. If the m. tibialis anterior is observed solely – within the blue lines in figure 3.7 through 3.9 – the median value is 0.15 for the 1st principal strain and -0.07 for the 2nd principal strain (BFR=1 and first order estimation).

3.4 Error analysis

3.4.1 Strain field between 2 undeformed muscles

Figure 3.10 and 3.11 show respectively the first and second principal strains of one of these tests (see also table 3.5). Table 3.6 and 3.7 present summarized results of the other two tests

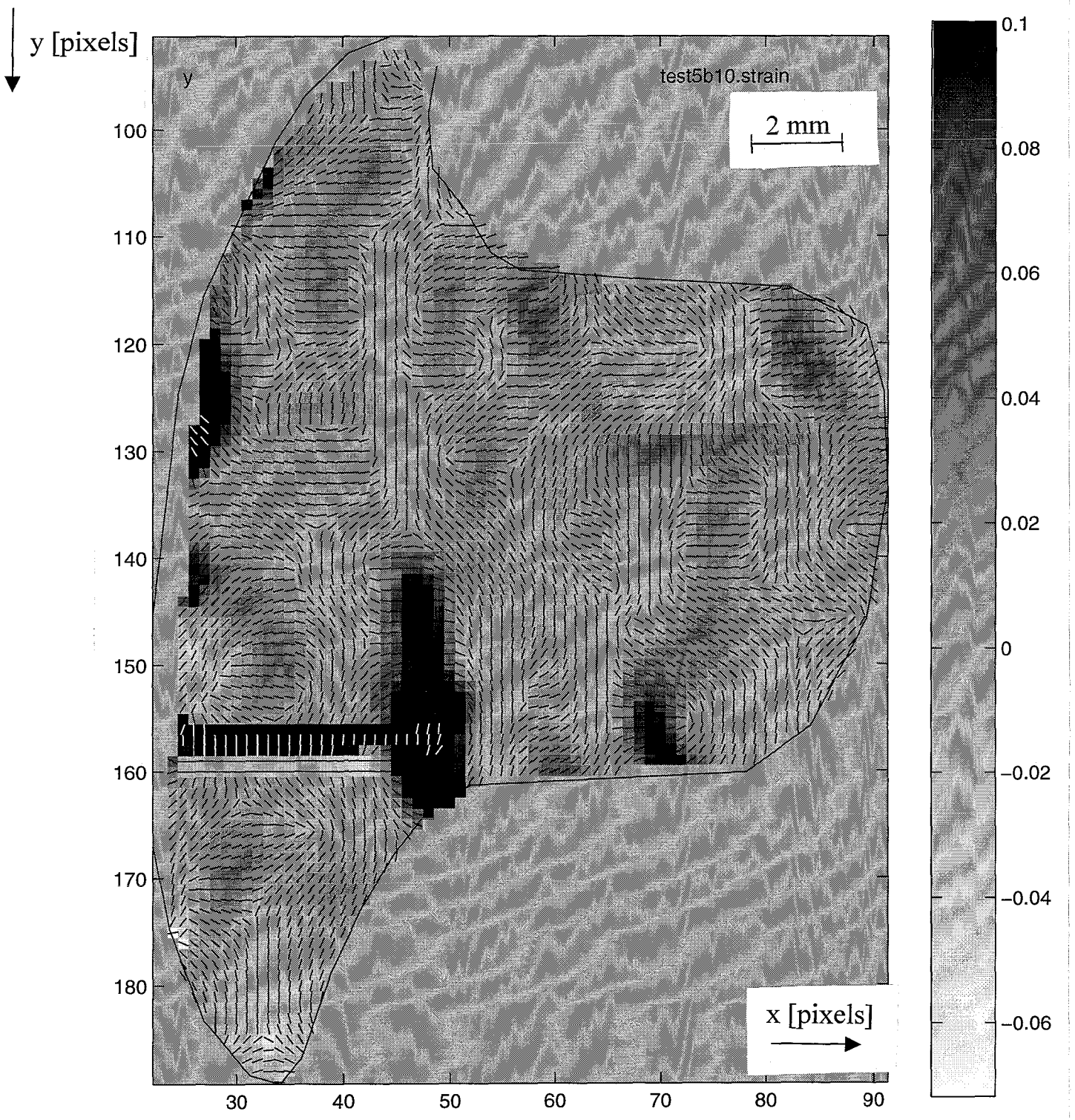

Figure 3.10: 1st order estimation of 1st principal strain (BFR=1) between 2 undeformed muscles. The gray values present the magnitude of the strain. The line pieces present the direction of the principal strains. At 155<y<161 a band of large strains is observed.

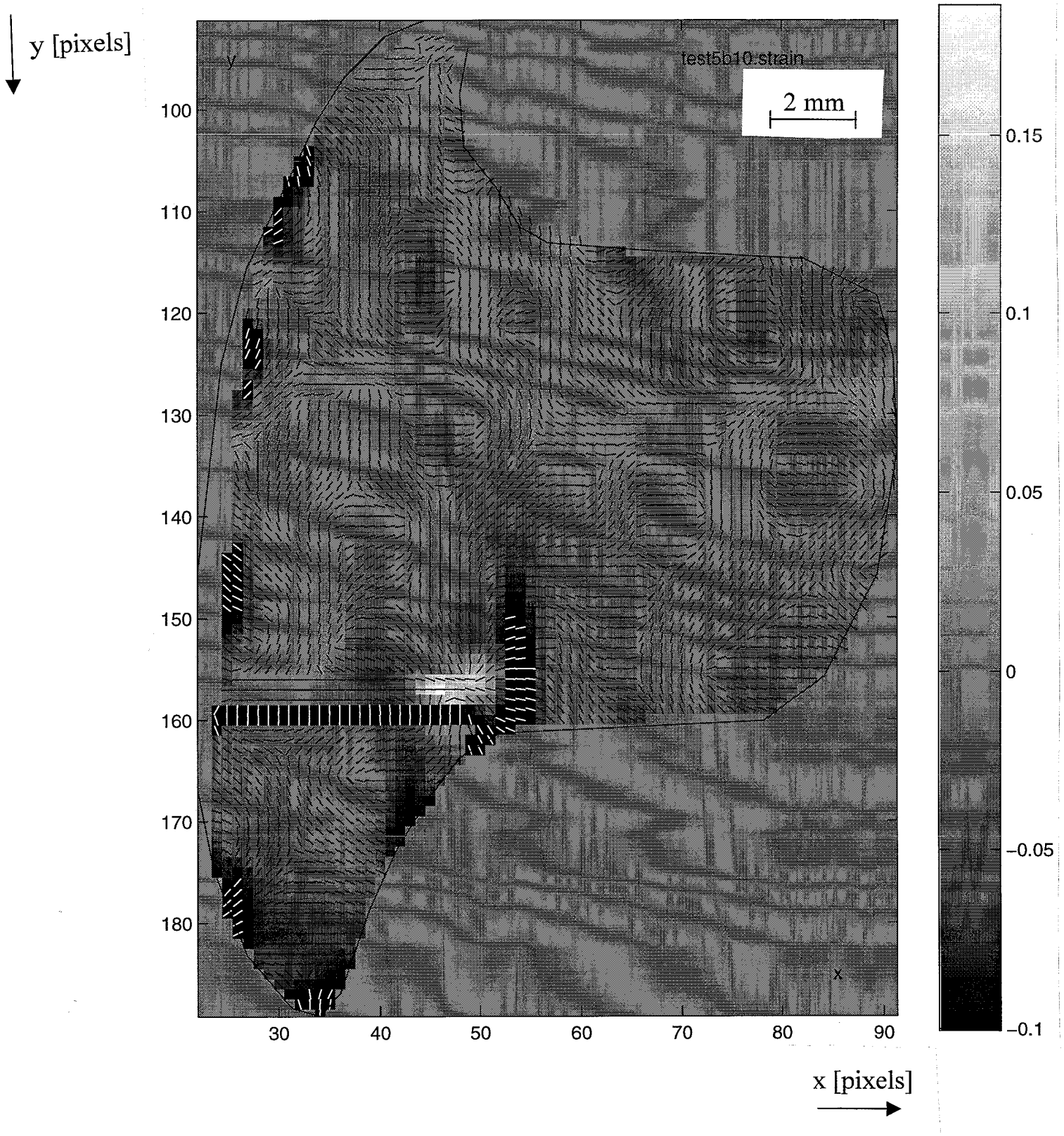

Figure 3.11: 1st order estimation of 2nd principal strain (BFR=1) between 2 undeformed muscles. The gray values present the magnitude of the strain. The line pieces present the direction of the principal strains. At 158<y<161 a band of large negative strains is observed. Around (50,158) large positive strains are observed.

	minimum	maximum	median
ε_{11}	-0.0716	1.28	0.0138
ε_{22}	-0.354	0.186	-0.0159
ε_{12}	0	0.644	0.0163

Table 3.5: Noise in strains. BFR=1. First order estimation $\hat{\mathbf{E}}_1$

	minimum	maximum	median
ε_{11}	-0.0786	1.91	0.0139
ε_{22}	-0.428	0.201	-0.0160
ε_{12}	0	1.09	0.0162

Table 3.6: Noise in strains. BFR=1. Second order estimation $\hat{\mathbf{E}}_2$

	minimum	maximum	median
ε_{11}	-0.0236	0.145	0.0130
ε_{22}	-0.0977	0.0401	-0.0114
ε_{12}	0	0.114	0.0123

Table 3.7: Noise in strains. BFR=1. Second order estimation $\hat{\mathbf{E}}_2$

The largest differences between the tables are seen in the strain minimums and maximums that exist in the strain fields. Especially between table 3.5 and 3.6 on one side and table 3.7 on the other. This is explained by looking at figure 3.10 and 3.11. It is seen that a horizontal band of large strains exists at $155<y<161$. Apart from this band, it can be seen in figures 3.10 and 3.11 that most errors also occur at the edges of the ROI and in the region around (47,150) where $\varepsilon_{11} \approx 0.1$.
If the principal strains are compared mutually, it is observed that their medians presented in the 3 tables are nearly equal. The numbers indicate a strain uncertainty of 0.01 on $|\varepsilon_{11}|$, $|\varepsilon_{22}|$ and $|\varepsilon_{12}|$.

3.4.2 Artificial muscle

Figure 3.12 shows the displacement field of the homogeneously deforming artificial muscle. Figure 3.13, 3.14 and 3.15 show respectively the principal strains ε_{11}, ε_{22} and ε_{12}. The tibialis transition is at x=63.5, as is clearly seen by the large strains that exist there. The right-hand side of x=63.5 is at rest (which shows $\varepsilon_{11}=\varepsilon_{22}=0$); the left-hand side of x=63.5 is the contracting artificial m. tibialis anterior (showing exactly $\varepsilon_x=\varepsilon_{11}=0.3613$ and $\varepsilon_y=\varepsilon_{22}=-0.2188$ for the major part).

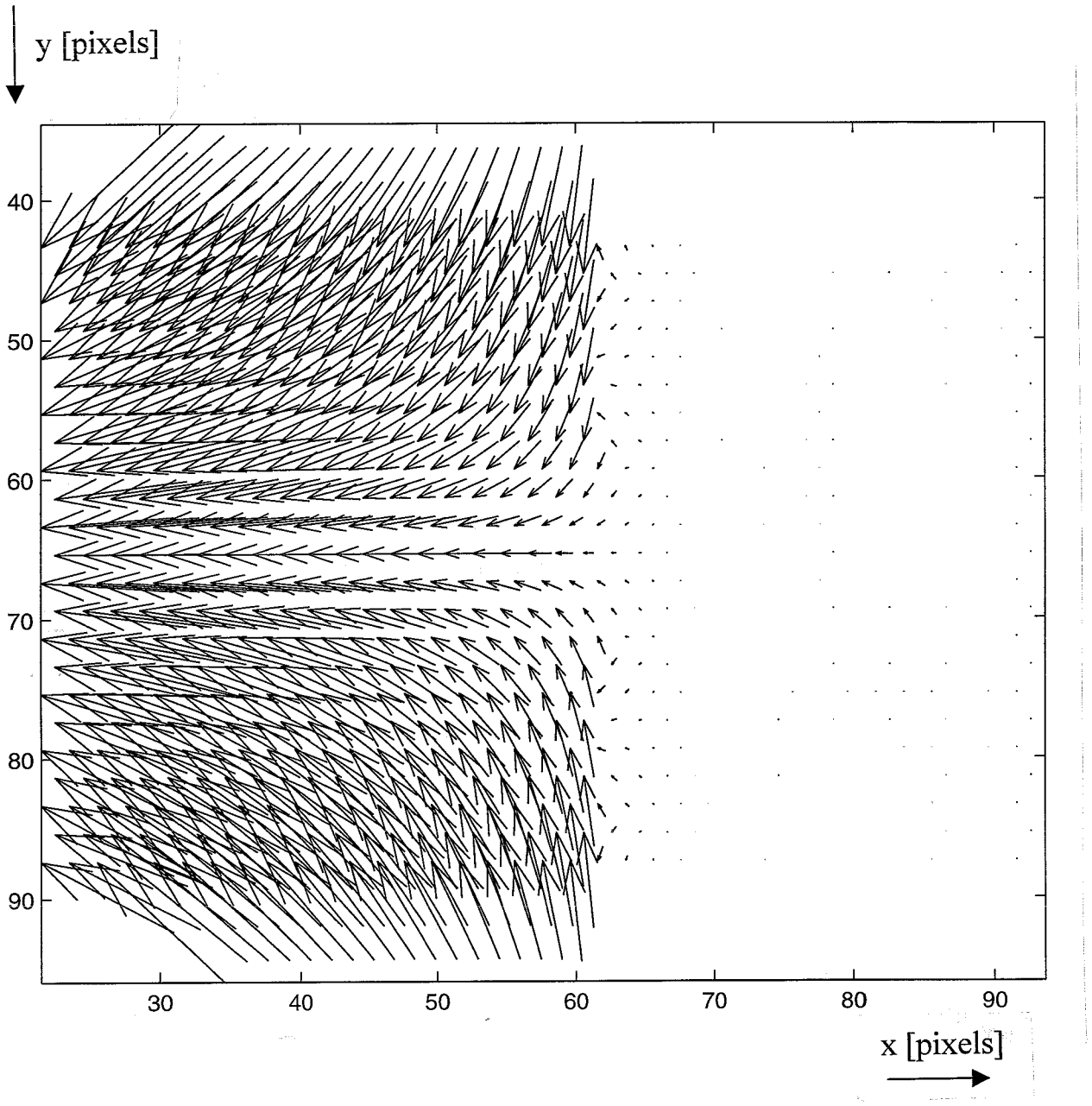

Figure 3.12: Displacement field of the artificial hind-leg (BFR=1.2)

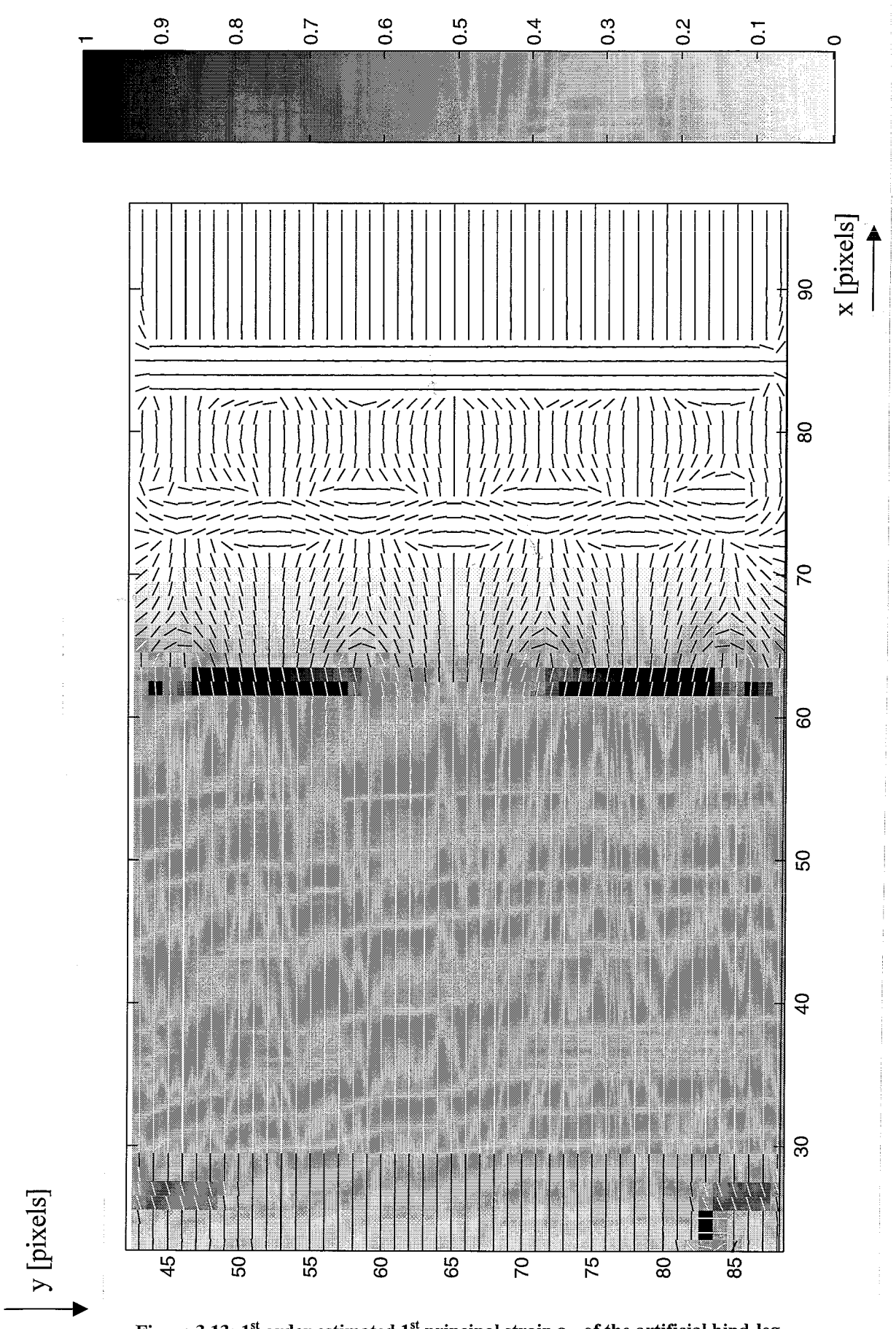

Figure 3.13: 1st order estimated 1st principal strain ε_{11} of the artificial hind-leg (BFR=1.2). The gray values represent the magnitude of the strains. The line-pieces represent the direction of the strains.

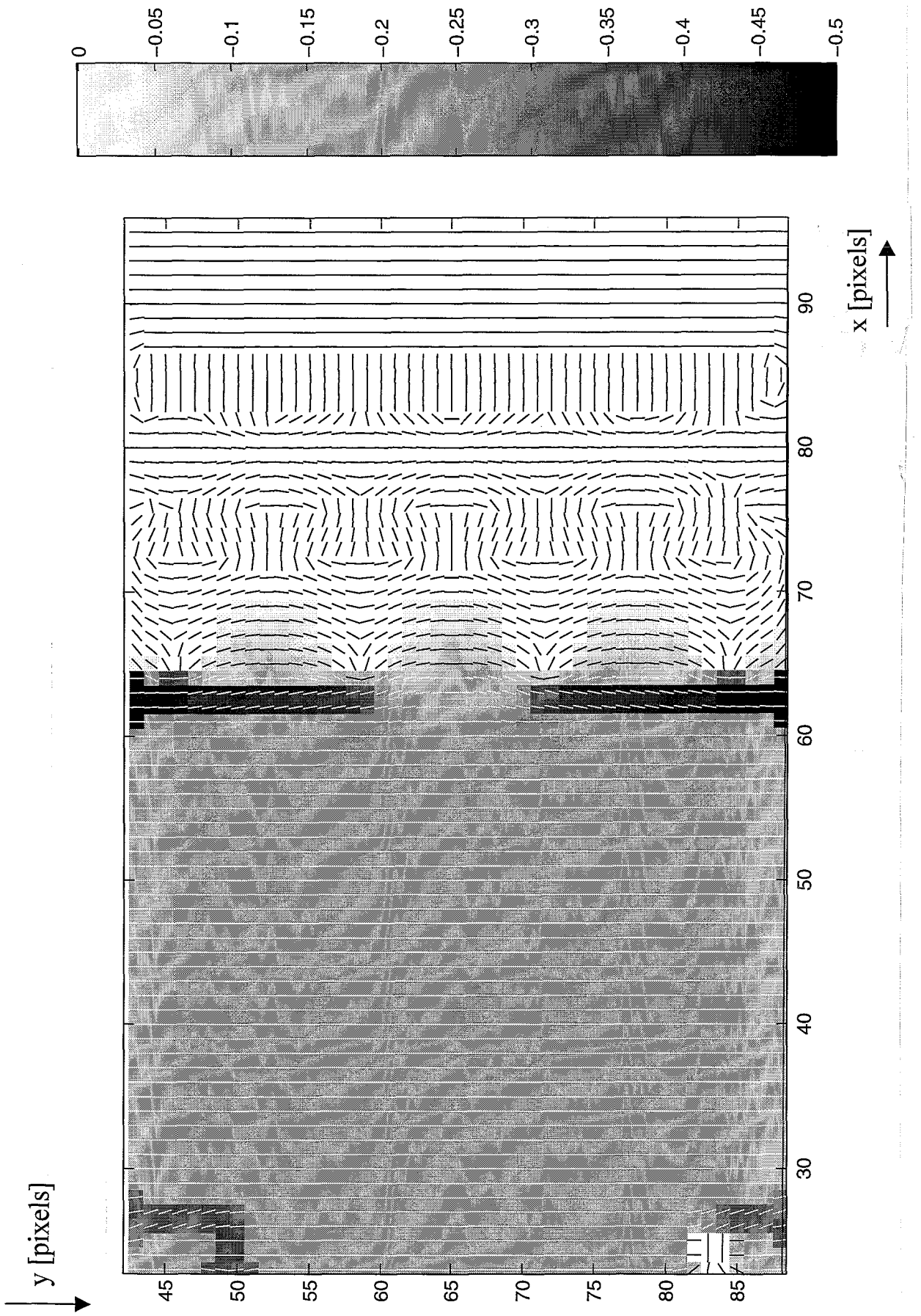

Figure 3.14: 1st order estimated 2nd principal strain ε_{22} of the artificial hind-leg (BFR=1.2). The gray values represent the magnitude of the strains. The line-pieces represent the direction.

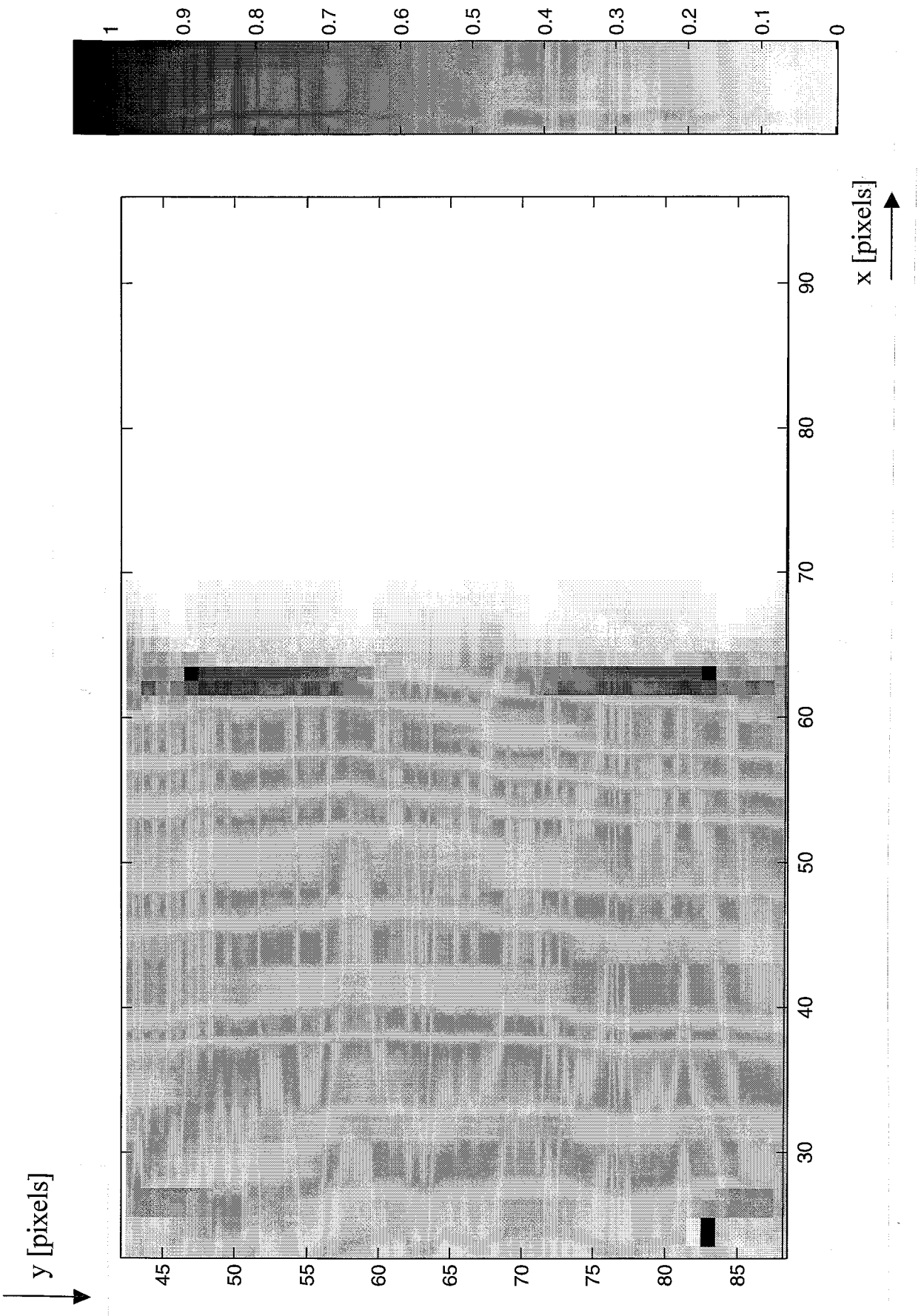

Figure 3.15: 1st order estimated largest shear ε_{12} of the numerical hind-leg . The gray values represent the magnitude of the shear. (BFR=1.2)

4. Discussion

The problems and errors in
- the selection of the anatomical coordinate system;
- the selection of a slice of observation in the m. tibialis anterior;
- determination of a displacement field from MR tagged images;
- estimation of a strain field from this displacement field;

will be discussed in this chapter.

4.1 Anatomical coordinate system

The intention of the anatomical coordinate system and subsequently the selection of a slice of observation is to acquire a reproducible slice through the tibialis anterior muscle.

The main sources of error of the anatomical coordinate system are:

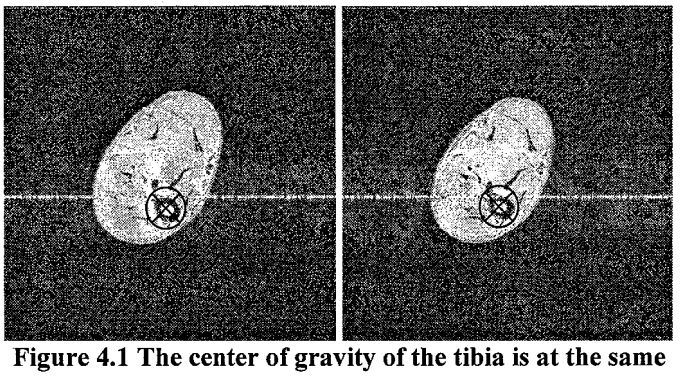

Figure 4.1 The center of gravity of the tibia is at the same location before (left) and after the fusion (right) (±1 pixel)

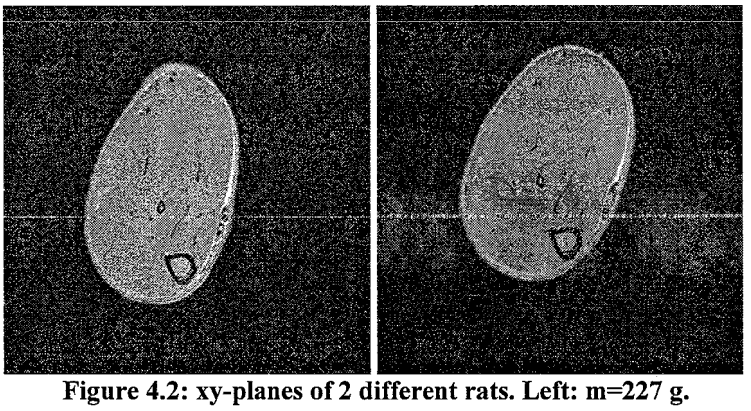

Figure 4.2: xy-planes of 2 different rats. Left: m=227 g. Right: m=248 g

- The coordinate system depends mainly on the observer's interpretation relating to bone and muscle contours. Contours of adjoining muscles cannot be differentiated unambiguously. They are a greater source of error with respect to the centers of gravity than muscle-skin or muscle-bone transitions.

Because the coordinate system is mainly based on the bone-structure, the errors on the centers of gravity will be not too large, but are still to be quantified.

- There's an uncertainty of 0.4 mm in the localization of the centers of gravity of the tibia. The contiguous slices in the high-resolution dataset are situated at discrete distances of 0.4 mm. So the tibia-fibula fusion takes place somewhere in the range of 0.4 mm between two neighbouring slices - excluding the observer's interpretation of the fusion. This applies also to the images showing tibia area increase by a factor of 2.8. The error in locating the 2 centers of gravity of the tibia cross-section for defining the anatomical z-axis is small. The error is becoming relevant when between two adjoining slices the in-plane positions of the centers of gravity of the tibia differ greatly. However, this is not the case, as can be seen in figure 4.1.

Figure 4.2 shows the xy-planes of 2 different rats. It is observed that the cross-sections are nearly the same. Small differences are caused by the fact that the rats were of different mass.

4.2 Selection of slice of observation

In figure 4.3, 3 slices of observation are presented for 3 different rats. Comparison between the slices is difficult, because they are all chosen different. The image in figure 4.3a) is the mid-sagittal plane of the tibialis anterior muscle of a partly dissected dead rat, defined by and subjected to Kretzers' experiment (1996). The skin and the posterior muscles were removed. The ankle angle was 90°, slice thickness 0.5 mm. Figure 4.3b) and c) present 2 slices of observation of 2 different rats used in our experiments (slice thickness 0.4 mm, ankle angle 110°). It is clearly seen that the different ankle angles influence the shape of the m. tibialis anterior between 4.3a) on one side and 4.3b) and c) on the other. The image in figure 4.3b) was made with factors α=0.5 and β=0.5, which are in fact too small. The image in figure 4.3c) was made with α=β=0.6. The reason for these different factors is as follows:

A tagged FLASH image contains poor tag lines near the tibia and fibula. The explanation for this phenomenon is that cortical bone and soft tissue have different NMR susceptibility. The result of this difference in susceptibility combined with the use of a small flip angle in the FLASH sequence, is a signal disturbance around bone. The solution to avoid tag disturbances, is to choose the slice of observation such (α=β=0.6) that no tibia appears in the middle of the image. The tibia isn't seen in the middle of figure 4.3a), but that's because the slice thickness is only 0.5 mm. In our FLASH sequence, a slice thickness of 1 mm had to be used, exposing the tibia. Figure 4.3b) shows that the factors α=0.5 and β=0.5 are too small, because the tibia is already in the image, despite the small slice thickness.

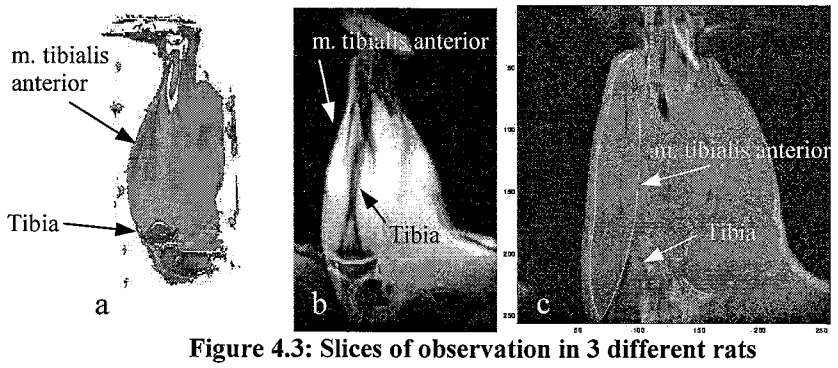

Figure 4.3: Slices of observation in 3 different rats

4.3 Displacement and strain fields

4.3.1 Tagging

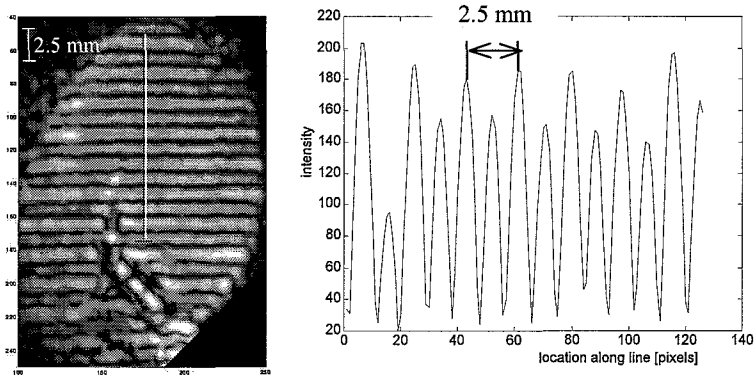

Figure 4.4: Left: Tags in skeletal muscle after Δ=150 ms. Right: The intensity along the white line. The dephasing gradient in the SPAMM sequence was such, that the peak to peak distance should be l=2.5 mm. In this centric encoded image, l=1.25 mm.

The distances from peak to peak in the images with horizontal tag lines is halved in relation to the theoretical expected distance (equation 2.10). So a doubling of tags is observed (see figure 4.4). The extra lines are of lesser intensity. This effect is not seen in the images with the vertical tag lines. Compare also figure 4.5a with figure 4.5b. In figure 4.5a the peak to peak distance is 0.5 mm, but should be 1 mm. The peak to peak distance in figure 4.5b is and should be 1 mm.

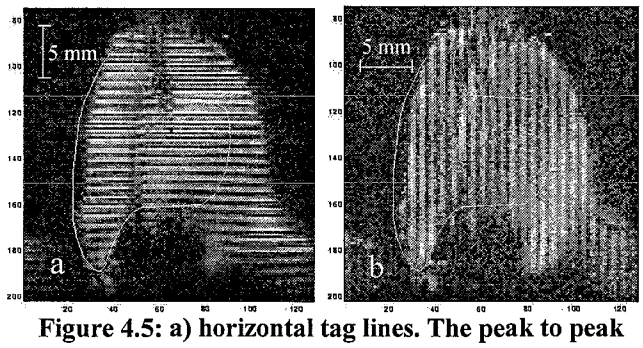

Figure 4.5: a) horizontal tag lines. The peak to peak distance should be *l*=1 mm, but is *l*=0.5 mm. b) vertical tag lines. The peak to peak distance is equivalent with the theoretical distance *l*=1 mm.

The combination of centric sampling and a 0° tagging angle influences a conventional MR image. A conventional MR image is the absolute representation of the Fourier transformation of the k-space, the so-called magnitude spectrum (like the images in figure 4.5). This means that negative magnetization $-M_z$ appears positive in the magnitude spectrum and as a consequence a doubling of number of tags occurs. Usually this does not happen in monotonic sampling, because when the center of the k-space is sampled at half the total scan-time, the negative magnetization has already passed the zero-line due to T_1 relaxation (see figure 4.6).

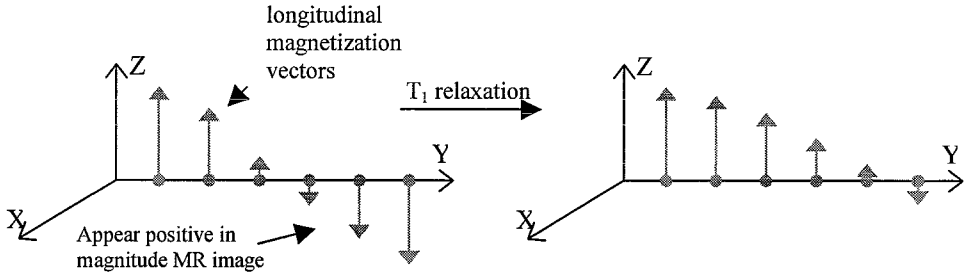

Figure 4.6: Loss of saturation due to T_1 relaxation

Because the FLASH imaging sequence started Δ=100 ms after application of the tagging lines, these extra lines appeared with less intensity due to T_1 relaxation.

The reason that the extra tag lines did not appear in the images with the vertical tag lines, was caused by the read-out and phase-encode direction. The read-out gradient was applied along the image y-axis (perpendicular to the horizontal tag lines, parallel with the vertical tag lines); the phase-encode along the image x-axis. In case of a centric phase-encoding, the read-out starts in the middle of the k-space from bottom to top (or from top to bottom, but that's irrelevant).
Now, if horizontal tag lines were applied, the most information (two peaks, see the white arrows in figure 4.7a) was situated exactly along the first read-out gradient (gray arrow in figure 4.7a). So the major part of the tag line information was read 100 ms after application of the horizontal lines. If vertical tag lines were applied, the most information was situated in the middle of the image, from left to right. But the major parts of the two peaks (white arrows in figure 4.7b, the peaks are already relaxed) were read out approx. 1.1 s (at half the total image time 0.5*2 s in case of a tag width l = 1 mm, plus 100 ms) after application of the vertical lines. Thus the negative magnetization had already passed the zero-line due to T_1 relaxation. If the read-out and phase-encode directions are switched in case of vertical tag lines, the problem is omitted.

Tag doubling is harmful in 2 ways. When the tag frequency approaches the Nyquist frequency – the maximal possible frequency that can be sampled (2 pixels per period) – a sticking of tag lines will appear and cannot be separated. Secondly, a 2nd harmonic appears in the frequency domain. If large positive and negative strains exist in the deformed muscle, the 1st and 2nd harmonic will overlap and displacements cannot

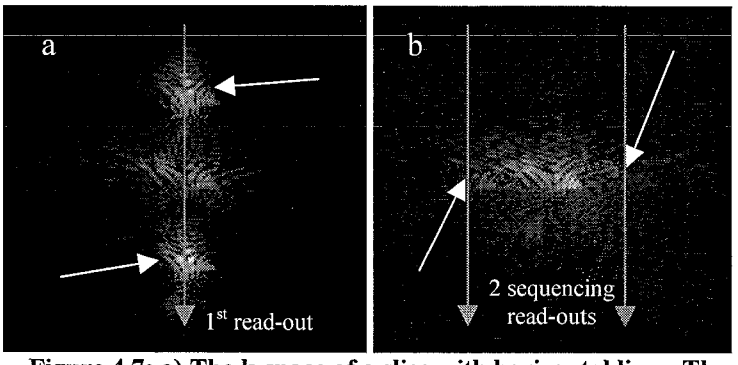

Figure 4.7: a) The k-space of a slice with horizontal lines. The white arrows mark the first positive and negative harmonics f_1. In case of centric encoding and a read-out in the y-direction, they are sampled in the beginning of the FLASH sequence (marked by the gray arrow). b) The k-space of a slice with vertical lines. The white arrows mark also f_1, but are already heavily relaxed. In case of centric encoding and a read-out in the y-direction, they are sampled at approximately half the total imaging time (marked by the gray arrows).

be determined properly.

A way to resolve the tag doubling problem is to prevent it by presenting the negative magnetization as it is. Therefore, phased spectra can be calculated. Fourier transformation of the time domain signals (along k_x in the k-space) yields the frequency spectrum. Now, a pure phase image can be produced by interactively adjusting phase errors in the spectrum. These are the zero order phase φ_0 and the first order phase φ_1 of the rotating spins. The zero order phase φ_0 exists due to a phase offset and the first order phase φ_1 is caused by hardware imperfections and/or timing errors. This means that φ_1 depends linearly on the resonance frequency ω. For a more extensive elaboration is referred to De Graaf (1998).

However, the phase correction could not be carried out properly, because zero and first order phase correction was not sufficient. As can be seen in figure 4.8, the platinum stimulation electrode has great

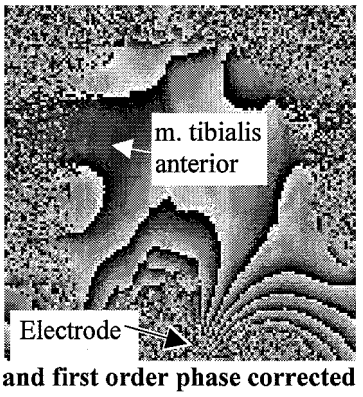

Figure 4.8: Zero and first order phase corrected phased image. It is observed that the electrode has great influence on the phases. After correction, the hind-leg should look uniform.

influence on the magnetic field and as a consequence on the phases of the spinning nuclei. Also, experience with phased images only existed in case of spin echo images. The influence of phase corrections on images made with a gradient echo sequence (as was the case) has to be examined.
As a result, conventional magnitude images were produced. In some images, sticking of tags occurred and were kept out of the displacement determination. Overlap between the 1st and 2nd harmonics did not occur.

Comparison of tagging results
Comparing results of deformed horizontal tag lines of our experiments with the results of the experiments by Ossevoort (1997) – figure 3.4b and figure 4.9b – it is observed that the muscle in both images displaces mostly towards the knee (which is in fig 4.9 at the top). We suspect that the v-shaped structure is caused by the m. extensor digitorum longus, because the m. tibialis anterior is a small muscle (only the right part,

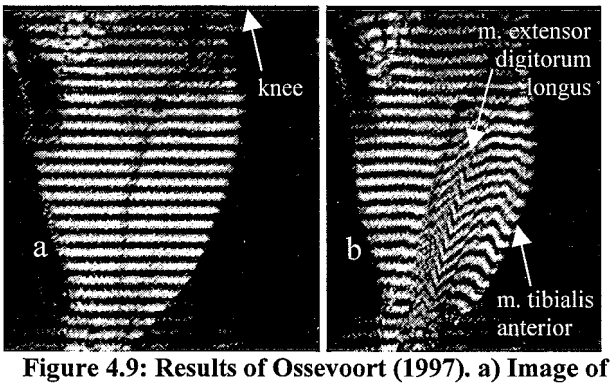

Figure 4.9: Results of Ossevoort (1997). a) Image of rat hind-leg with an undeformed horizontal tag line pattern. b) The deformed situation. It can be seen that the m. extensor digitorum longus also contracts. The images presented are an average of 16 images.

until the first discontinuity is seen from right to left). It was seen in a different slice of observation in our experiments that the extensor digitorum muscle also contracted.
The images by Ossevoort have a higher signal to noise ratio, but then, they are a result of 16 averaged measurements. The images in figure 3.2 are made in one shot. For the calculation of the displacement field, 2 shots are acquired (one with vertical and one with horizontal lines).

4.3.2 Phase analysis of complex amplitude

Weak signals
On the very limited experience we have found that the proposed phase analysis is sensitive to weak MRI signals. Three kinds of regions of weak signal influence the phases within the region of interest: signals that emanate outside the ROI from air, signals emanating from tissue near bone and signals emanating from tissue near the electrode (see figure 4.10). Regions of weak signal inside the ROI can influence the displacement field.

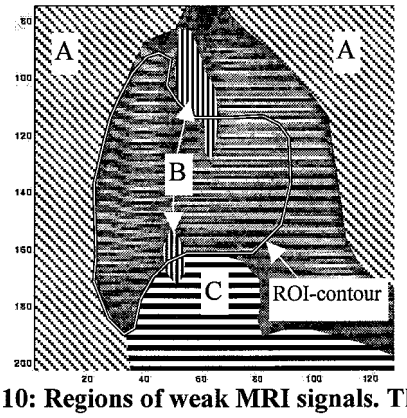

Figure 4.10: Regions of weak MRI signals. The region indicated by A) is air. The region indicated by B) is bone. It is observed that bone enters the region of interest. C) indicates the region distorted by the electrode.

The influence of the regions of weak signal outside the ROI is dual:
1) Within one image, unwrapped phase-lines lying next to each other (perpendicular to the tag lines), can show jumps of $n \cdot 2\pi$ ($n \in \mathbf{N}$).
2) Between undeformed and deformed images: the difference in position between equal phases is a measure for the deformation. However, this displacement shows a part that is related to the deformation and can show a constant part that is the same for all the points in the image, an offset phase. The consequence is that in the calculated displacements a rigid body movement is included, which does not actually exist.

The influence of weak signals inside the ROI has its consequences on the calculated displacements. This means that pixels are located at locations where they do not exist, due to their distorted phases (see the 2 displacement vectors around (50,160) in figure 3.5). The effect of these distortions on the strain calculations is the occurrence of large strains.

Case 1) was resolved by unwrapping along one line perpendicular to the first unwrapped phase-lines. Case 2) can be resolved by subtracting the phase difference from one of the images, if the phase in a point (in the deformed and undeformed state) is known (e.g. where u=0). When calculating strains, this so-called rigid body movement is of no importance.

The occurrence of weak signals inside the ROI has to be prevented, by selecting a slice with no bone in it or by selecting a ROI, which contains no weak signals. The latter explains the "hat"-shaped ROI in our experiments.

Displacement perpendicular to the slice of observation
The muscle did not only deform within the 2d slice that was selected, but also perpendicular to the selected slice of observation.
The slice of observation was a slice that was selected from the anatomical coordinate system, but was fixed in the magnet coordinate system. As a result, the slice did not follow the material points in the displacing tissue. This means that in the deformed state other tissue was scanned, when the tissue moved perpendicular to the slice of observation. This perpendicular motion along the intersection of the slice of observation and the xy-plane is depicted in figure 4.11. It is observed that the perpendicular displacement $u_\perp$ was at maximum value ($u_\perp$=0.8 mm) at the skin-side of the m. tibialis anterior and decreased further into the leg. Recall that the slice thickness was 1 mm, so right below the skin surface, 80% new tissue entered the slice. The displacement field in figure 3.6 shows all displacement vectors in the xy-plane.

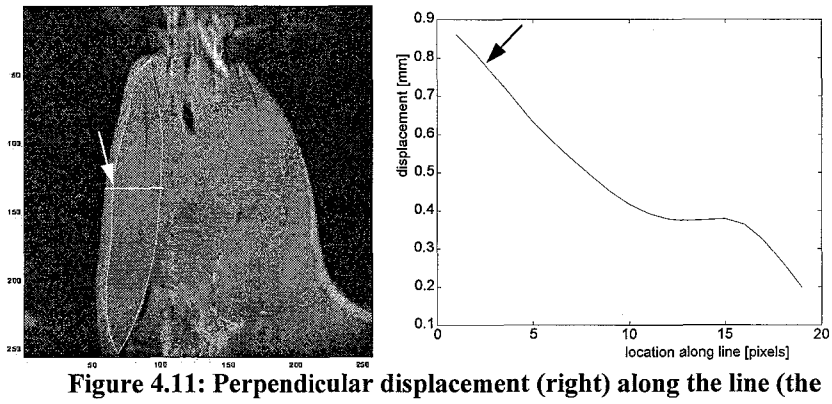

Figure 4.11: Perpendicular displacement (right) along the line (the intersection of the xy-plane and the depicted slice of observation) in the left-hand image. The arrows mark the skin-muscle transition.

The 2d-displacement fields in slices parallel to the selected slice of observation were approximately the same. This means that the displacements perpendicular to the slice of observation could have a negligible effect on the 2d strain estimation.
A muscle is a 3 dimensional structure and therefore it is important to calculate 3d displacement fields instead of 2d displacements within a slice.

4.3.3 Data analysis

In tables 3.1 through 3.4 it is observed that the extreme strains imposed by eq.(2.40) and eq.(2.41) are exceeded. The minimum and maximum strains in tables 3.1 through 3.4 are caused by bone and/or edge disturbances. They can be avoided by selecting a ROI without bones.
Another cause of the exceeding of the maximum strain is the shape of the hanning window. It is square, so when lengthening occurs along a line at an angle of ±45° and no strain or shortening perpendicular to this line, a stretch ratio can be detected that is a factor $\sqrt{2}$ larger than the imposed maximum stretch ratio by equation 2.39. As a result a larger strain is detected.

4.3.4 Error analysis

4.3.4.1 Strain field between 2 undeformed muscles

There were some regions with large strains in the ROI of figure 3.10 and 3.11:
1. a horizontal band at 155<y<161;
2. at some edges of the ROI (e.g. around (25,150));
3. around (50,158);

These 3 cases have different causes:
Case 1 was the result of 2 horizontal tag lines sticking together in one undeformed muscle, whereas this did not occur in the other undeformed muscle. This case can be avoided by applying tag lines with a larger peak to peak distance. But here it is a coincidental artifact, because it occurs local and not for all tag lines.
Case 2 was a combination of weaker signals emanating at the edges of the ROI and the filter procedure. This will be explained in §4.3.4.2. It can be avoided by selecting a ROI not to close to regions with weak MR signals.
Case 3 occurred at the region where the tibia tended to enter and disturb the tag lines. This can also be avoided by selecting a slice of observation and ROI without any bones.

Tables 3.5 through 3.7 are presented with median values instead of mean values to prevent the influence of the exceptional large strains.

4.3.4.2 Artificial muscle

Large strains were observed at x=63.5 in figures 3.13 and 3.14, as well as large shear in figure 3.15. Considering the whole region of interest as a continuum is the cause of the large strains that appear along the transition. "In reality" - also in the in vivo experiments - the m. tibialis anterior slides along the adjoining other muscles without undergoing any shear. This phenomenon can be used for detecting tissue transitions, as it is sometimes difficult to differentiate transitions between different muscles from MR images.

Identical to the in vivo experiments, errors are seen at the edges. This is partly a result of the filtering procedure (another reason is the strain estimation procedure: especially the 1st order estimation causes errors at edges).
An abrupt transition – transitions consisting of large strain gradients, but also transitions between regions of strong MR signals and weak MR signals – has to be described by limited frequencies (defined by the bandwidth). Theoretically, perpendicular to the line x=63.5, a sudden transition in strain from ε_{11}=0.3613 to 0 should be observed (an example of a large strain gradient). This can be resolved partially by applying a larger bandwidth to frequency ratio (BFR=1 or BFR=1.2 doesn't make much difference, as can be seen in figure 4.12). However, if the bandwidth is chosen wider, more high frequency noise enters the filtering procedure. Lowering the frequency restricts also the bandwidth, because overlap with the negative frequencies has to be avoided (BFR<2).
Edge errors at signal-no signal transitions can be avoided mostly by selecting a ROI not to close to regions with weak MR signals.

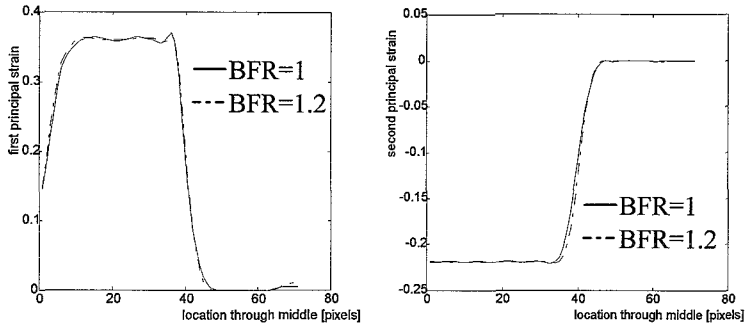

Figure 4.12: a) 1st principal strain, horizontally along the middle of the numerical hind-leg. b) 2nd principal strain along the same line

4.3.5 Strain field review

It was seen in the xy-plane that the tibia wasn't fixed completely and moved approx. 0.1 mm when the m. tibialis anterior was stimulated. The fixations are situated at the foot and the femur, enabling small motions at the knee. As a result, the tibia can deform nearby soft tissue and subsequently non-zero strains are observed in figure 3.7 and 3.8 (1st and 2nd principal strains of the deforming muscle) at the right-hand side of x=55. Other causes of these non-zero strains are:

- The m. tibialis anterior deforms neighbouring tissue in a direct way by pushing or pulling it. This can be clearly seen in figure 3.6 (the displacement field of the xy-plane). The skin is pulled at the top side of the leg. This effect does not need to be prevented.
- Another (possible) explanation could be leaking of signal of the stimulation electrode to nearby nerves, such that other muscles undergo a deformation by stimulation. However, it is not clear if this is the case.

To prevent tibia motion, the tibia should be fixed instead of the femur.

The large strains and shear along x=50 are caused by the transition of the m. tibialis anterior and the m. soleus. Here, the tibialis slides along undeformed tissue. The large strains around (55,160) are caused by another reason: the tibia enters the image slightly, disturbing the tag lines and as a consequence the phases. At the left-hand tibialis contour also large strains and shear exist, due to sliding of the muscle along the skin.

It can be expected that the direction of the 2nd principal strain aligns with the muscle fibers, showing contraction. The 1st principal strain is accordingly perpendicular to the fibers. Obviously, looking at figure 3.7 and 3.8, this is the case. However, recall that if shear is present, the directions of the principal strains rotate.
The m. tibialis anterior contains distally a tendon sheet. If we have a look at the region around (40,120), one sees that the 2nd principal strain is oriented perpendicular to the main muscle axis. At the high-resolution MR images, it is seen that the tendon sheet is situated from (40,120) to the upper side of the muscle. However, there is almost no shear around (40,120).

The tissue around (43,106) is stretched in all the in-plane directions ($\varepsilon_{11}>0.12$, $\varepsilon_{22}>0.4$). This implies that perpendicular to the slice, the tissue is strongly compressed ("ε_{33}"=-0.27, assuming incompressibility). Because this region is located near the distal end of the muscle, it is likely that the muscle fibers are oriented at an angle "out of the figure".

The overall magnitude of lengthening perpendicular to the main muscle's axis (presented by the median value of $\varepsilon_{11}=0.15$) is larger than the shortening of the muscle (presented by the median value of $\varepsilon_{22}=-0.07$). A possible explanation is that the selected slice of observation is not situated completely parallel with the muscle fiber direction. The larger the angle between the slice and the fiber direction, the larger (more positive) the second principal strain becomes. The influence of the 3d motion (the motion of tissue perpendicular to the slice) is also indistinct.

5. Conclusions

It is possible to define an anatomical coordinate system. The system is based on:
1. The tibia-fibula fusion
2. Gradient in the proximal tibia cross-section area
3. Positions of fibula and tibia in a cross-section between the fusion and the gradient

It is possible to define a longitudinal slice of observation, partly based on the anatomical coordinate system and partly on the m. tibialis anterior.

It is possible to perform a phase analysis of MR tag lines in the frequency domain and as a result to determine a displacement field. Vertical and horizontal displacements were determined separately. The phase analysis enables to determine displacements per pixel. The size of a pixel was 0.23×0.23 mm. The region of interest contained over 3000 pixels.
The choice of bandwidth frequency ratio in the phase analysis depends on the strains that can be expected and on the magnitude of noise. For the m. tibialis anterior, BFR = 1 is sufficient in the used slice of observation.

Displacements were used to estimate Green Lagrange strains per pixel in a straingroup of 8 pixels. Differences between 1st and 2nd order strain estimation are small. The absence of large gradients in the tissue (with exception of tissue-transitions) and the large concentration of markers (the pixels) enable a 1st order estimation of strains under the circumstances (for a supramaximal, isometrical, tetanical stimulation). However, a more complex deformation field implies that a new trade-off has to be made concerning 1st or 2nd order strain estimation. Also, when larger strains exist in a deformation field, a wider bandwidth is needed. Bone in the ROI has to be avoided, because bone distorts tag lines.
Uncertainties in the estimated strains lie in the order of 0.01 on a median value of 0.09 for the first principal strain and –0.04 for the second principal strain.

Transitions between deforming and non-deforming tissue are detected by large strains and shear. The 2nd principal strain shows a tendency to align with the main axis of the muscle and such with the muscle fibers, but this is not the case at all locations within the muscle. The muscle fiber direction however, has to be determined in another diffusion weighted MRI experiment to make a comparison.

6. Recommendations

- Reproducibility of the anatomical coordinate system needs to be quantified.
- It is difficult to locate the m. tibialis muscle contour visually at muscle-muscle transitions in the implementation of the anatomical coordinate system. Therefore, optimal echo time TE and repetition time TR have to be found in creating images with maximal contrast between muscle and connective tissue. Also, a higher image resolution is needed. A resolution somewhere between 128 and 256 pixels for 30 mm must be possible and is yet to be determined/calculated for the read-out direction.
- Because of the tibia's motion, the tibia should be fixed in stead of the femur.
- The electrode should be hitched further away from the region of interest. In this manner, a phased image can be acquired in which the negative magnetization appears with a 180° phase. Such an image prevents sticking of tag lines. Another advantage is the absence of a 2^{nd} harmonic in the frequency domain, so overlap between the 1^{st} and 2^{nd} harmonic is not possible anymore when large strains exist.
- Weak MR signals disturb the calculated displacements of the complex phase analysis. These disturbances happen at edges of soft tissue and air and at soft tissue-bone transitions. To avoid these areas being taken inside the region of interest, the signal intensity could be thresholded at amplitude magnitude. In this manner, pixels with low intensity are removed. This threshold procedure should be performed in both the images containing the undeformed and deformed muscle. However, it is better to prevent the occurrence of weak MR signals in the region of interest.
- The strains are estimated by using a strain group definition. However, strains can also be calculated by differentiating the displacements with respect to their positions by multiplying the frequency spectrum with $i\omega$ and transforming the result back to the spatial domain. This is possible, because displacements are calculated per pixel in stead of using tags. In this way, resolution is preserved.
- To calculate strains in the direction of the fibers, a diffusion weighted MR image should be made of the slice of observation. Another way to yield the fiber direction is to dissect the hind-leg, right through the slice of observation and perform a histological examination.
- More experiments are needed to acquire more certainty related to the anatomical coordinate system and the strain computations.
- 3d deformations have to be measured.

Bibliography

Axel L, Dougherty L. *MR imaging of motion with spatial modulation of magnetization.* Radiology 171: 841-845, 1989

Bogaerds, A.C.B. *Parametrizering van geometrie en vezelveld van skeletspier uit MRI-meting.* WFW-report 97.025, Eindhoven University of Technology, 1997.

Drost, M. *Rat's m. tibialis anterior anatomy is equivalent to human anatomy.* Personal communication, 1998.

Geers, M.G.D. *Computing strain fields from discrete displacements in 2d solids.* Int. J. Solids Structures. Vol. 33, nr. 29: 4293-4307, 1996

Gielen, A.W.J. *A continuum approach to the mechanics of contracting skeletal muscle.* In press, 1998.

De Graaf, R.A. *In vivo nmr spectroscopy. Principles and techniques.* John Wiley and Sons. In press, 1998.

Hendrich, K. et al *Surface coil cardiac tagging and ^{31}P spectroscopic localization with B_1-sensitive Adiabatic pulses.* Magnetic Resonance in Medicine 31: 541-545, 1994

Kretzers, L.J.G. *Bepaling van de spiervezel richting met behulp van Diffusie Gewogen Magnetic Resonance Imaging.* WFW-report 96.074, Master's thesis. Eindhoven University of Technology, 1996.

Ossevoort, L. *Measuring deformation in skeletal muscle using NMR imaging techniques.* WFW-Report 97.034, Master's thesis. Eindhoven University of Technology, 1997.

Popesco P. et al. *A colour atlas of Anatomy of small laboratory animals, volume II: rat, mouse, hamster.* Wolfe Publishing Ltd. London, 1992

Peters, G.W.M *Tools for the measurement of stress and strain fields in soft tissue: application to the elbow joint.* Rijksuniversiteit Limburg. Maastricht . Ph.D. thesis, 1987

Philips *Basic principles of MR imaging.* Second edition.

Williams, P.L. *Gray's anatomy,* 38th edition. London: Churchill Livingstone, 1995

Appendix A: Image formation in MRI

In order to reconstruct an image, it is necessary to spatially encode the echoes emanating from the resonating nuclei in the tissue. For the more basic principles of magnetic resonance, one is referred to the literature (Philips).

A.1 Slice selection

It is possible to superimpose a weak linearly increasing magnetic field on the static field B_0 in all possible directions. As a result, the nuclei precess along the imposed magnetic gradient with different frequencies, depending on their spatial location.
Now, if a narrow bandwidth radio frequency pulse (RF) is exposed to the tissue, only those nuclei where the Larmor frequency matches the frequencies in the RF pulse, will absorb the energy. Such, a slice of excited nuclei is selected. The position of a slice can be changed by off-centering the gradient

The slice thickness is determined by the magnitude of the magnetic gradient and the bandwidth (see figure A.1).

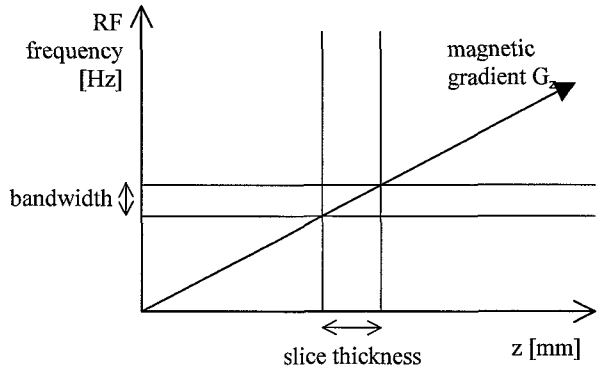

Figure A.1: Slice selective excitation. Combination of a bandwidth RF pulse and a magnetic gradient G_z, selects a slice of a certain thickness.

However, because of the Larmor relationship $\omega=\gamma(B+zG_z)$, spins within the slice precess with slightly different frequencies. As a result, the spins will dephase. The spins are brought back in phase by applying a rephasing gradient. This rephasing gradient has opposite polarity in relation to the first applied slice selection gradient. Thus, maximal signal intensity is achieved from the slice.

A.2 Spatial encoding

After slice selection, the spins within the slice have to be spatially encoded in order to reconstruct an image. The spatial encoding is done by frequency and phase encoding.

A.2.1 Frequency encoding using a read-out gradient

If a second magnetic gradient G_x is applied orthogonally to the slice selection gradient G_z while receiving the signal, the frequency of the emitted signal can be related to its position along the G_x gradient axis. The

amplitude of each frequency component after a Fourier transformation is proportional to the summed signal in the y-direction for the x-position, thus a 1d image. To acquire a 2d image from the selected slice, we need a third gradient.

A.2.2 Frequency and phase encoding

The phase-encoding gradient G_y is applied orthogonally to both the slice selection gradient G_z and the frequency encoding gradient G_x. By combining all 3 gradients and applying a 2d Fourier transformation, an image is obtained.

When along the y-direction the phase-encoding gradient G_y is turned on, the spins will have different frequencies related their position - alike the frequency encoding gradient G_x. However, when the phase-encoding gradient is turned off, spins will precess at their original frequency. But now, their phases have been changed, according to their position along the y-direction. Next, the frequency encoding gradient is turned on while receiving the signal. The signal component at a particular frequency along the x-axis is the sum of all the vector contributions from a row of spins in the y-direction. The signal generated represents a composite of all frequency components along the x-axis. During the read-out, the signal is sampled, acquiring N_x data points. Repeating the measurements N_y times for different values of the phase encoding gradient, yields a matrix of $N_y \times N_x$ points, the k-space. The k-space is actually a collection of echoes put parallel next to each other (e.g. the profile at $k_y=0$ is the echo measured after an applied zero phase encoding gradient).

If we 2d Fourier transform this k-space, we produce a 2 dimensional spectrum of $N_y \times N_x$ pixels whose intensity is representative for the signal distribution in the selected slice. The MR image is a gray-scale representation of the spectrum.

A.3 MR imaging sequences

A.3.1 Spin echo imaging

Figure A.2 shows a standard spin echo sequence. The combination of a 90° RF pulse and the selection of the

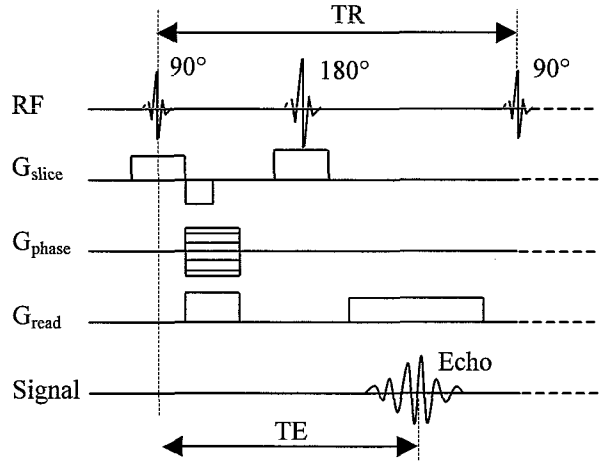

Figure A.2: Standard spin echo sequence. The combination of a 90° RF pulse and a magnetic gradient G_{slice} selects a slice. Next, the spins are phase-encoded within the slice by a magnetic gradient G_{phase}. At the same time a negative G_{slice} and a G_{read} do a refocusing of spins. A slice selective 180° RF pulse rephases the dephased spins, causing an echo. This echo is scanned while being frequency encoded by a G_{read}. The procedure is repeated N_y times with different phase encoding gradients G_{phase}.

slice selection gradient define the image slice. The 90° RF pulse flips the magnetization to the horizontal plane. The 180° RF pulse at t=½TE refocuses the - due to T_2 relaxation - dephased spins. The time between the middle of the 90° RF pulse and the maximum echo signal is TE (typically 10 to 200 ms). The sequence is repeated N_y times with N_y different phase encoding gradients. The time between successive excitations is called the repetition time TR. The repetition time must be long enough in order to let the transverse magnetization return to its original orientation due to T_1 relaxation. The repetition time is typically between 200 to 2000 ms in spin echo measurements. The total scan time is $N_y \times TR$.

A variation on the spin echo sequence is the spin echo multi slice (SEMS) sequence. It operates by acquiring data from other image slices during the time between echo formation and the end of the repetition time, as shown in figure A.3. This reduces total imaging time when more slices have to be acquired. A shorter echo time TE and/or a longer repetition time TR increase the maximum number of slices which can be acquired within a TR period.

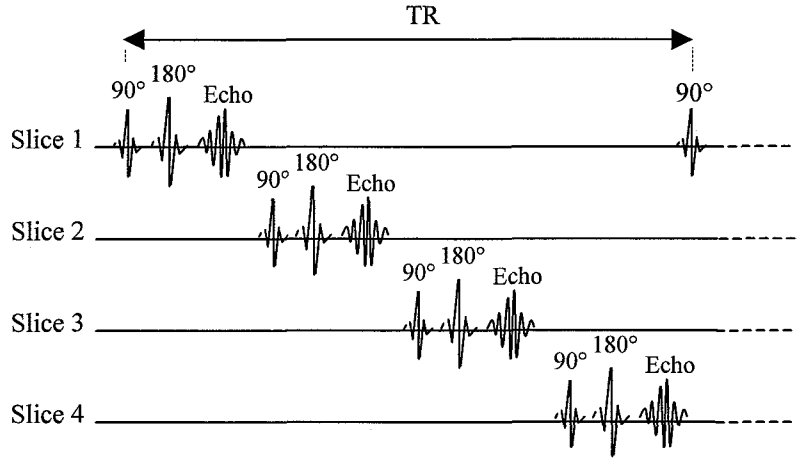

Figure A.3: Spin echo multi slice sequence. During the repetition time TR, more slices are being scanned.

A.3.2 Gradient echo imaging

Figure A.4 shows a standard gradient echo sequence. Instead of applying a 180° RF pulse to rephase the spins, they are first dephased by using a gradient in the read-out direction, following the excitation pulse. Next, the gradient is reversed. This reversal leads to a rephasing of the spins, and an echo signal. A gradient is in fact a controlled way of introducing magnetic field inhomogeneities and therefore the symbol T_2^* is also used to characterize the signal drop after switching on the gradient. This T_2^* is smaller than the "real"

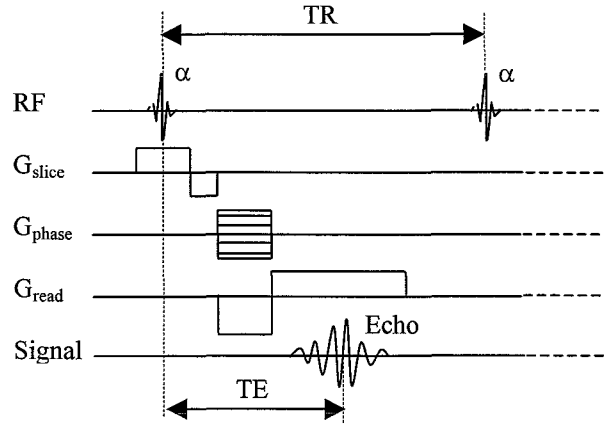

Figure A.4: Standard gradient echo sequence. A smaller flip angle α than the spin echo sequence can be used, because the rephasing is done with a bipolar magnetic gradient Gread to evoke an echo.

T_2^* due to field inhomogeneities that characterizes the signal drop of an FID without the gradient switched on.

One significant difference between gradient and spin echo formation is a sensitivity to magnetic field inhomogeneities. Unlike the spin echo sequence, gradient echo acquisition does not cancel field inhomogeneities.

The completion of an image requires repeated sampling of echoes. The repetitions take place once every repetition time. In spin echo imaging, the excitation pulse is a 90° pulse and the repetition time varies between a few hundred milliseconds and a few seconds. This long time is required to avoid saturation: Immediately following a 90° pulse, there is no effective longitudinal magnetization. Complete restoration requires a time equal to or greater than several T_1. It longitudinal relaxation is incomplete before the next excitation pulse, the effective magnetization flipped into the transverse plane is smaller.
The gradient echo sequence is compatible with the use of smaller flip angles, shorter echo times and shorter repetition times than spin echo measurements, with a resulting decrease in total imaging time. If the TR in a spin echo sequence would be reduced with a factor of 50, the total imaging time also reduces with a factor of 50. However, this would lead to strong saturation and an unacceptably low signal.

The use of shorter repetition times imply smaller flip angles. Following a limited flip angle excitation (e.g. 7°-45°), the time required to restore normal longitudinal magnetization is greatly reduced.
However, smaller flip angles are not compatible with the use of 180° pulses for generating an echo. Since a large fraction of the magnetization remains in the longitudinal plane, a 180° pulse would primarily invert longitudinal magnetization. Thus, gradient echoes are necessary instead of spin echoes. The gradient echo sequence allows image acquisition within 2 seconds.

Appendix B: Slice selection

B.1 Oblique slices

The 3 major orientations of a slice to be imaged in the magnet coordinate system are the transverse (slice plane normal to the Z-axis), coronal (Y slice plane) and sagittal (X slice plane) planes. They have readout, phase-encode and slice selection axes that are combinations of the three major X, Y and Z axes (shown in table B.1).

Orientation	*Readout*	*Phase-encode*	*Slice selection*
transverse	Y	X	Z
coronal	Z	X	Y
sagittal	Z	Y	X

Table B.1: The 3 major orientations and their encoding axes.

An oblique orientation does not correspond to one of these major planes: such a plane has to be defined using 4 parameters: the 3 euler angles θ, ψ, φ and a slice offset in cm. With these angles any arbitrary major or oblique orientation can be obtained: together with an offset any slice can be imaged. θ is the angle between the Z-axis and the normal vector of the slice to be imaged. ψ is the angle between the Y-axis and the projection of the normal vector onto the XY-plane. The third angle φ defines the rotational orientation of the slice about the normal vector: this angle can be used to switch the readout and phase-encoding axes. The major planes of course can also be described by the euler angles which is shown in table B.2.

Orientation	θ [°]	ψ [°]	φ [°]
transverse	0	0	NA
coronal	90	0	NA
sagittal	90	90	NA

Table B.2: The major orientations and their euler angles

An other way to look at the euler angles is as follows:
Define the unit vectors $\vec{e}_1$, $\vec{e}_2$ and $\vec{e}_3$ lying respectively along the X-, Y- and Z-axes. When all euler angles are 0°, the normal vector $\vec{n}$ is aligned with the Z-axis, so $\vec{n} = \vec{e}_3$. Now φ, θ and ψ define a clockwise rotation of $\vec{n}$ respectively about the Z-axis, X-axis and Z-axis again. In this way any orientation can be

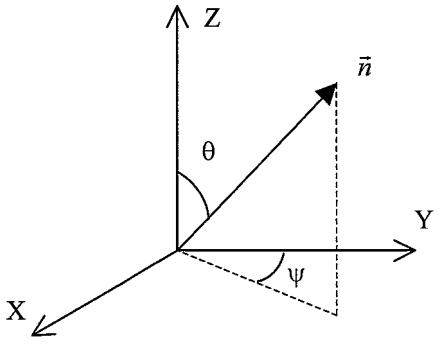

Figure B.1: Definition of the euler angles in the magnet coordinate system

accomplished. These 3 rotations can be put together in a rotation matrix $\underline{R} = \underline{R}_{\psi} \cdot \underline{R}_{\theta} \cdot \underline{R}_{\varphi}$.

B.2 Implementation of the anatomical xy-plane

The point between $\vec{p}_1$ and $\vec{p}_2$ (the center of gravity $\vec{p}_1$ of the tibia at the tibia-fibula fusion and the center of gravity $\vec{p}_2$ of the tibia in a different slice – see §2.1.4) is the anatomical origin (eq.2.1):

$$\vec{p}_0 = \tfrac{1}{2}(\vec{p}_1 + \vec{p}_2) \tag{B.1}$$

Next, the xy-plane is defined as the plane perpendicular to the vector $\vec{p}_2 - \vec{p}_1$ (defining the anatomical z-axis), through the origin $\vec{p}_0$. The normal vector $\vec{e}_z$ of the xy-plane is defined by

$$\vec{e}_z = \frac{\vec{p}_2 - \vec{p}_1}{\|\vec{p}_2 - \vec{p}_1\|} \tag{B.2}$$

The equation of this plane is

$$\vec{e}_z^{\,T} \cdot \vec{x} = d \tag{B.3}$$

In which $\vec{x}$ is a point in the plane and $d = \vec{p}_0^{\,T} \cdot \vec{e}_z$ is the slice offset (the smallest distance between plane and origin).
The euler angles θ and ψ are calculated by

$$\theta = \arccos\left(\vec{e}_z^{\,T} \cdot \vec{e}_3\right) \tag{B.4}$$

$$\psi = \arctan\left(\frac{\vec{e}_z^{\,T} \cdot \vec{e}_1}{\vec{e}_z^{\,T} \cdot \vec{e}_2}\right) \tag{B.5}$$

where $\vec{e}_1$, $\vec{e}_2$ and $\vec{e}_3$ are unit vectors defining respectively the X-, Y- and Z-axes of the magnet coordinate system.
These 3 parameters (θ , ψ and *d*) are sufficient to define a slice and can be transferred to the magnet control. If needed, the third euler angle φ can be used to change the rotational orientation of the slice in the image.

Appendix C: Strain fields

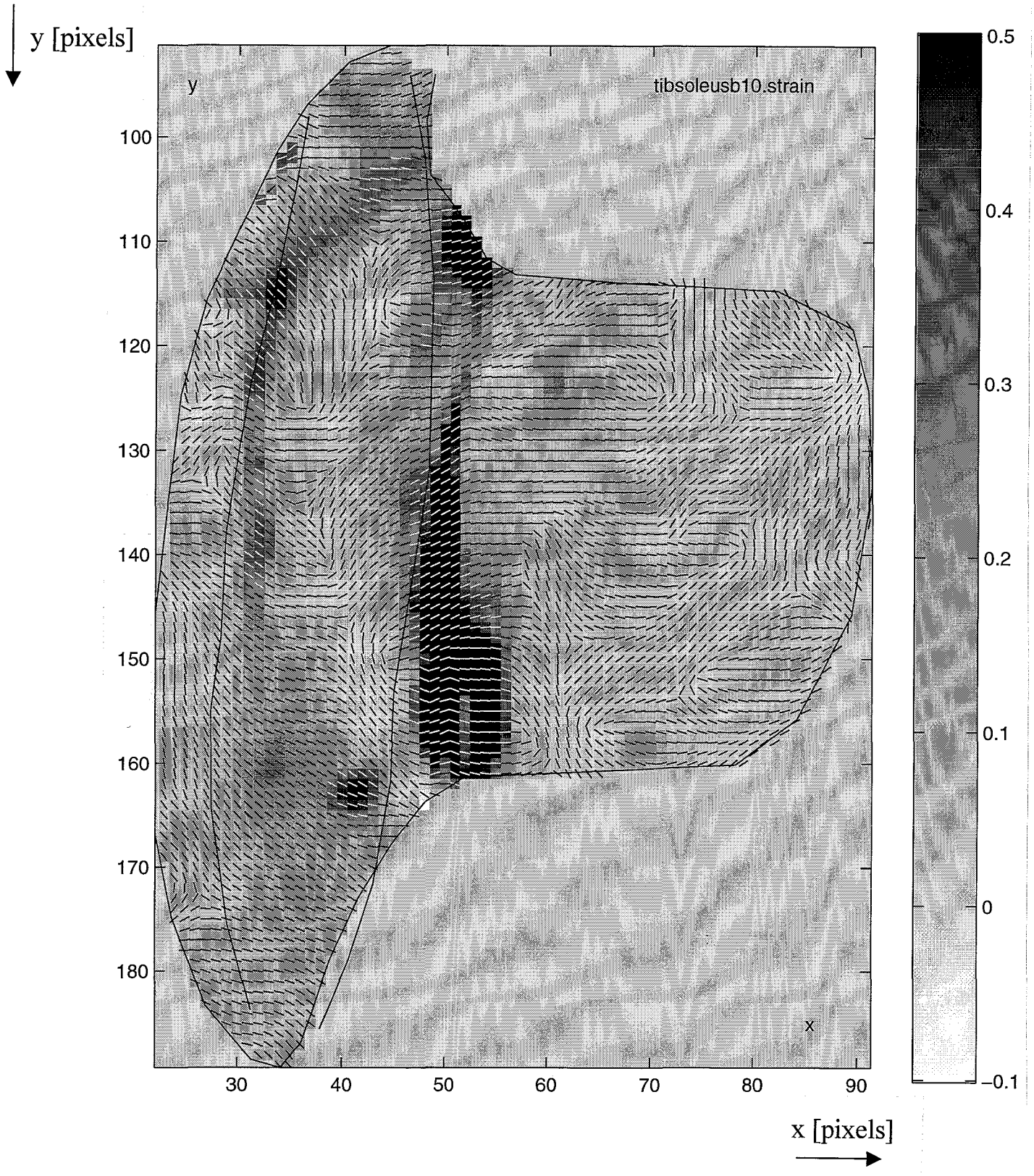

Figure C.1: 1st order estimated Green Lagrange strain field (1st principal strain ε_{11}) of the slice of observation (BFR=1). The magnitude of the strain is presented by the gray values. The direction of the strains is presented by the line pieces. The continuous line within the ROI is the deformed m. tibialis anterior contour. This strain field is also depicted in colour in figure 3.7

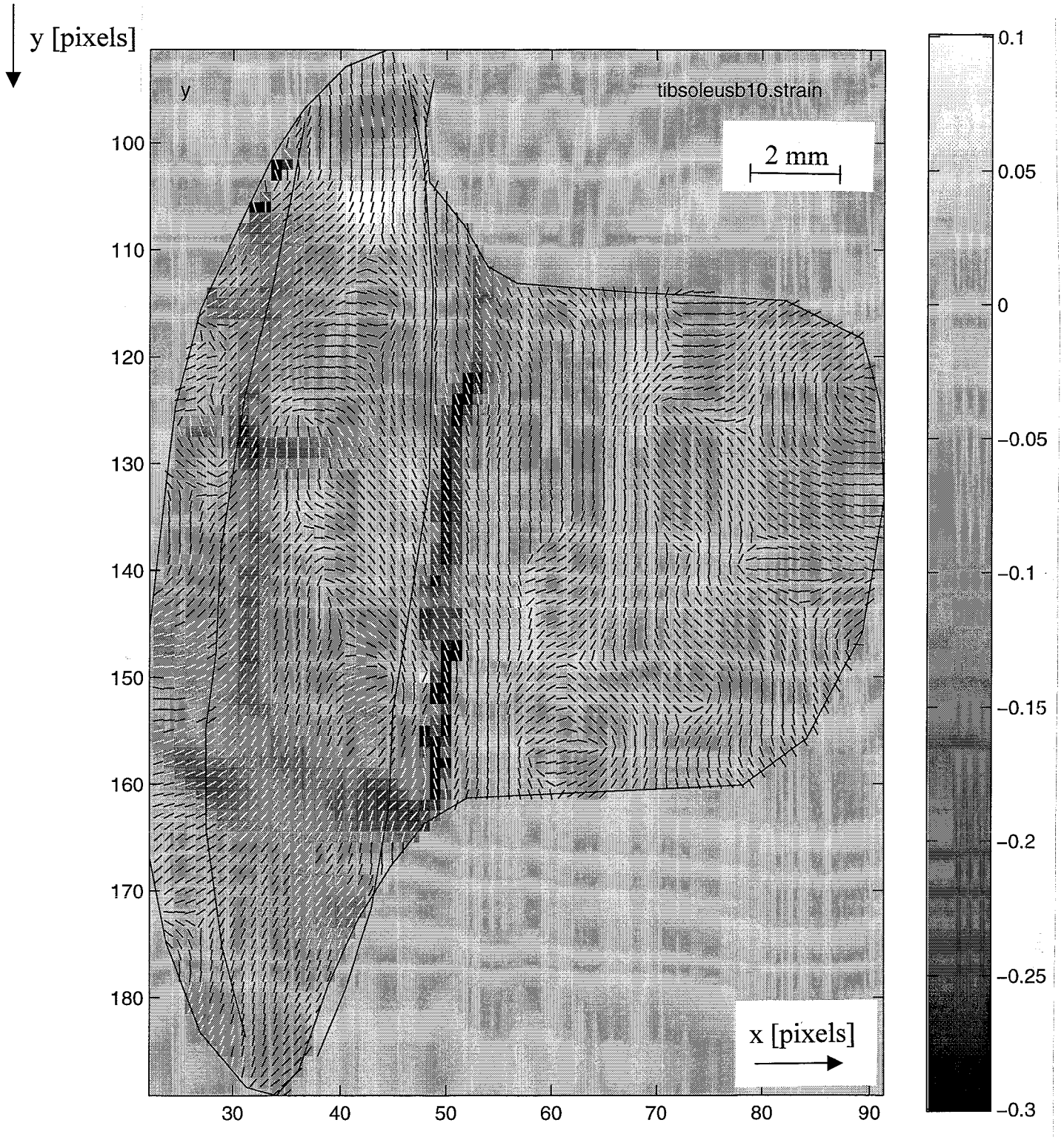

Figure C.2: 1st order estimated Green Lagrange strain field (2nd principal strain ε_{22}) of the slice of observation (BFR=1). The magnitude of the strain is presented by the gray values. The direction of the strains is presented by the line pieces. The continuous line within the ROI is the deformed m. tibialis anterior contour. This strain field is also depicted in colour in figure 3.6.

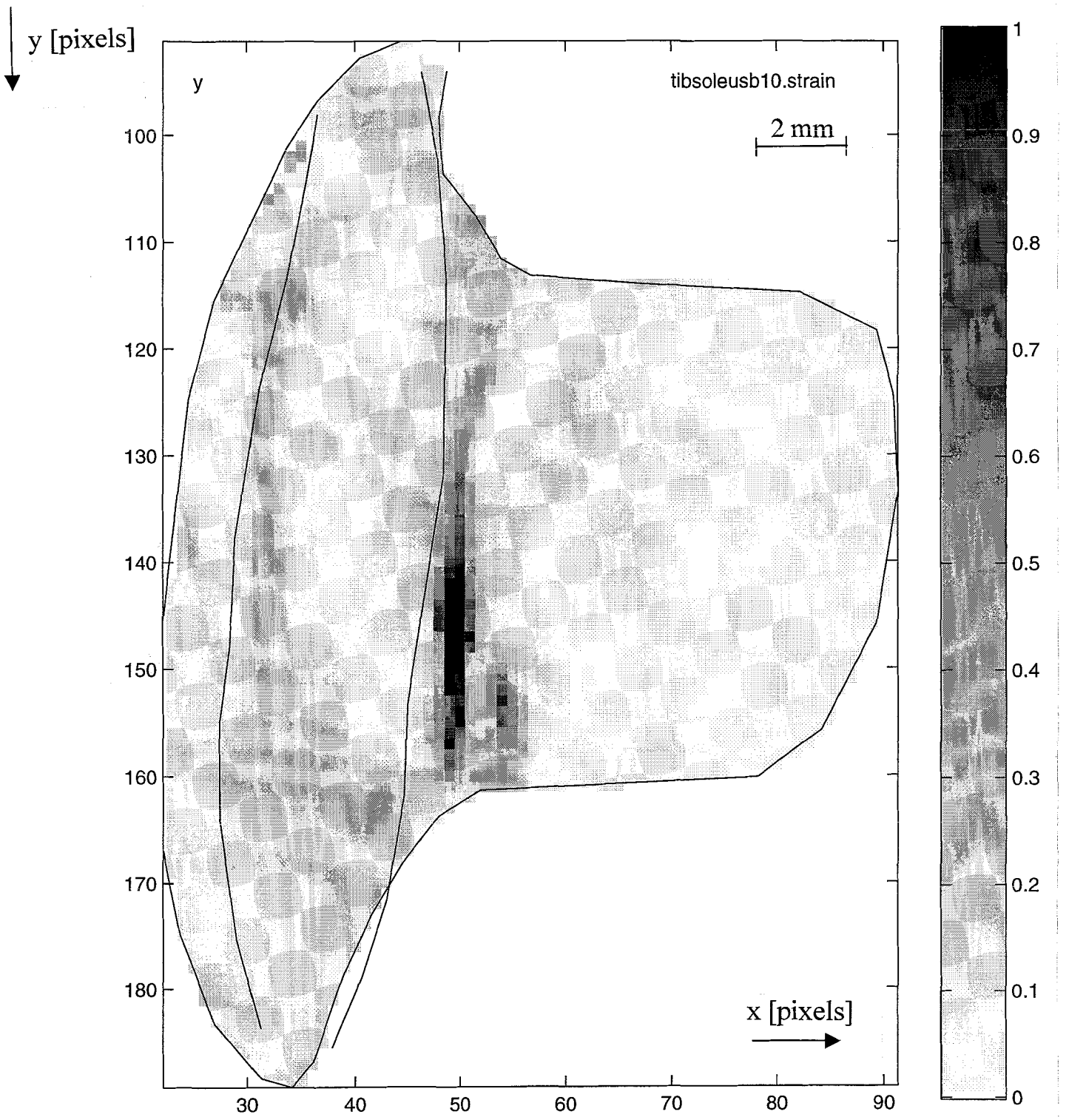

Figure C.3: 1st order estimated largest Green Lagrange shear ε_{12} of the slice of observation (BFR=1). The magnitude of the shear is presented by the gray values. The continuous line within the ROI is the deformed m. tibialis anterior contour. This strain field is also depicted in colour in figure 3.9.

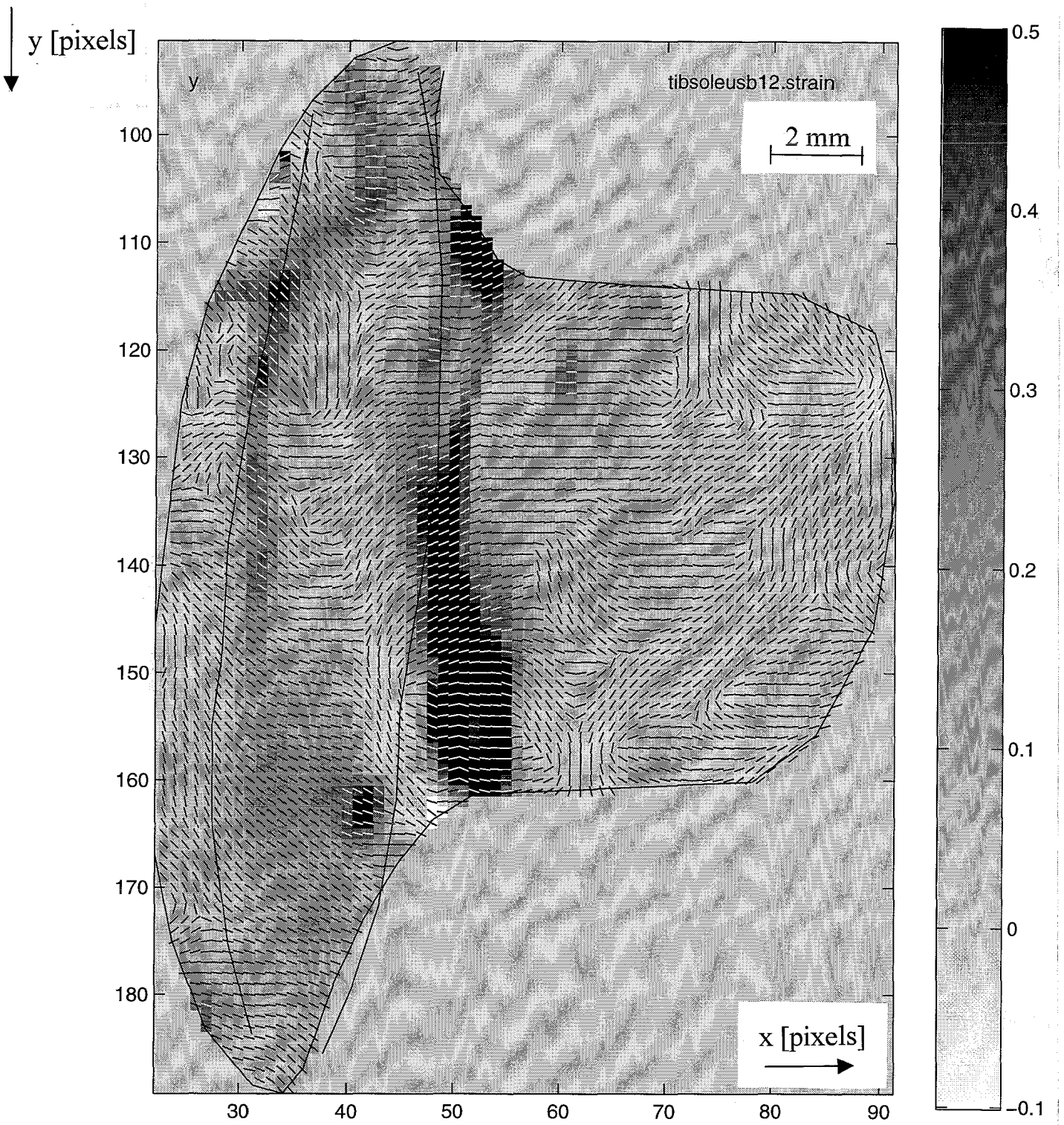

Figure C.4: 1st order estimated Green Lagrange strain field (1st principal strain ε_{11}) of the slice of observation (BFR=1.2). The magnitude of the strain is presented by the gray values. The direction of the strains is presented by the line pieces. The continuous line within the ROI is the deformed m. tibialis anterior contour.

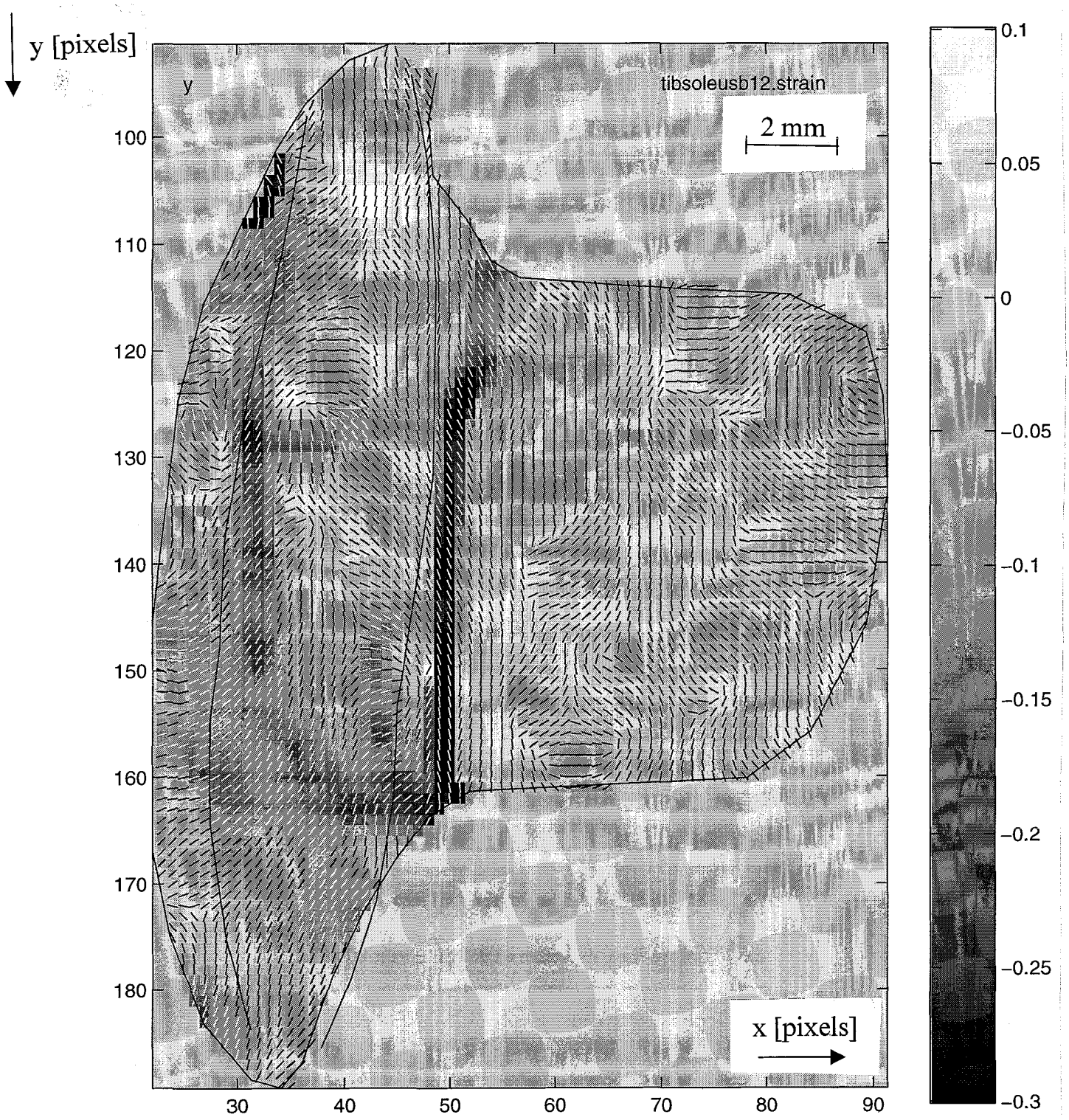

Figure C.5: 1st order estimated Green Lagrange strain field (2nd principal strain ε_{22}) of the slice of observation (BFR=1.2). The magnitude of the strain is presented by the gray values. The direction of the strains is presented by the line pieces. The continuous line within the ROI is the deformed m. tibialis anterior contour.

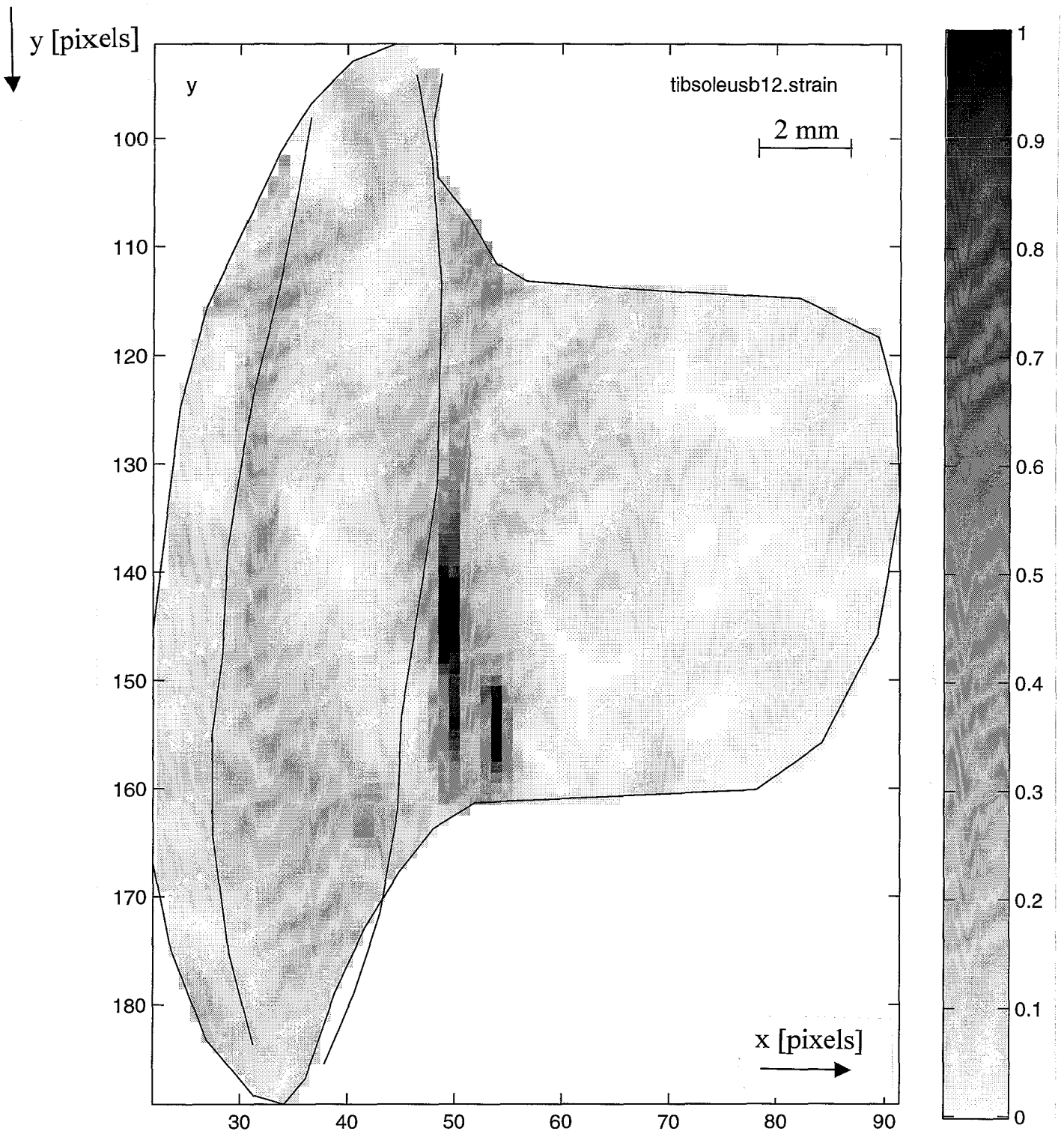

Figure C.6: 1st order estimated largest shear ε_{12} of the slice of observation (BFR=1.2). The magnitude of the shear is presented by the gray values. The continuous line within the ROI is the deformed m. tibialis anterior contour.

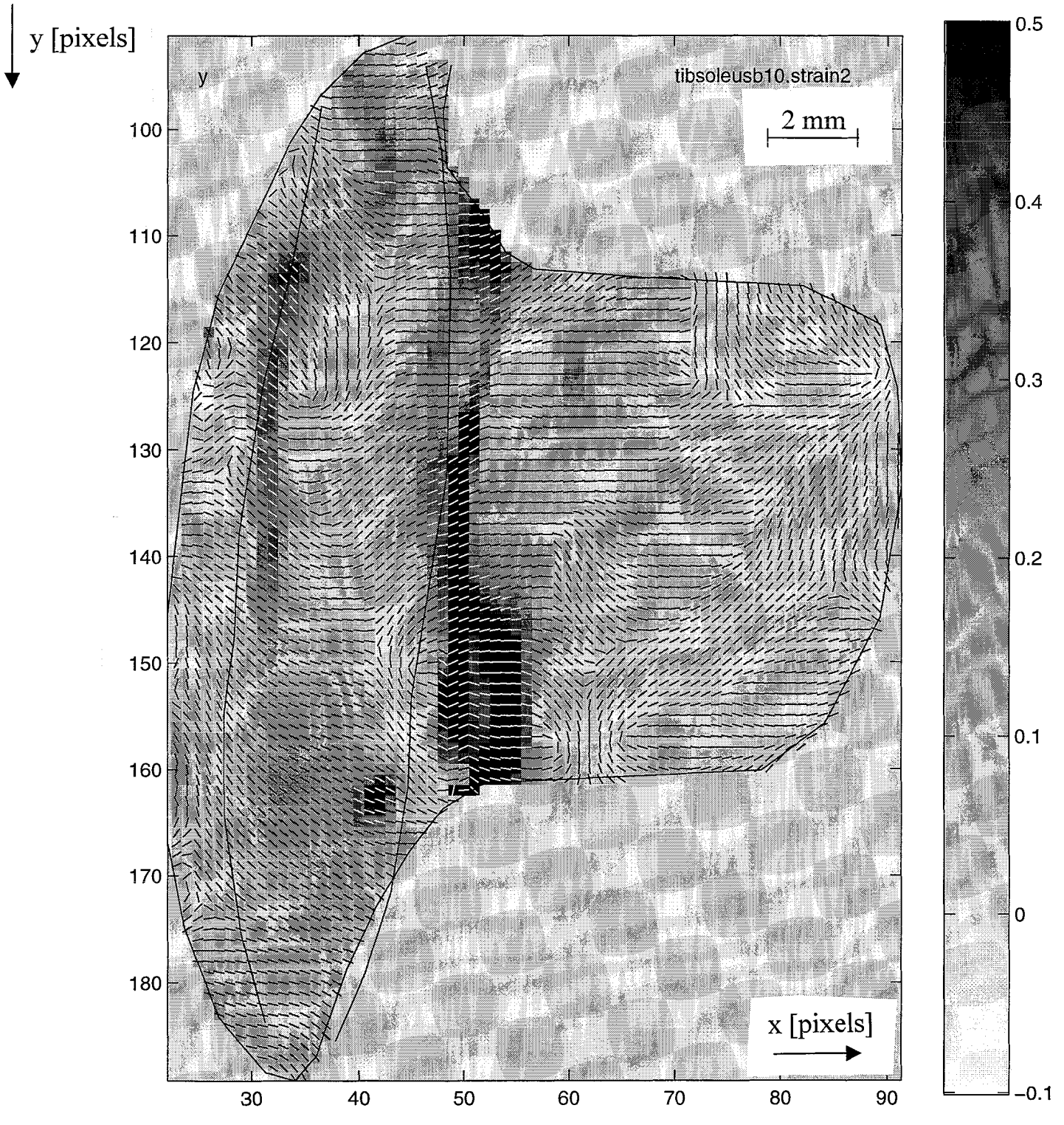

Figure C.7: 2nd order estimated Green Lagrange strain field (1st principal strain ε_{11}) of the slice of observation (BFR=1). The magnitude of the strain is presented by the gray values. The direction of the strains is presented by the line pieces. The continuous line within the ROI is the deformed m. tibialis anterior contour.

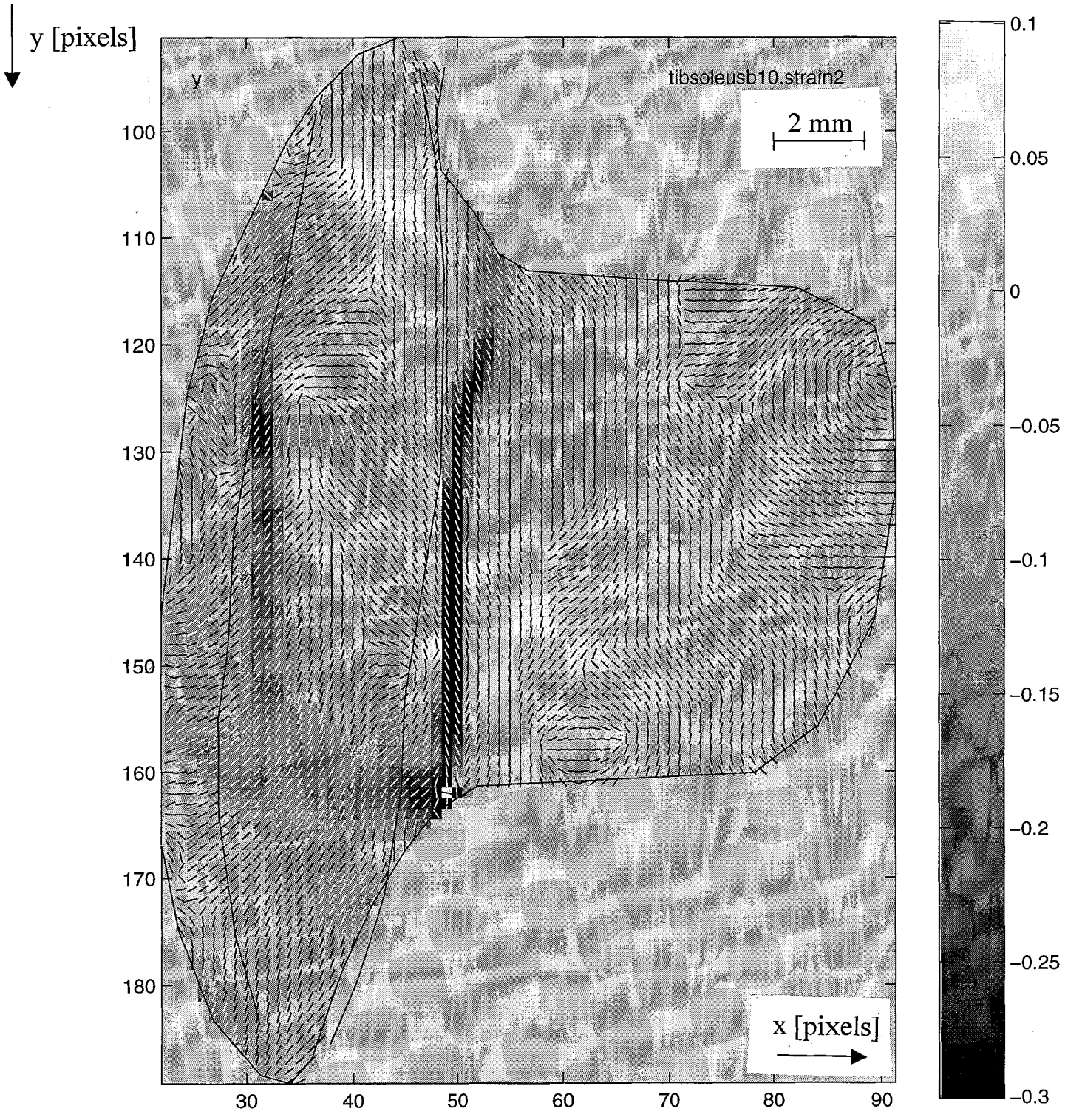

Figure C.8: 2nd order estimated Green Lagrange strain field (2nd principal strain ε_{22}) of the slice of observation (BFR=1). The magnitude of the strain is presented by the gray values. The direction of the strains is presented by the line pieces. The continuous line within the ROI is the deformed m. tibialis anterior contour.

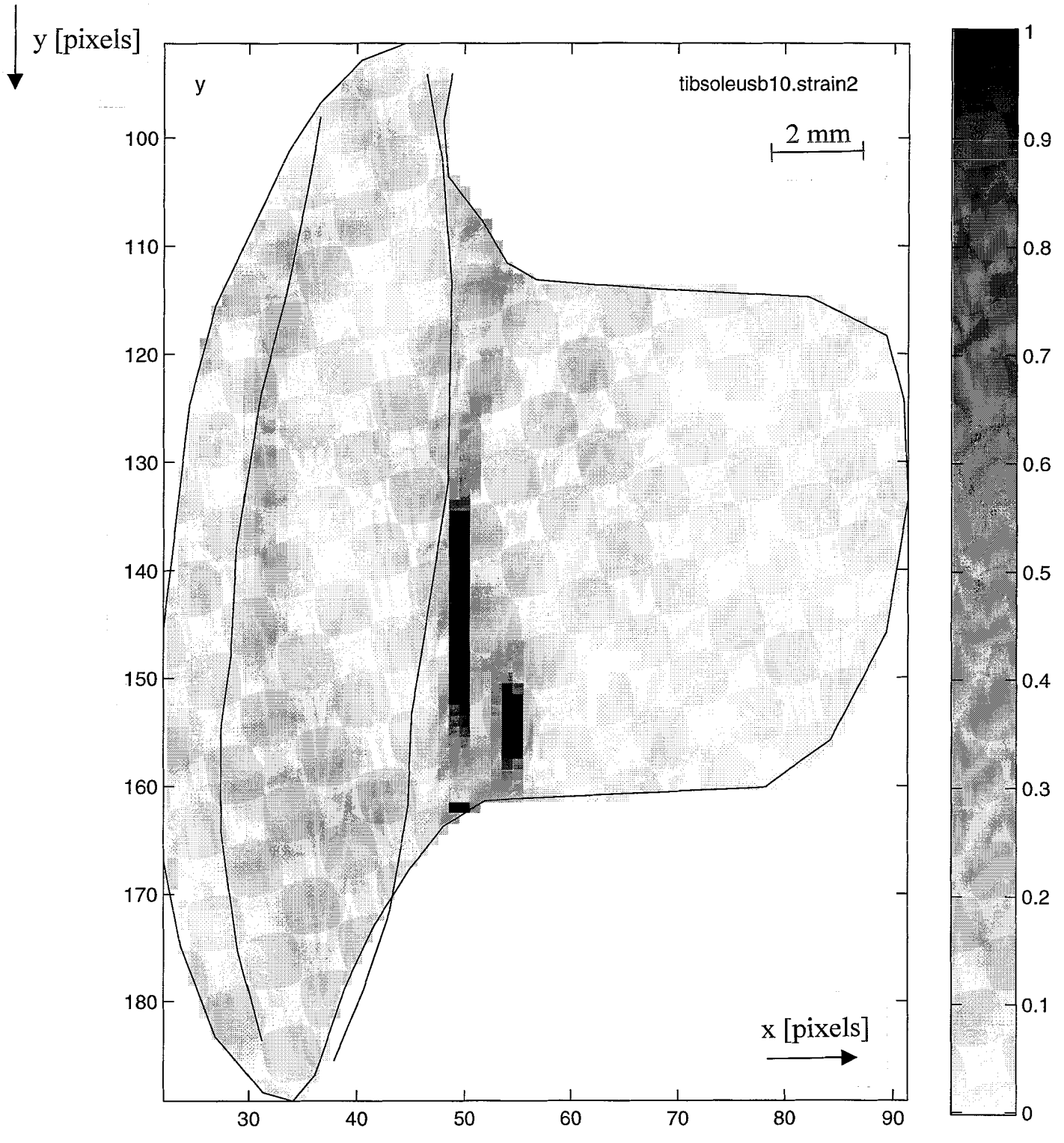

Figure C.9: 2nd order estimated largest shear ε_{12} of the slice of observation (BFR=1). The magnitude of the shear is presented by the gray values. The continuous line within the ROI is the deformed m. tibialis anterior contour.

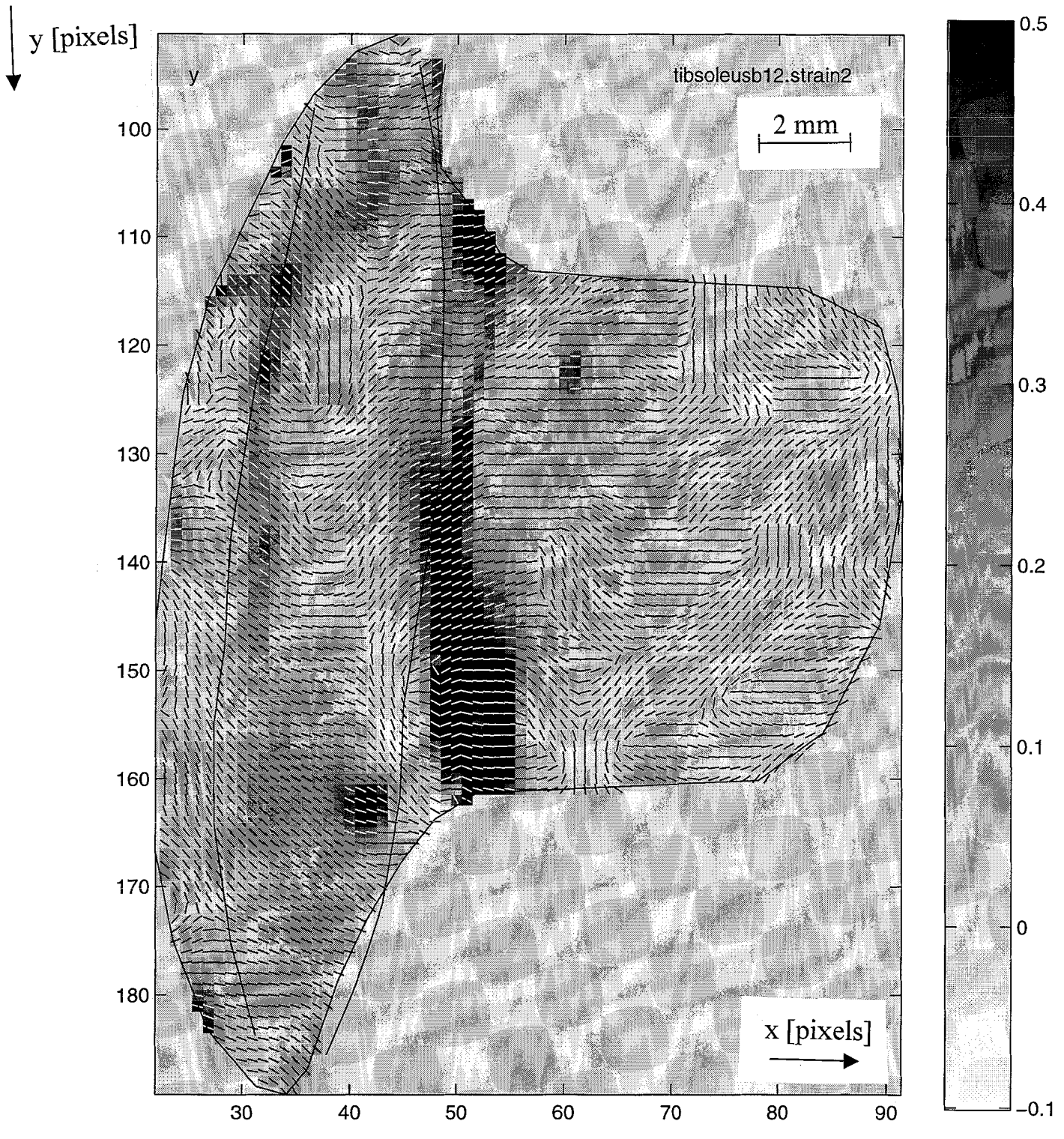

Figure C.10: 2nd order estimated Green Lagrange strain field (1st principal strain ε_{11}) of the slice of observation (BFR=1.2). The magnitude of the strain is presented by the gray values. The direction of the strains is presented by the line pieces. The continuous line within the ROI is the deformed m. tibialis anterior contour.

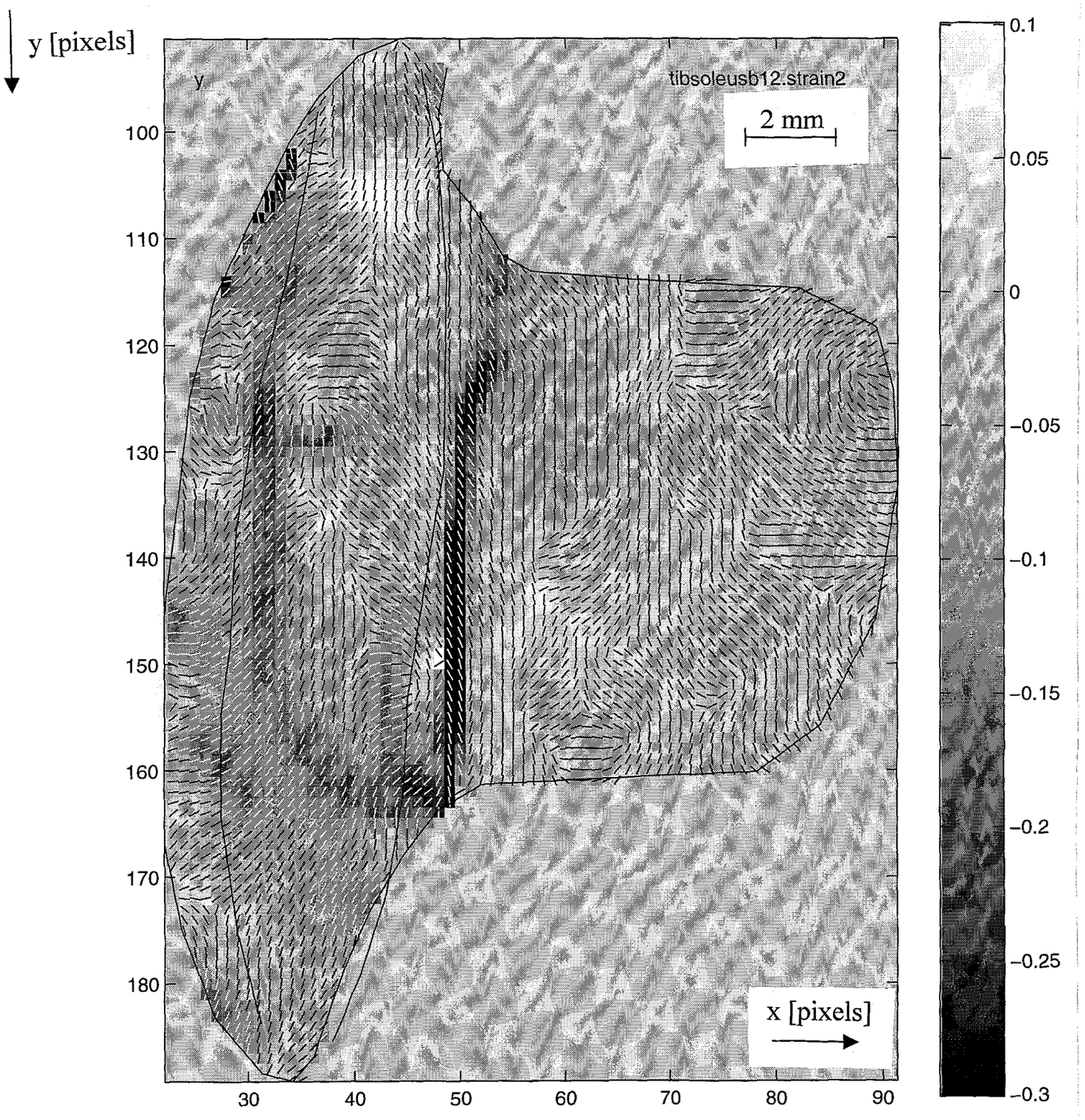

Figure C.11: 2nd order estimated Green Lagrange strain field (2nd principal strain ε_{22}) of the slice of observation (BFR=1.2). The magnitude of the strain is presented by the gray values. The direction of the strains is presented by the line pieces. The continuous line within the ROI is the deformed m. tibialis anterior contour.

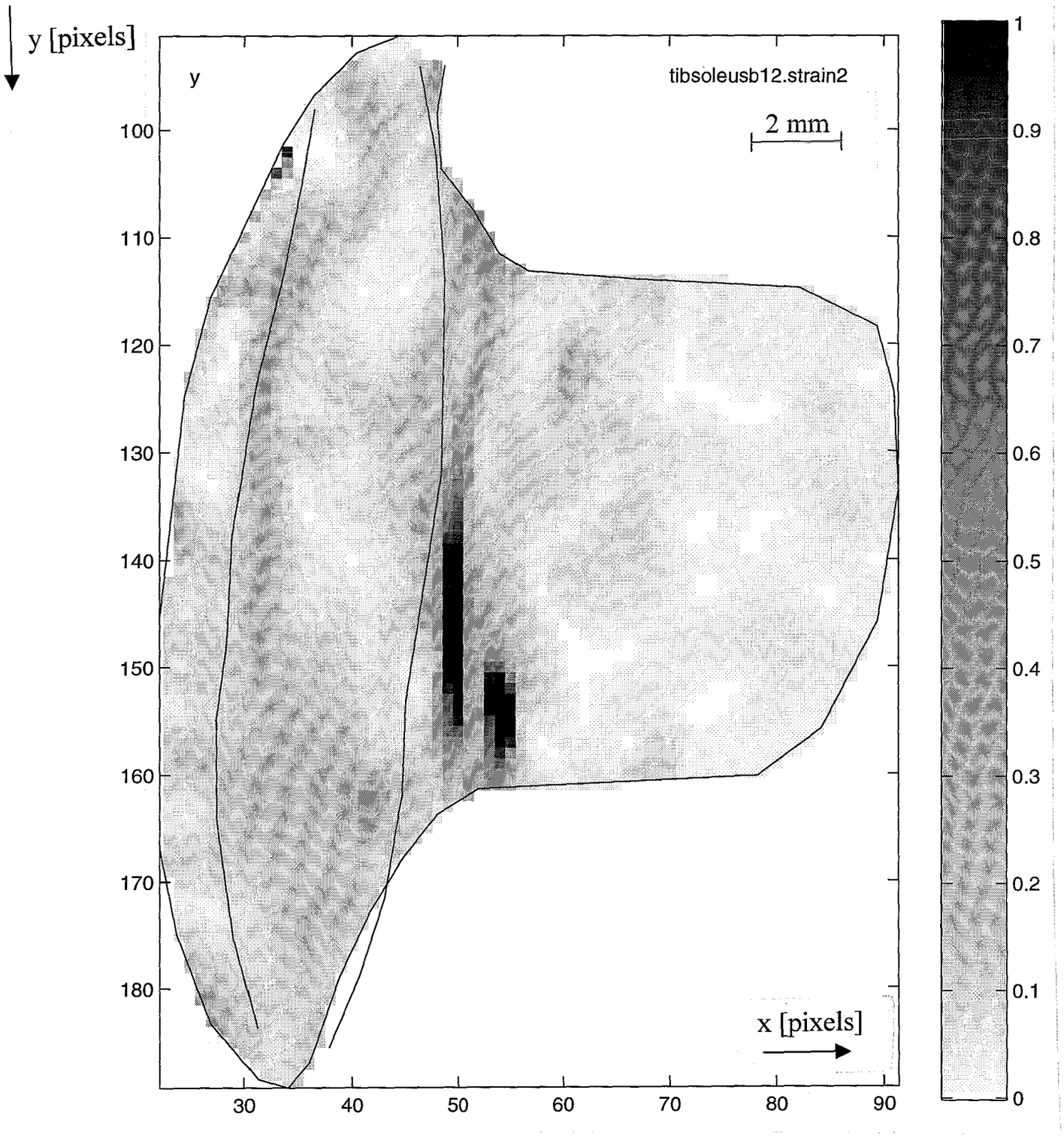

Figure C.12: 2nd order estimated largest shear ε_{12} of the slice of observation (BFR=1.2). The magnitude of the shear is presented by the gray values. The continuous line within the ROI is the deformed m. tibialis anterior contour.